DOCTORAL SCHOOL
UNIVERSITA' *MEDITERRANEA* DI REGGIO CALABRIA

DIPARTIMENTO DI INGEGNERIA DELL'INFORMAZIONE, DELLE INFRASTRUTTURE E DELL'ENERGIA SOSTENIBILE (DIIES)

PHD IN INFORMATION ENGINEERING

S.S.D. IINF-01/A XXXVII CICLO

Flexible Microdevices for Biosensing: Integrating Optics and Capillarity for Advanced Biomedical Solutions

CANDIDATE
Federica GRANATA
[redacted]

ADVISOR
Ing. Giuseppe COPPOLA
[redacted]

Prof. Ing. Francesco DELLA CORTE
[redacted]

COORDINATOR
Prof. Antonella MOLINARO

Università degli Studi *Mediterranea* di Reggio Calabria
Via dell'Università, 25 (già Salita Melissari) - Reggio Calabria

FEDERICA GRANATA

Flexible Microdevices for Biosensing: Integrating Optics and Capillarity for Advanced Biomedical Solutions

The PhD Board of the PhD course in
INFORMATION ENGINEERING
is composed of:

Antonella MOLINARO (coordinator)
Giuseppe ARANITI
Francesco Antonio BUCCAFURRI
Claudia CAMPOLO
Riccardo CAROTENUTO
Giuseppe COPPOLA
Mariantonia COTRONEI
Lorenzo CROCCO
Dominique DALLET
Claudio Roberto Maria DE CAPUA
Francesco Giuseppe DELLA CORTE
Loreto DI DONATO
Giuliana FAGGIO
Gioia FAILLA
Pasquale Giuseppe Fabio FILIANOTI
Patrizia FRONTERA
Sofia GIUFFRE'
Giorgio GRADITI
Voicu GROZA
Tommaso ISERNIA
Gianluca LAX
Aime' LAY EKUAKILLE
Gateano LICITRA
Elena Simona LOHAN
Pietro MANZONI
Giacomo Domenico Savio MESSINA
Andrea Francesco MORABITO
Rosario MORELLO
Gabriel-Miro MUNTEAN
Giuseppe MUSOLINO
Filippo Gianmaria PRATICO'
Fortunato PEZZIMENTI
Sandro RAO
Maria ROMANO
Domenico ROSACI
Giuseppe RUGGERI
Mariateresa RUSSO
Alexey VINEL
Antonino VITETTA
Maria Gabriella XIBILIA

Contents

CONTENTS **5**

LIST OF FIGURES **7**

ABSTRACT **13**

INTRODUCTION **15**

REFERENCES **24**

1. MICROFLUIDIC DEVICE FOR BIOMARKER DETECTION USING PLASMONIC SENSOR **28**

1.1 INTRODUCTION TO PLASMONIC SENSORS 29
1.2 PLASMONIC-BASED BIOSENSING 33
1.3 DESIGN 34
1.4 FABRICATION 39
1.5 DEVICE PERFORMANCE EVALUATION AS A FUNCTION OF FLOW RATE 41
1.6 FUNCTIONALIZATION 42
1.7 OPTICAL CHARACTERIZATION 44
1.8 FLUORESCENCE ANALYSIS 46
1.9 RAMAN ANALYSIS 47
1.10 CONCLUSIONS 49

REFERENCES **50**

2. FLEXIBLE PLASMONIC DEVICE FOR BIOMEDICAL APPLICATIONS **53**

2.1 SOFT MATERIAL FOR PLASMONIC BIOSENSING 53
2.1 FABRICATION 55
2.3 CHARACTERIZATION 58
2.3.1 MECHANICAL PROPERTIES OF FLEXIBLE PLASMONIC DEVICES 58
2.3.2 OPTICAL CHARACTERIZATION 59
2.4 FUNCTIONALIZATION 62
2.5 FLUORESCENCE ANALYSIS 63
2.4 COMPARATIVE EVALUATION OF FLUORESCENT SENSITIVITY ON FLEXIBLE AND RIGID SUBSTRATES 64
2.7 VERIFYING SITE-SELECTIVE AMPLIFICATION OF FLUORESCENCE SIGNAL BY GOLD NANOPARTICLES 66
2.8 VERIFYING SELECTIVITY AND SPECIFICITY OF THE SENSOR DEVICE 67
2.9 RAMAN ANALYSIS 68
2.10 CONCLUSIONS 73

REFERENCES **75**

3. WETTABILITY STUDY FOR OPTIMIZING SAMPLE SPREADING ON CRYO-EM GRIDS **78**

3.1 INTRODUCTION TO CRYO-EM 78
3.2 MATERIALS AND METHODS 81
3.2.1 CONTACT ANGLE MEASUREMENTS 81
3.2.2 FEM MODEL DESIGN 83
3.2.3 MESHING STRATEGY 84
3.3 2D NUMERICAL SIMULATIONS 86
3.4 3D NUMERICAL ANALYSIS - COMPARATIVE ANALYSIS OF THREE DESIGNS 88
3.5 CONCLUSIONS 92

REFERENCES 95

4. ANALYTICAL MODEL DEVELOPMENT FOR CAPILLARY MICROFLUDIC SYSTEM WITH EXPERIMENTAL VALIDATION 99

4.1 CAPILLARY SYSTEM (CS) 100
4.2 ANALYTICAL MODEL 102
4.3 NUMERICAL ANALYSIS MODEL VALIDATION 108
4.4 EXPERIMENTAL MODEL VALIDATION BY DEVELOPMENT OF CS 111
4.5 DEVELOPMENT AND CHARACTERIZATION OF A FLEXIBLE MICROFLUIDIC CAPILLARY SYSTEM WITH INTEGRATED PLASMONIC SENSOR 116
118
4.6 CONCLUSIONS 119

REFERENCES 120

5. CONCLUSIONS AND FUTURE PRESPECTIVE. 123

REFERENCES 132

APPENDIX A. NUMERICAL SIMULATION FOR FLUIDS DYNAMIC DESIGN OF MICROFLUIDIC DEVICES 133

A.1 INTRODUCTION TO NUMERICAL SIMULATION AND THE FINITE ELEMENT METHOD (FEM) 134
A.2 COMSOL MULTIPHYSICS 135
A.3 LAMINAR FLOW IN COMSOL MULTIPHYSICS 135
A.4 TRANSPORT OF DILUTED SPECIES IN COMSOL MULTIPHYSICS 138
A.5 LEVEL SET METHOD IN COMSOL 142
A.6 PHASE FIELD IN COMSOL MULTIPHYSICS 145

REFERENCES 147

APPENDIX B. NUMERIC LABORATORY MANUFACTORING PROCESSES 148

B.1 μ-FABRICATION 148
B.2 RAPID PROTOTYPING 150
B.3 FLEXIBLE PLASMONIC DEVICE FABRICATION PROCESS 158
B.4 OPTICAL CHARACTERIZATION 162

REFERENCES 166

APPENDIX C. HOE-BASED PDMS WAVEGUIDE FOR ADVANCED BIOSENSING 172

C.1 HOLOGRAPHIC OPTICAL ELEMENT (HOE) 169
C.2 FIRST APPLICATION 171

REFERENCES 173

ACKNOWLEDGMENTS

List of Figures

Figure 1 Sketch of the microfluidic device made of flexible material (Polydimethylsiloxane, PDMS) integrating a plasmonic sensor based on gold nanostructure clusters on a silicon substrate, along with SEM images of the optical sensor and the corresponding chemica map ... 28
Figure 1.1 a) Comparison between the filling of an ellipsoidal and a circular microfluidic chamber; b) Filling and rinsing dynamics of the system, imposing a function formed by 4 rectangular pulses; and c) Results from a concentration probe in the microfluidic chamber, showing the achievement of the desired concentration uniformity within 30 seconds from the start of flow injection and rinsing. 36
Figure 1.2. a-d) Chemical species and rinse flow within the system at the t0, t = 5 s and t = 30 s. 38
Figure 1.3. Contour lines and surface plot showing shear stress distribution within the microfluidic chamber and channel. The contour lines indicate areas of maximum shear stress, while the surface plot illustrates how stress is distributed across the channel. 40
Figure 1.4. a-b-c) Fabrication process based on soft lithography, replica molding, and sealing using RIE (Reactive Ion Etching); d) Images of the fabricated device. 42
Figure 1.5. a) External pumping system in the microfluidic device; b) Verification of uniform filling, emptying, and coverage of the plasmonic nanostructures; c) Deterioration of the gold nanoparticle substrate at a flow rate of 1 ml/min with a shear stress of 11.20 Pa. 43
Figure 1.6. Functionalization Process 45
Figure 1.7. SEM Measurement 46
Figure 1.8. AFM Measurement 47
Figure 1.9. a-b) Image of the non-functionalized sensor and fluorescence images of the functionalized sensor; c) Mean value of fluorescent intensity of folic acid captured by the sensor under different flow conditions (10 and 100 µl/min). The mean was calculated over more than 20 technical replicates, with the marker diameters in the plot proportional to the standard deviation of the measurements; d) Raman map of A-FA activity measured on the non-functionalized plasmonic substrate; e) Comparison between the average Raman spectra of A-FA measured on the functionalized and non-functionalized plasmonic substrate. 48
Figure 2. Schematic of a plasmonic sensor on flexible material integrated with microfluidics, along with fabrication images. Optical microscope images are shown to illustrate the morphology of the sensor. 54
Figure 2.1 Fabrication Process 58
Figure 2.2. Geometrical pattern by optical lithography 59

Figure 2.3. The fabricated flexible plasmonic device…… 59
Figure 2.4. a) Contact angle of a microliter drop of DI water with the PDMS plasmonic surface; b) Stress strain curve of the PDMS device…… 61
Figure 2.5. SEM images of plasmonic sensor on PDMS substrates……62
Figure 2.6. AFM image of the gold nanoparticle cluster surface (8 μm × 8 μm)……..63
Figure 2.7. AFM image of the gold nanoparticle cluster surface (6 μm × 6low μm).....64
Figure 2.8. a)Scheme of the antigen-antibody immunoassay test performed by the sensor device. b) Upon functionalization with human IgG, and exposure to anti-human IgG, the sensor device correctly captured anti-human IgG in solution, evidenced by bright green fluorescence of samples. c) Fluorescence intensity profile measured across a cluster of gold-nanoparticles after incubation with anti-human IgG ..……...…..... 66
Figure 2.9. Comparison of fluorescence intensity on PDMS and silicon substrates with varying FITC solution concentrations. Results show a similar exponential decrease in fluorescence for both materials, with PDMS demonstrating slightly higher sensitivity than expected…... 67
Figure 2.10. Comparison of fluorescence intensity between flat gold on silicon and clustered gold nanoparticles on PDMS. After exposure to FITC solution (100 μg/ml), the nano-patterned gold surface)showed approximately 3 times higher fluorescence intensity than the flat gold surface, demonstrating superior signal enhancement……69
Figure 2.11. FITC green fluorescence intensity and the mean fluorescence intensity on different substrates as a function of the ligand-receptor combination and mixture composition……70
Figure 2.12. a)Raman spectra of IL-8 molecules acquired on soft plasmonic devices for different values of concentration of the starting solution, the system is interrogated from the top (*direct*, top-down configuration); b) Raman spectra of IL-8 molecules acquired on soft plasmonic devices for different values of concentration of the starting solution, the system is interrogated from the bottom (*inverted*, bottom-up configuration); c)Mean Raman intensity of IL-8 molecules for values of concentration varying from 1 ng/ml to 100 ng/ml measured adopting a *direct* configuration and using as a refence a band centered around 1450 cm^{-1} with a bandwidth of 4 cm^{-1};d) Mean Raman intensity of IL-8 molecules for values of concentration varying from 1 ng/ml to 100 ng/ml measured adopting an *inverted* configuration and using as a refence a band centered around 1450 cm^{-1} with a bandwidth of 4 cm^{-1}; e) In some cases, Raman analysis of samples was performed on an array of points partially overlapping the cluster of nanoparticles onto which the solute was adsorbed (f) so that resulting spectra can be displayed in the form of a density plot of values – i.e. a map (g). Raman maps measured for values of concentration of IL-8 ranging in the 1 ng/ml-100 ng/ml were processed using principal components analysis (PCA); h) The diagram in reports the first (pc1) versus the second (pc2) principal component of Raman spectra in the considered range of a

concentration, measured adopting a *direct* configuration. i) The diagram in reports the first (pc1) versus the second (pc2) principal component of Raman spectra in the considered range of a concentration, measured adopting an *inverted* configuration. In both cases, points in the PCA plot are clustered according to the concentration of the originating solution ……74
Figure 3. Droplet spreading dynamics.....80
Figure 3.1 a) Sketch of the spreading process of the droplet from the microfluidic chip to the grid: a laser targets the end of a microfluidic channel, generating a microjet through optical cavitation. The droplets are propelled onto the grid and spread onto it. Tested configurations: b) simple cryo grid-cell, c) pillars cryo grid-cell, d) with channels cryo grid-cell. The numerical simulations aim to optimize the spreading of the sample droplet while keeping wettability, size, and distance from the substrate constant.....83
Figure 3.2 a) Experimental setup used for contact angle measurements on various surfaces (copper-carbon-gold); b) Graph depicting the contact angle results as a function of surface type and associated treatment…….86
Figure 3.3 a) Configuration of the 2D axisymmetric simulation in Comsol, b) Spreading behavior of the droplet on a solid substrate with a focus on the area of interest: the region covered by a water thickness ≤ 200 nm, c) Detailed 2D meshing strategy with increased elements at the phase interface, d) Comprehensive 3D structured meshing strategy……89
Figure 3.4 a-c) Radius length profile as a function of droplet height with varying contact angles (θ = 1°, 5°, 10°) for droplets fully spread on the substrate in a 2D axisymmetric simulation: a) droplet with an initial diameter of 5 μm, b) droplet with an initial diameter of 10 μm, c) droplet with an initial diameter of 20 μm. d-f) Radius length spreading factor as a function of time with varying contact angles (θ = 1°, 5°, 10°). The graph shows that droplet spreading occurs almost entirely in the initial moments after impact, followed by a much slower spreading…… 91
Figure 3.5 Distribution of water after a droplet has fallen into the cryo-grid cell and evaluation of the area with a water thickness ≤ 200 nm, which is useful for cryo-EM measurements: a) for a droplet at the center of the cell; b) for a droplet near the edge of the cell……...92
Figure 3.6 Cuts of the yz planes at three different positions: a-b)at the center, c-d) near the left boundary, e-f) and near the right boundary, for both configurations (droplet at the center (a-c-e) of the cell and droplet near the left boundary of the cell (b-d-f)). The lengths of the water with a thickness ≤ 200 nm along the defined cut planes are reported, which are consistent with the area measurements…… 93
Figure 3.7 a) Representation of individual cryo-grid cells in the three analyzed configurations: (i) simple, (ii) with pillars, and (iii) with channels; b) Representation of the total area; c) Representation of the thin area with a thickness derived from the sample drop at the center of the

model; and d) Representation of the thin area with a thickness obtained from the sample drop at the edge of the model…….....95
Figure 4. a) Sketch of the formation of the meniscus in a fluid within a rectangular microfluidic channel. b) Formation of a concave and convex meniscus depending on the contact angle.....102
Figure 4.1. a) Initial domains of water and air before the simulation starts; b) Meniscus formation, influenced by the surface properties of the channel.....112
Figure 4.2 Comparison between the analytical model and numerical simulation data. 113
Figure 4.3. Velocity profile of the fluid flow over time. The initial peak represents the acceleration of the fluid as it rapidly adheres to the channel walls, defined by the contact angle. Following this, the velocity stabilizes at a terminal value, indicating the formation of a fully developed and stable meniscus. 114
Figure 4.4. Two fabrication methods for CS were used: soft lithography: the classic method for creating precise microstructures in PDMS; xurography: fabrication using a cutting plotter, a fast and low-cost alternative for flexible materials……...115
Figure 4.5. Fluid filling speed over time for rectangular microfluidic channels, including the relative errors, for rectangular microfluidic channels fabricated using: (a) PDMS/Glass/PDMS/PDMS and β = 1; (b) PDMS/Glass/PDMS/PDMS and β = 1.3; (c) PVA/Glass/Tape/Tape and β = 0.1; (d) PVA/Glass/Tape/Tape and β = 0.2.…….119
Figure 4.6. a-b) Start of flow within the fully flexible microfluidic system, activated solely by capillarity; c-e) progressive coverage of the entire plasmonic sensor positioned within the microfluidic chamber (gold nanoparticle cluster on PDMS); f) end of flow and complete filling of the designed structure. 120
Figure 4.7. a) Fully flexible sensor integrated with the microfluidic pump and elliptical chamber containing AuNP clusters. b-c) Capillary-driven filling of the system, illustrating uniform liquid distribution without external support ……..121
Figure 5.1 Schematic representation of a capillary-driven microfluidic circuit for optical sensing applied directly to the skin, including the filling and rinsing process of the system when in contact with the skin. ……..129
Figure 5.2 Sketch of HOE- based PDMS waveguide sensor.....129
Figure A. Example of meshing a microfluidic structure in COMSOL Multiphysics.....133
Figure B. ISASI's group Clean room.....148
Figure B.3. Reactive Ion Etching technique (RIE) machine.....155
Figure B.4. Mask Aligner Machine.....156
Figure B.4. Laser Writer 158
Figure B.4. Cutter Plotter for Xurography 160
Figure B.4. Plasma Enhanced Chemical Vapor Deposition (PECVD) machine……..…155

Figure C.1 a) Schematic of HOE recording and reconstruction process, illustrating the setup for interference recording and the subsequent reconstruction phase; b) Laboratory setup for HOE recording; c) PDMS waveguide with an HOE applied to its surface, deflecting a 532 nm light beam and enabling total internal reflection (TIR) within the material.....174
Figure C.2. a) PDMS microfluidic system with methylene blue dye solution attached to glass; b) Excitation of the dye chamber with a 633 nm in-coupler and 700 nm out-coupler; c) Spectrum of the in-coupled (excitation - 633nm) signal and the out-coupled (fluorescent dye solution – 700nm) signal from the system. 175

Abstract

This thesis presents a research path focused on the development and optimization of microdevices using flexible materials for biochemical detection, with a particular emphasis on creating portable, cost-effective, and versatile solutions. The primary aim was to transform initially rigid and complex devices into flexible, compact, and autonomous platforms suitable for continuous monitoring and field diagnostic applications. Through a multidisciplinary approach, the research has successfully addressed significant technical challenges, enhancing fluid transport and management in microchannels while pursuing miniaturization and operational simplicity without compromising detection efficiency. Each device was developed through three interlinked phases: design, fabrication, and characterization. These phases interact in a continuous cycle of improvement, enabling progressive optimization of each performance of the device. The thesis begins with the development of a microsystem that I designed and fabricated to optimize the functionalization of a rigid optical sensor with gold nanoparticles for biochemical detection. A detailed design and simulation of the microchannel geometry played a fundamental role, allowing for uniform flow distribution, reduction of stagnant zones, and a substantial increase in sensor sensitivity. Experimental measurements, conducted in collaboration with the University 'Magna Graecia' of Catanzaro, confirmed the effectiveness of the functionalization, demonstrating high uniformity in coverage and quality of the plasmonic substrate, with the microfluidic system able to maintain a stable and reproducible flow. These promising results motivated further development toward a fully flexible microdevice, resulting in the creation of a plasmonic sensor on soft materials like Polydimethylsiloxane (PDMS). This material was strategically chosen for its biocompatibility and stability, making it ideal for flexible biomedical devices. The thesis provides a detailed description of the device design, microfabrication techniques, and characterization methodologies used. Experimental tests conducted with spectroscopy and fluorescence microscopy confirmed the effectiveness of the flexible structure, showcasing high performance, signal amplification, and accurate biomarker detection, even in dynamic conditions. The

research aims to create autonomous, portable, and compact devices. To enhance portability and reduce complexity, the project focused on eliminating external pumps by developing an autonomous fluid transport system based on capillarity. This system utilizes the surface properties of microchannel walls to drive the spontaneous movement of fluids, proving to be a promising solution. During my research period at the Vrije Universiteit Brussel (VUB), I deepened my understanding of capillary phenomena, focusing on the wettability of surfaces relevant in microfluidic systems. The research group I joined specialized in cryogenic measurements, and my contribution involved analyzing and developing numerical models to predict the capillary behavior of sample droplets on cryo-EM grids, essential for cryogenic applications. The study of capillary spreading and surface wettability proved critical in this context, as uniform sample distribution on grids allows for optimal sample thickness, enhancing the quality of cryogenic images. This work led me to design new grid prototypes that facilitate effective droplet spreading, thereby improving the performance of cryo-EM measurements. Applying these insights led to the development of microfluidic devices with integrated capillary pumping systems, exploring fluid flow in microchannels made from materials with variable wettability. This work required creating a general analytical model to predict capillary flow dynamics under non-uniform conditions, as existing literature lacked a clear and comprehensive treatment of these phenomena with varying channel wettability. The model focused particularly on the transient regime, crucial for determining subsequent flow behavior. Experimental validation was carried out with devices fabricated through soft lithography and xurography, demonstrating the model's accuracy and versatility and establishing a basis for precise fluid transport control in microfluidic systems. The next phase of the project will focus on the integration of holographic diffractive elements (HOEs) to optimize optical path management, enhancing sensor efficiency and compactness. A key objective will be the integration of a PDMS waveguide, designed to utilize total internal reflection (TIR) to confine light and direct it precisely towards the optical sensors. A collaboration with TU Dublin is already underway, and initial tests have shown promising results. The combination of HOEs with PDMS will enable light to be deflected at angles beyond the critical angle, keeping it contained within the waveguide and ensuring optimal signal management.

Introduction

"There is plenty of room at the bottom"—with these words, Richard Feynman inaugurated a new era in science in 1959, anticipating the potential of miniaturization. This phrase, delivered during a historic conference at *Caltech*, expressed a forward-looking vision: the future of technology would lie in our ability to control and manipulate materials and devices at the atomic and molecular level [1]. Today, miniaturization represents not only a technological achievement but also a necessity in the biomedical field, where the precision and efficiency of microsystems are transforming how we approach diagnosis and therapy.

From the discovery of the optical microscope to modern *lab-on-chip* devices, the reduction in the size of analytical systems has led to remarkable advances in medicine, paving the way for new possibilities in diagnostics and treatment. Miniaturization now enables the use of flexible, portable, and implantable devices capable of operating directly within the human body with molecular precision [2].

An example of this evolution is the shift from large, cumbersome clinical analyzers to portable devices based on micro and nanochips. These not only reduce production costs but also make diagnostics faster and more accessible, with minimal impact on laboratory resources. Their ability to integrate multiple functions into a single device allows for the automation of complex tests with reduced consumption of reagents and energy, finding applications in both healthcare and home care settings.

The growing demand for portable and wearable diagnostic solutions has also driven the development of sensors made from flexible materials. These materials, ranging from elastic polymers to biocompatible and biodegradable compounds, have opened new possibilities in health monitoring, real-time

diagnostics, and drug delivery. Their flexibility and ability to adapt to complex and dynamic surfaces make these microsystems ideal for wearable or implantable applications, allowing for direct interaction with the soft tissues of the human body [3-4].

Flexible microsystems utilize materials with unique mechanical and optical properties, including elasticity, transparency, and biocompatibility. Polymer materials such as polydimethylsiloxane (PDMS), hydrophilic gels (like alginate-based hydrogels), and biodegradable materials are gaining increasing attention for their biomedical applications [5]. PDMS is one of the most commonly used materials for developing flexible microsystems. It is an organic elastomer with excellent elasticity, chemical inertness, thermal stability, and non-toxicity. Its high transparency makes PDMS particularly useful in optical and sensory applications. PDMS-based microsystems can be fabricated using replica molding techniques, allowing the creation of sensors capable of withstanding mechanical deformation without compromising their functionality [6].

Sensors integrated into these microdevices can monitor parameters such as heart rate, blood pressure, body temperature, and blood oxygen saturation. Made with flexible materials, they adhere perfectly to the skin, ensuring comfort and precise, continuous data collection, even when integrated into clothing [6-7]. Implantable microsystems, on the other hand, allow for monitoring biochemical parameters like glucose or oxygen levels in the blood, transmitting real-time data and enabling continuous control without the need for frequent blood draws [8]. Implantable devices made from biodegradable materials can provide consistent and timed dosages, eliminating the need for frequent administrations. This approach is particularly effective in treating chronic diseases like cancer, where continuous drug delivery can enhance therapeutic efficacy and reduce side effects [9].

The complexity and effectiveness of these multifunctional microsystems derive from the integration of technologies from various disciplines, such as microfluidics, sensing (optical, electrochemical, piezoresistive, etc.), and electronics. Microfluidics, in particular, facilitates the handling of small volumes of biological samples, aiding in separation and analysis, while sensors detect

physiological or biochemical changes [10]. Finally, electronics manage data processing and device power, as well as ensure wireless data transmission [11]. A significant example of this integration is represented by Lab-on-Chip (LOC) systems, which combine microfluidics, sensors, and electronics on a miniaturized platform capable of replicating many laboratory functions. These systems are particularly useful in point-of-care diagnostics, providing rapid and accurate analyses directly at the side of patient, thereby improving healthcare management efficiency. LOCs enable precise control of tiny fluid volumes, integrating bioanalytical operations into a single chip, with applications ranging from medical diagnostics to environmental monitoring [13-15].

My thesis focuses on the study of flexible materials for the development of microfluidic systems intended for biochemical applications. The focus has been on developing devices by transforming complex and rigid structures into flexible platforms that are more cost-effective and, above all, more autonomous, with the goal of creating compact and portable tools suitable for continuous monitoring.

Each device developed and presented in this thesis work follows a structured process consisting of three fundamental and interconnected phases: design, fabrication, and characterization. These phases influence each other, creating a continuous refinement cycle that allows for the progressive optimization of each device.

In the design phase, I utilized numerical simulations to support the selection of the most suitable microfluidic geometry. This approach allowed for a detailed understanding of fluid behavior and properties under various conditions and how these interact with the shape of microchannel. Each device was designed using COMSOL Multiphysics software, which employs the Finite Element Method (FEM) to solve partial differential equations in various fields of physics. The COMSOL Microfluidics module offers advanced tools for studying microfluidic devices and is widely used for designing lab-on-chip devices, biosensors, and electrokinetics devices [16-20]. This rigorous design process ensured that the chosen geometries effectively controlled fluid dynamics (Appendix A).

In the fabrication phase, advanced techniques were employed, such as soft lithography, replica molding [21], as well as metal deposition and evaporation techniques, carried out in top-tier laboratories (Clean Room at ISASI-CNR in Naples, Appendix B). Additionally, I explored more accessible methods like xurography [22-23], which can be executed with standard commercial cutter plotters and do not require specialized facilities. This dual approach allowed for the production of microfluidic devices that varied in complexity and cost-effectiveness.

In the characterization phase, various techniques were employed to thoroughly assess the structural and functional properties of the devices. Optical microscopy was used for preliminary surface analysis, while atomic force microscopy (AFM) provided detailed evaluations of topography and roughness. Profilometer measurements were conducted to accurately determine the coating thickness, and scanning electron microscopy (SEM) offered high-resolution images for more precise morphological analysis (Appendix B). Fluorescence microscopy was used to study specific optical characteristics and the distribution of fluorescent materials, followed by Raman spectroscopy to analyze the chemical composition and molecular properties of the samples. Additionally, optical, flow, and mechanical measurements were performed according to the specific requirements of each device, ensuring a comprehensive characterization and that the devices met the necessary performance standards for biochemical applications.

In this thesis, I will showcase the journey that led me to tackle initial challenges and seek innovative solutions through a multidisciplinary approach. This enabled me to overcome technical limitations and significantly enhance the effectiveness and accuracy of microfluidic systems.
My thesis is structured as follows.

Chapter 1. The first objective of my work was to conduct an in-depth study to develop a microfluidic system aimed at optimizing the functionalization of a plasmonic sensor within it. Plasmonic sensors have represented one of the

main innovations in the field of nanotechnology in recent years. In these devices, the interaction between metallic nanostructures and light radiation induces a collective oscillation of electrons on the surface of the metal, a phenomenon known as localized surface plasmon resonance [24-25]. This resonance generates a significant amplification of the electromagnetic field near the metallic surface, which can be exploited to enhance fluorescence and/or Raman signals on the nanometallic surface. This field amplification mechanisms, known respectively as Metal-Enhanced Fluorescence (MEF) and Surface-Enhanced Raman Spectroscopy (SERS) [26-31], offer extremely high sensitivity, enabling the detection of analytes or biomarkers at ultra-low concentrations, potentially down to single-molecule resolution. Despite numerous scientific successes in the fabrication of plasmonic substrates, the industrial application of this technology remains limited. While early plasmonic prototypes demonstrated high resolution and sensitivity with low detection limits, they suffered from moderate selectivity and specificity, hindering their large-scale use for biomedical applications. Indeed, when analyzing complex samples such as blood, an ideal plasmonic device must be capable of selectively identifying the biomarker of interest among many other components present in the sample.

In this study, I analyzed how to improve the functionalization of a plasmonic substrate within a microsystem, focusing on selectivity and uniformity. The plasmonic sensor consists of an array of gold nanoparticle clusters on a rigid silicon substrate. I designed and optimized the geometry of the microfluidic system to ensure a uniform distribution of chemical compounds toward the active sites of the substrate. The optimization aimed to minimize dead zones, areas where flow is absent or greatly reduced, to ensure that every part of the sensor was exposed for the same amount of time to the target chemical species. The ultimate goal was to functionalize the substrate with cysteine and folic acid complexes (C-FA) to selectively capture folic acid receptors (A-FA). Tumor cells often express folate receptors (A-FA) in higher quantities than healthy cells. Therefore, targeting these receptors with a device using C-FA as a ligand allows for the selective identification and isolation of tumor cells. The flow rates necessary for optimal functionalization were estimated through numerical

simulations and validated through Raman and fluorescence measurements conducted at various points on the device. These experiments confirmed the uniformity of the functionalization, along with high specificity and selectivity, while maintaining high standards of sensitivity and resolution. A device designed in this way could improve the rapid and efficient identification and detection of cancer cells in liquid biopsy samples.

Chapter 2. In this chapter, I aim to develop a completely flexible device, representing a significant advancement over the previous work, which required the design of a plasmonic system on a soft material. Traditional plasmonic devices typically consist of gold or silver nanoparticles of varying sizes and shapes in the nanometer range, placed on rigid, planar substrates, usually made of silicon (as in the first work) or silicon dioxide. However, in recent years, the development of plasmonic metal nanostructures on soft materials has gained traction, offering advantages over traditional substrates, such as lightweight, low cost, high flexibility, and better mechanical properties. These characteristics have paved the way for new applications, such as active optical tuning, wearable plasmonic devices for detecting biochemical species, health monitoring sensors, and strain detection applications [33-37]. Following these trends, I demonstrated the functionalization of flexible PDMS membranes with gold nanoparticle clusters. Specifically, μm-thick membranes were produced through spin coating and polymerization processes of PDMS. The device was then functionalized with human immunoglobulin G (IgG), demonstrating the ability to recognize, capture, and amplify human antibodies, as confirmed through fluorescence analysis. Additionally, the sensing capabilities of the device were evaluated through Raman spectroscopy, which enabled the detection of interleukin 8 (IL8), a clinically relevant biomarker associated with inflammatory responses and immune system regulation. Raman measurements confirmed the device's ability to detect IL8 with high sensitivity, further validating its potential for biochemical sensing applications. Although a good level of sensor flexibility has been achieved, sufficient compactness for a fully integrated device has not yet been obtained. For this reason, future developments will focus on enhancing the compactness of the device, with the

first step aimed at eliminating external components, such as flow pumps, to create a more compact solution. Specifically, attention has been directed toward the development of capillary microfluidic systems, where the fluid motion is driven solely by the surface properties of the materials involved. Capillarity was extensively studied during the research period at the Vrije Universiteit Brussel (VUB) in Belgium for a specific application, which will be discussed in the next chapter.

Chatpter 3. As previously mentioned, capillary phenomena were thoroughly studied during the research experience in Belgium. Specifically, the influence of capillary phenomena was explored for a particular application in Cryo-EM. Cryo-EM (Cryogenic Electron Microscopy) is a technique that allows for the observation of biological samples at cryogenic temperatures, preserving their natural structure without the need for chemical fixatives. This technology is particularly useful for studying complex molecular structures with extremely high resolution [48-50]. During my research, I focused on the spreading capillary dynamics of a sample droplet on a Cryo-EM grid. The droplet, generated through optical cavitation using a laser within a microfluidic circuit, impacts the grid. Specifically, I analyzed the behavior of a single cell of the cryogenic grid. To identify the optimal configuration for droplet spreading, I conducted numerical simulations on three different types of Cryo-EM grid cells: the simple cell, the one with pillars, and the one with channels, considering parameters such as contact angle and other geometric factors. The analysis was performed using COMSOL Multiphysics for precise tracking of the interface between the liquid sample and the impact surface of the cell. The analysis of the droplet impact highlighted its shape and the velocity field during spreading on a solid substrate with characteristics similar to those of grids used in Cryo-EM. The results obtained from the numerical simulation were compared with experimental data, showing a good correspondence regarding the parameters of droplet spreading.

Chapter4. With the knowledge acquired in Belgium on capillarity, I focused my work on developing a flexible capillary microfluidic device capable of ensuring a satisfactory level of compactness and autonomy. Indeed, in a passive

microfluidic system, the flow is determined solely by the design of the device itself. The main forces driving liquids in these systems include surface chemical gradients, osmotic pressure, and, most importantly, capillary forces. In capillary systems, the spontaneous movement of a fluid over a surface is governed by the interaction between the surface tension of liquid and the intrinsic properties of the solid surface. This interaction can be exploited to automatically fill microstructures and to guide and transport liquids along defined paths [42-47]. Despite the growing interest in capillary flow microfluidic systems, there were still no clear and comprehensive studies on fluid dynamics in channels with walls made of materials with different wettability properties. Moreover, the behavior of the fluid during the initial moments of channel filling had not been thoroughly investigated. This motivated the development of an ad hoc theory for my case study, particularly an experimentally validated-generalized analytical approach, capable of dynamically predicting the displacement and velocity of the meniscus, influenced solely by capillary forces. The developed model allows for accurate estimation of the average capillary flow velocity within a three-dimensional rectangular microfluidic channel, taking into account the complex interactions between the fluid and the channel walls due to differing wettability properties. This makes it applicable to capillary microfluidic systems fabricated using both traditional and sophisticated techniques, as well as to more recent and cost-effective methods. The model was validated with microfluidic devices fabricated using some of these techniques, demonstrating its versatility and precision. Furthermore, the capillary filling process was demonstrated in a flexible microfluidic system with an integrated plasmonic sensor. The system was shown to fill effectively, even when subjected to significant curvature.

Chatpter 5. In this concluding chapter, the results obtained throughout the research journey are summarized, highlighting how complex problems were addressed and solved step by step through a multidisciplinary approach aimed at developing compact, autonomous, and flexible devices. The next phase of device development will focus on further miniaturization and portability, with specific attention to optimizing illumination and signal detection systems, essential aspects for creating a fully flexible and autonomous biosensor. Within

a fully PDMS-based microfluidic device, the focus will shift to an innovative approach in optical pathway control. Specifically, the goal is to integrate holographic diffractive elements (HOE) that enable total internal reflection (TIR) within the PDMS [38]. These elements are designed to deflect light at an angle greater than the critical angle, calculated using Snell's law, trapping the light within the PDMS and defining a precise optical path that accurately reaches the area of interest, represented in this case by the optical sensor. Preliminary implementation tests of this technology have already been conducted on the materials used, and future prospects foresee the full integration of these elements into the sensor. The results obtained provide a solid foundation for future developments, opening new perspectives in the field of miniaturization and optimization of portable and autonomous biosensors. These devices have the potential to transform the landscape of biomedical applications, enabling faster and more precise diagnoses and improving health monitoring.

My research journey highlights the importance of a multidisciplinary approach in the field of biomedical applications. This approach not only allows us to optimize device performance but also ensures greater effectiveness in practical applications, such as the early diagnosis of diseases and health monitoring. The synergy between different areas of knowledge translates into more integrated and comprehensive solutions, thus contributing to significant advancements in the field of biomedicine and opening new avenues for improving quality of life.

References

1. Feynman, R.P., There's Plenty of Room at the Bottom, Engineering and Science, Caltech, 1960.

2. Toumey, C., Plenty of Room, Plenty of History, Nature Nanotechnology, 2009.

3. Dong, L., Xia, P., Wei, D., Flexible and Wearable Sensors for Biomedical Applications, Micromachines, 2022, 13(9), 1395.

4. Lima, R., Minas, G., Properties and Applications of PDMS for Biomedical Engineering: A Review, J. Funct. Biomater., 2022, 13(1), 2.

5. Polydimethylsiloxane (PDMS)-Based Flexible Resistive Strain Sensors for Wearable Applications, MDPI, 2022.

6. Fiala, J. et al., An Implantable Optical Blood Pressure Sensor Based on Pulse Transit Time, Biomed Microdevices, 2013.

7. Su, Z. et al., Wearable and Implantable Biosensors: Mechanisms and Applications in Closed-Loop Therapeutic Systems, J. Mater. Chem. B, 2023.

8. Hasanzadeh, A., Smartphone-Based Microfluidic Devices for Biomedical Applications, 2021.

9. Iguchi, S. et al., A Flexible and Wearable Biosensor for Tear Glucose Measurement, Biomed Microdevices, 2007.

10. García-Carmona, L. et al., Pacifier Biosensor: Toward Noninvasive Saliva Biomarker Monitoring, Anal. Chem., 2019.

11. Fiore, L. et al., Microfluidic Paper-Based Wearable Electrochemical Biosensor for Reliable Cortisol Detection in Sweat, Sens. Actuators B Chem., 2023.

12. Dutse, S.W., Yusof, N.A., Microfluidics-Based Lab-on-Chip Systems in DNA-Based Biosensing: An Overview, Sensors, 2011.

13. Pilloton, R., Lab-on-Chip and Microfluidic Sensors, MDPI, 2021.

14. Giménez-Gómez, P., Pilloton, R., Advanced Microfluidic Devices and Lab-on-Chip (Bio)sensors, MDPI, 2022.

15. Dutse, S.W., Yusof, N.A., Microfluidics-Based Lab-on-Chip Systems for Pathogen Detection, Sensors, 2011.
16. Zienkiewicz, O.C., Taylor, R.L., The Finite Element Method. Volume 1: The Basis, Fifth Edition, Butterworth-Heinemann, 2000.
17. Lewis, R.W., Nithiarasu, P., Seetharamu, K.N., Fundamental of the Finite Element Method for Heat and Fluid Flow, John Wiley & Sons, 2004.
18. Pryor, R.W., Multiphysics Modeling Using COMSOL: A First Principles Approach, Jones and Bartlett Publishers, 2009.
19. Zimmerman, W.B.J., COMSOL Process Modeling and Simulation with Finite Element Methods, World Scientific Publishing Co. Pte. Ltd., 2004.
20. COMSOL Multiphysics Documentation: The Microfluidics Module.
21. McDonald, J.C., Duffy, D.C., Anderson, J.R., et al., Fabrication of Microfluidic Systems in Poly(dimethylsiloxane), Electrophoresis, 2000, 21, 27–40.
22. Shahriari, S., Patel, V., Selvaganathy, P.R., Xurography as a Tool for Fabrication of Microfluidic Devices, Journal of Micromechanics and Microengineering, 2023.
23. Neuville, A., Renaud, L., Luu, T.T., et al., Xurography for Microfluidics on a Reactive Solid, Lab on a Chip, 2017.
24. Brolo, A.G. (2012). Plasmonics for future biosensors. Nature Photonics, 6(11), 709-713.
25. Bauch, M., Toma, K., Toma, M., Zhang, Q., & Dostalek, J. (2014). Plasmon-enhanced fluorescence biosensors: a review. Plasmonics, 9, 781-799.
26. Kneipp, J., Kneipp, H., & Kneipp, K. (2008). SERS—a single-molecule and nanoscale tool for bioanalytics. Chemical Society Reviews, 37, 1052–1060.
27. Kneipp, K. (2007). Surface-enhanced Raman scattering. Physics Today, 60, 40–47.
28. Kneipp, K., Kneipp, H., Abdali, S., Berg, R., & Bohr, H. (2004). Single molecule Raman detection of Enkephalin on silver colloidal particles. Spectroscopy, 18, 433–440.
29. Kneipp, K., Wang, Y., Perelman, L.T., Itzkan, I., Dasari, R.R., & Feld, M.S. (1997). Single molecule detection using surface-enhanced Raman scattering (SERS). Physical Review Letters, 78, 1667–1670.

30. Battista, E., Coluccio, M.-L., Alabastri, A., Barberio, M., Causa, F., Netti, P.-A., Di Fabrizio, E., & Gentile, F. (2017). Metal-enhanced fluorescence on super-hydrophobic clusters of gold nanoparticles. Microelectronic Engineering, 175, 7–11.

31. Deng, W., Xie, F., Baltarac, H.T.M.C.M., & Goldys, E.M. (2013). Metal-enhanced fluorescence in the life sciences: here, now and beyond. Physical Chemistry Chemical Physics, 15, 15695–15708.

32. Ray, K., & Lakowicz, J.R. (2013). Metal-enhanced fluorescence lifetime imaging and spectroscopy on a modified SERS substrate. The Journal of Physical Chemistry C, 117, 15790–15797.

33. Gontier, A., Marae-Djouda, J., Hmima, A., Proust, J., Bercu, N.-B., Le Joncour, L., Stagon, S., Konoplev, G., Tarasov, S.-A., Adam, P.-M., Gardan, J., Panicaud, B., Molinari, M., & Maurer, T. (2020). Flexible plasmonic and strain sensors: fabrication, design and perspectives. IOP Conference Series: Journal of Physics, 1461, 012096.

34. Kumari, S., Mohapatra, S., & Moirangthem, R.S. (2018). Development of flexible plasmonic sensor based on imprinted nanostructure array on plastics. Materials Today: Proceedings, 5, 2216–2221.

35. Song, L., Chen, J., Xu, B.B., & Huang, Y. (2021). Flexible plasmonic biosensors for healthcare monitoring: progress and prospects. ACS Nano, 15, 18822–18847.

36. Torino, S., Conte, L., Iodice, M., Coppola, G., & Prien, R.D. (2017). PDMS membranes as sensing element in optical sensors for gas detection in water. Sens. Bio-Sens. Res., 16, 74–78.

37. Peng, J., Jeong, H.-H., Smith, M., Chikkaraddy, R., Lin, Q., Liang, H.-L., De Volder, M.-F.-L., Vignolini, S., Kar-Narayan, S., & Baumberg, J.J. (2021). Fully printed flexible plasmonic metafilms with directional color dynamics. Advanced Science, 8, 2002419.

38. Close, D.H. (1975). Holographic optical elements. Optical Engineering, 14(5), 408–419.

39. Xu, L., Wang, A., Li, X., & Oh, K.W. (2020). Passive micropumping in microfluidics for point-of-care testing. Biomicrofluidics, 14.

40. Elizalde, E., Urteaga, R., Koropecki, R.R., & Berli, C.L. (2014). Inverse problem of capillary filling. Physical Review Letters, 112, 134502.
41. Kolliopoulos, P., Jochem, K.S., Johnson, D., Suszynski, W.J., Francis, L.F., & Kumar, S. (2021). Capillary-flow dynamics in open rectangular microchannels. Journal of Fluid Mechanics, 911, A32.
42. Wang, X., Liu, Z., & Pang, Y. (2017). Concentration gradient generation methods based on microfluidic systems. RSC Advances, 7, 29966–29984.
43. Bayraktar, T., & Pidugu, S.B. (2006). Characterization of liquid flows in microfluidic systems. International Journal of Heat and Mass Transfer, 49, 815–824.
44. Gervais, L., & Delamarche, E. (2009). Toward one-step point-of-care immunodiagnostics using capillary-driven microfluidics and PDMS substrates. Lab on a Chip, 9, 3330–3337.
45. Safavieh, R., & Juncker, D. (2013). Capillarics: pre-programmed, self-powered microfluidic circuits built from capillary elements. Lab on a Chip, 13, 4180–4189.
46. Olanrewaju, A., Beaugrand, M., Yafia, M., & Juncker, D. (2018). Capillary microfluidics in microchannels: from microfluidic networks to capillaric circuits. Lab on a Chip, 18, 2323–2347.
47. Safavieh, R., Tamayol, A., & Juncker, D. (2015). Serpentine and leading-edge capillary pumps for microfluidic capillary systems. Microfluidics and Nanofluidics, 18, 357–366.
48. Yip, K.M., Fischer, N., Paknia, E., Chari, A., & Stark, H. (2020). Atomic-resolution protein structure determination by cryo-EM. Nature, 587(7832), 157-161.
49. Fischer, N., Konevega, A.L., Wintermeyer, W., Rodnina, M.V., & Stark, H. (2010). Ribosome dynamics and tRNA movement by time-resolved electron cryomicroscopy. Nature, 466(7304), 329–333.
50. Chen, B., Kaledhonkar, S., Sun, M., Shen, B.X., Lu, Z.H., Barnard, D., Lu, T.M., Gonzalez, R.L., & Frank, J. (2015). Structural dynamics of ribosome subunit association studied by mixing-spraying time-resolved cryogenic electron microscopy. Structure, 23(6), 1097–1105.

1
Microfluidic Device for Biomarker Detection using Plasmonic Sensor

In this chapter, I describe the development of a microfluidic system aimed at optimizing the functionalization of a plasmonic sensor within it, starting from the theoretical basis of plasmonics. I introduce Localized Surface Plasmon Resonance (LSPR) and its importance in electromagnetic signal amplification, followed by its integration with microfluidics for precise control of sample flow. The device features a PDMS microfluidic chip incorporating a plasmonic sensor composed of gold nanoparticle clusters on a rigid silicon substrate, sealed with a glass layer (Fig. 1). Using a Cysteine-Folic Acid complex, it detects Anti-Folic Acid expressed by tumor cells, with potential for isolating and identifying circulating tumor cells from liquid biopsy samples. Compact in design, it is compatible with Raman and fluorescence microscopy for real-time analysis. The system was developed through design, fabrication, and characterization phases. Optical measurements confirmed that combining microfluidics with plasmonics enhances functionalization, greatly improving sensor performance and making it ideal for advanced biomedical applications [1].

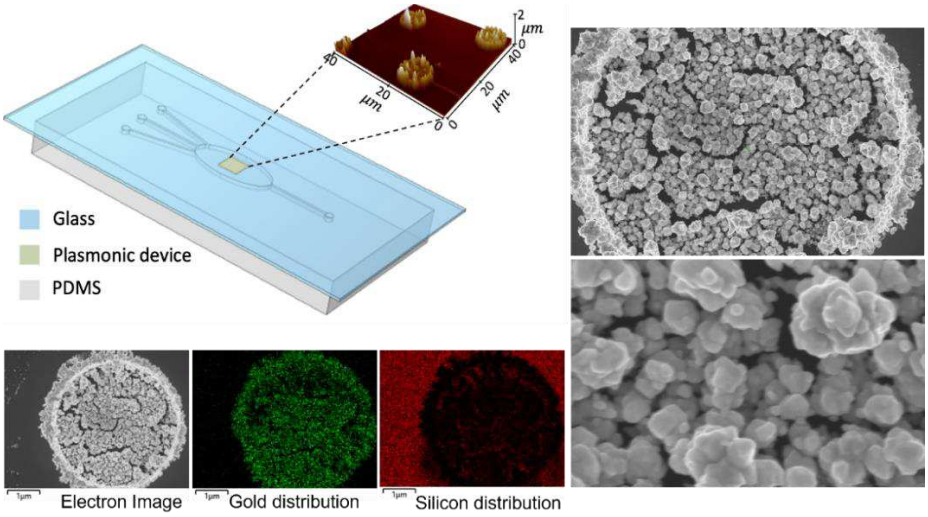

Figure 1 Sketch of the microfluidic device made of flexible PDMS material, integrating a plasmonic sensor based on gold nanostructure clusters deposited on a rigid silicon substrate. The figure also includes SEM images of the optical sensor and its corresponding chemical composition map.

1.1 Introduction to Plasmonic Sensors

Plasmon resonance is a phenomenon that occurs when the conduction electrons on the surface of a metallic nanostructure oscillate collectively in response to an incident electromagnetic wave. When this phenomenon takes place in a structure whose size is much smaller than the wavelength of the incident light, it is referred to as LSPR. The primary effect of LSPR is an amplification of the electromagnetic field in the immediate vicinity of the nanostructure [2-5].

The fundamental principles of LSPR can be explained through the interaction between light and free electrons in metals, an interaction described by Maxwell's equations and the Drude model, which governs the motion of electrons in metals. The resonance condition for LSPR is satisfied when the frequency of the incident light (ω) meets the following relation:

$$Re\{\epsilon_{met}(\omega)\} = -2\epsilon_m$$

- ϵ_{met} is the complex dielectric constant of the metal.
- ϵ_m is the dielectric constant of the surrounding medium.

Known as the Frohlich condition.

The amplification of the electromagnetic field is strongly influenced by the size, shape, and material of the nanostructure, as well as the dielectric properties of the surrounding environment. The amplitude of the electric field |E| near the surface can be described by the following relation:

$$|E| \approx |E_0| \cdot \frac{R}{\lambda} \left| \frac{\epsilon_{met} - \epsilon_m}{\epsilon_{met} + \epsilon_m} \right|$$

where:

- $|E_0|$ is the amplitude of the incident electric field,
- R is the radius of the metallic nanoparticle,
- λ is the wavelength of the incident light,

The amplification of the electromagnetic field near the surface of a metallic nanostructure has numerous applications. In this thesis, we will explore two

related phenomena: Metal-Enhanced Fluorescence (MEF) and Surface-Enhanced Raman Spectroscopy (SERS).

Metal-Enhanced Fluorescence: MEF [13] occurs when a fluorescent molecule (fluorophore) is in close proximity to a metallic surface. The amplified electromagnetic field in the local area increases the excitation rate of the fluorophore, resulting in an enhancement of fluorescence intensity. The increase in fluorescence I_{MEF} can be expressed as:

$$I_{MEF} = I_0 \cdot (\frac{|E|}{|E_0|})^2$$

where:

- I_0 is the initial fluorescence intensity in the absence of the metallic nanostructure,
- $|E|$ is the amplitude of the amplified electric field generated by the plasmonic nanostructure,
- $|E_0|$is the amplitude of the incident electric field.

The term $(\frac{|E|}{|E_0|})^2$ represents the local amplification of the electromagnetic field, which is responsible for the observed increase in the fluorescence of the fluorophore intensity.

Surface-Enhanced Raman Spectroscopy: SERS [10-12] is a powerful analytical technique that exploits the amplification of the electromagnetic field induced by LSPR to enhance the intensity of Raman signals. The Raman signal intensity I_{SERS} is proportional to the fourth power of the local electromagnetic field:

$$I_{SERS} = I_0 \cdot (\frac{|E|}{|E_0|})^4$$

- I_0: represents the intensity of the Raman signal without the presence of the plasmonic nanostructure. This is the baseline value of the Raman signal that would be obtained under normal conditions, without amplification.

- $|E_0|$: is the amplitude of the electric field of the incident light before interacting with the plasmonic nanostructure. This field represents the light striking the sample without any amplification.
- $|E|$: is the amplitude of the local electric field amplified by the plasmonic nanostructure as a result of surface plasmon resonance. This enhanced field is responsible for the significant increase in Raman signal intensity.

This fourth-power dependence occurs because both the incident light and the scattered Raman light experience electromagnetic field amplification. As a result, SERS can achieve signal enhancements of up 10^6 to 10^{10}, allowing for the detection of molecules at ultra-low concentrations, even down to the single-molecule level.

The resonance frequency of LSPR and the associated field amplification are highly sensitive to variations in the surrounding dielectric environment. A small change in the refractive index n or ε_m the dielectric constant of the medium near the metallic surface will cause a shift in the LSPR resonance frequency, which can be exploited for detection applications. This sensitivity is quantified by the refractive index sensitivity S, defined as:

$$S = \frac{\Delta\lambda_{LSPR}}{\Delta_n}$$

where $\Delta\lambda_{LSPR}$ is the variation in the resonance wavelength due to a change $\Delta_n$in the refractive index. Higher values of S indicate greater sensitivity of the plasmonic sensor to changes in the local environment, making LSPR-based devices highly suitable for detecting biological and chemical species in complex samples.

The phenomenon of LSPR provides an ideal platform for developing highly sensitive optical sensors, thanks to its ability to locally amplify the electromagnetic field. This amplification effect supports techniques such as MEF and SERS, enabling the detection of analytes at ultra-low concentrations. In our work, this principle was utilized in the development of a plasmonic device consisting of an array of gold nanoparticle clusters on a silicon substrate, fabricated using low-cost techniques such as optical lithography and electroless

deposition. The ability to modulate the LSPR properties by varying the geometry of the nanostructures and the surrounding medium enhances the versatility of the sensor, making it particularly suitable for applications in biosensing, diagnostics, and environmental monitoring.

1.2 Plasmonic-Based Biosensing

Microfluidics allows for the precise manipulation of fluids in extremely small volumes within microchannels, revolutionizing diagnostics and other biomedical applications. It optimizes the management of samples and reagents, reducing both consumption and reaction times.

The integration of microfluidics with plasmonic sensing is of great interest, as highly controllable microfluidic systems efficiently manage the analyte, directing it precisely to the active areas where plasmonic sites are located. This optimized control enhances biochemical interactions, reduces reagent consumption, and ensures that the sample is exposed only to the desired sensing surfaces. Additionally, microfluidics enables the regulation of key parameters such as flow rate, exposure time, and sample distribution, improving both sensitivity and accuracy in measurements. The integration with advanced techniques such as MEF and SERS, which leverage plasmonic resonance amplification, allows for the detection of biomarkers at extremely low concentrations, making this technology critical for advanced biomedical applications [14-16].

PDMS is widely used in the fabrication of microfluidic systems due to its excellent mechanical and optical properties, as well as its biocompatibility. Its elasticity and transparency make it ideal for creating complex microchannels, ensuring optimal optical coupling with plasmonic sensors. Transparency of PDMS in the visible range facilitates illumination and the collection of optical signals, which are critical for ensuring precise and reliable measurements.

This integration is particularly advantageous in lab-on-chip applications, where the combination of microfluidics and LSPR enables sophisticated analyses on miniaturized platforms, allowing for the detection of biomarkers at ultra-low concentrations and real-time monitoring of optical signals. Thanks to its transparency, PDMS simplifies the acquisition of signals necessary for the proper functioning of plasmonic sensors, ensuring accurate and reproducible results [17-21].

In my work on the development of microfluidic devices integrated with plasmonic sensors on a rigid silicon substrate, I focused on optimizing the functionalization through microfluidics to increase the selectivity of the sensor. The development process described in this thesis follows the three main phases for each device: design, fabrication, and characterization.

1.3 Design

The geometric design of the microfluidic system is critical to ensure uniform functionalization of the plasmonic surface. I developed the design of the microfluidic chamber by considering key geometric parameters such as shape, size, and the configuration of the inlet and outlet channels. To optimize these aspects, I conducted numerical simulations using COMSOL Multiphysics (ver. 6.0)[22]. COMSOL, through finite element analysis (FEM), allowed me to precisely study the flow distribution within the chamber, evaluating how geometry affects the velocity profile and fluid concentration. The numerical analyses enabled accurate predictions of system performance, optimizing the design to ensure uniform flow and optimal fluid distribution on the plasmonic surface, thus improving the overall sensor efficiency.

The system was designed with three inlet channels, a central ellipsoidal chamber, and an outlet channel (Fig. 1.1). The ellipsoidal shape of the chamber, which hosts the plasmonic device, was chosen to avoid the formation of dead zones—areas where the fluid flows very slowly, leading to non-uniform solute distribution. In these zones, the functionalization of the gold nanostructures could be ineffective, and the concentration of the target receptor may be too low.

The ellipsoidal geometry was selected after comparing it with a circular configuration (Fig. 1.1). Under the same conditions, the ellipsoidal chamber ensured a more uniform fluid distribution and faster filling. This allows all areas containing the plasmonic sensor to be exposed to chemical species for the same amount of time, ensuring homogeneous functionalization of the nanostructures and more accurate analyte detection.

The side channels were configured for reagent introduction, while the central channel was designated for rinsing and removing excess material. This arrangement optimizes the flow within the microfluidic chamber, minimizing distribution inconsistencies and improving process efficiency.

The dynamics of the injection and rinsing phases were defined by a time function that modulates the flow in the inlet channels (Fig. 1.1b). This function combines four appropriately phased rectangular pulses, representing the activation commands of the micropumps responsible for injecting fluids into the device. Specifically, the first pulse corresponds to the injection of the first chemical species, the second rectangular pulse to the initial rinsing phase, the third to the injection of the second chemical species, and the fourth to the final rinsing.

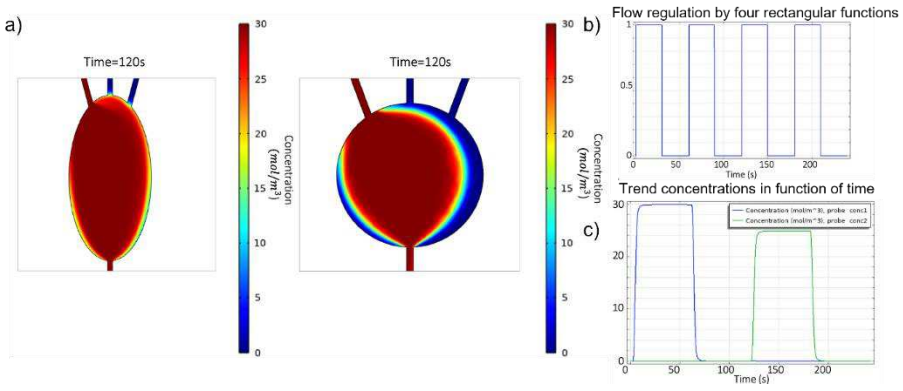

Figure 1.1 a) Comparison between the filling of an ellipsoidal and a circular microfluidic chamber; b) Filling and rinsing dynamics of the system, imposing a function formed by 4 rectangular pulses; and c) Results from a concentration probe in the microfluidic chamber, showing the achievement of the desired concentration uniformity within 30 seconds from the start of flow injection and rinsing.

To evaluate the uniformity of reagent distribution within the microfluidic chamber, a virtual concentration probe was placed at the center of the chamber during the simulations.

The simulations revealed that the system could reach an average reagent concentration of 95% of the desired concentration in the chamber within 30 seconds of the start of injection (Fig. 1.1c). The configuration with three inlet channels and one outlet channel allowed for uniform flow, minimizing the

formation of dead zones and ensuring that every point on the plasmonic surface is exposed to the same reagent concentration for the same period.

The optimal length and width of the channels were determined to be 1 cm and 400 μm, respectively, while the major and minor radii of the ellipsoidal chamber were defined as 5 mm and 2.5 mm. Additionally, the geometric parameters for the channels included a spacing of 200 μm between channels and a wall thickness of 50 μm.

The chemical species were simulated with an initial concentration of 30 mol/m^3 for chemical species 1 and 25 mol/m^3 for chemical species 2 to monitor concentration levels during filling and rinsing phases. In Figure 1.2 (a-d), the behavior of the system at times t=0, t=5s, and t=30s is shown, illustrating how

the species enter the system and how, after only 30 seconds, complete filling and effective rinsing are achieved.

A rapid and uniform filling is as crucial as an efficient rinsing, as it ensures effective cleaning and minimizes interference between functionalization steps, allowing for system reuse. The flow rates and time modulation function enabled precise flow control, preventing the saturation of active sites and maintaining laminar flow, thereby minimizing the risk of turbulence.

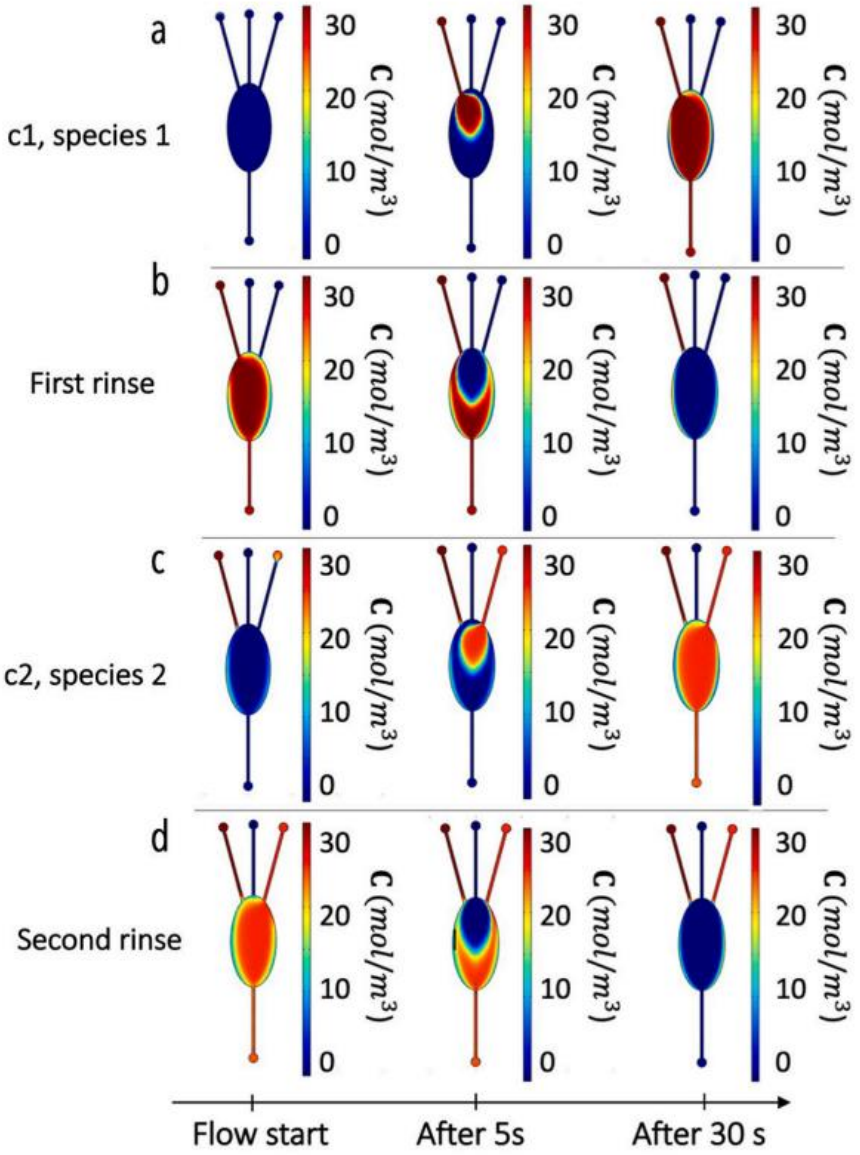

Figure 1.2. a-d) Chemical species and rinse flow within the system at the t=0, t = 5 s and t = 30 s.

Simulations were conducted to measure shear stress within the microfluidic chamber and channels, using a flow rate range from 10 μL/min to 100 μL/min. Shear stress is a measure of the tangential force exerted on the channel walls by the moving fluid. This parameter is crucial in microfluidics, as it directly affects the integrity of structures and the behavior of confined fluids, especially when working with sensitive materials or functional substrates.

Measuring shear stress is essential for several reasons. First, it helps to understand the level of stress applied to the channel walls, preventing potential deformations or long-term structural damage. Second, this data provides an essential reference point for evaluating the stress that will be applied to the plasmonic substrate, which will be inserted into the device. This plasmonic substrate, as an active component in fluid interaction and sensing, may be affected by high stress levels, impacting its efficiency and lifespan.

Flow rate	**Shear stress**
10 μL/min	0.053 Pa
20 μL/min	0.093 Pa
40 μL/min	0.17 Pa
60 μL/min	0.28 Pa
80 μL/min	0.37 Pa
100 μL/min	0.46 Pa

Table I

The simulations, conducted using strategically placed probes within the system, provided a detailed shear stress profile along the channel. In the Figure 1.3, I show both the contour lines indicating points of maximum shear stress within the microfluidic chamber and the surface plot measurements illustrating how stress is distributed within the channel. All average shear stress values within the device are summarized in Table I. These measurements allow us to better

calibrate the operational parameters of the device, ensuring optimal performance without compromising internal components, while maintaining adequate sensitivity for plasmonic and biomolecular sensing applications.

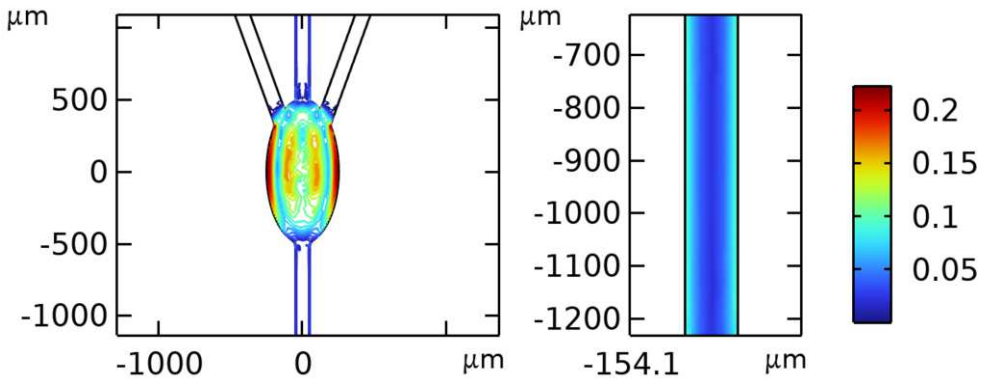

Figure 1.3 Contour lines and surface plot showing shear stress distribution within the microfluidic chamber and channel, with a flow rate of 10 µL/min. The contour lines indicate areas of maximum shear stress, while the surface plot illustrates how stress is distributed across the channel.

1.4 Fabrication

The device was fabricated in the clean room of the Institute of Applied Sciences and Intelligent Systems (ISASI-CNR) in Naples. The technology used for the fabrication of microchannels and microfluidic chambers is based on soft lithography and replica molding techniques, widely adopted methodologies for creating micro- and nanostructures on polymeric materials like PDMS. These techniques allow for the production of devices with complex geometries and high resolution, ensuring high reproducibility and the ability to easily customize the design of the microchannels [23-26].

The fabrication process (Fig. 1.4 a-c) begins with the creation of a raised master using photolithography techniques on a rigid substrate, usually silicon or glass. I obtained the master by depositing a layer of SU8-3010 negative photoresist, which was then exposed to UV radiation through a mask containing the desired microchannel design. The height of the SU8-3010 photoresist corresponds to the height of the microfluidic channel, which in this case was set to 15 µm.

After exposure to UV radiation, the exposed portion of the photoresist hardens, and through chemical development, the remaining raised structure forms a negative mold of the microfluidic structure on the surface of substrate.

Once the master is ready, I proceeded to prepare the PDMS, a biocompatible and transparent polymer ideal for microfluidic applications. The PDMS was mixed with a curing agent and poured over the master, followed by a degassing process to eliminate any air bubbles. The PDMS was then cured on a hotplate at 100°C for 1 hour, acquiring the shape of the mold. Once solidified, the PDMS was carefully peeled off the master, creating an accurate replica of the microchannel geometry.

Integrating the plasmonic substrate into the microfluidic chip is a crucial step in the fabrication process. The substrate, composed of an array of gold nanoparticles on a rigid silicon or glass support, is carefully placed into the PDMS microfluidic chamber. To ensure precise alignment and avoid misalignment that could compromise both the uniformity of functionalization and the sensitivity of the sensor, the chamber was designed with a custom-made cavity that matches the dimensions of the optical substrate, ensuring perfect compatibility with the silicon-based sensor.

After positioning the substrate, the bonding process between the PDMS and the plasmonic substrate is carried out. This step involves a surface activation treatment using oxygen plasma in Reactive Ion Etching (RIE). The plasma treatment generates hydroxyl groups (-OH) on the surfaces of the PDMS and the substrate, making them hydrophilic and facilitating the formation of covalent bonds between the surfaces. After plasma treatment, the PDMS chip is aligned and pressed against the plasmonic substrate, creating a stable and permanent bond between the two components, ensuring the robustness and reliability of the final microfluidic device.

This methodology allows the production of advanced microfluidic devices with complex geometries and a high degree of integration with sensitive substrates

such as plasmonic ones, providing an ideal platform for high-precision biochemical and diagnostic applications.

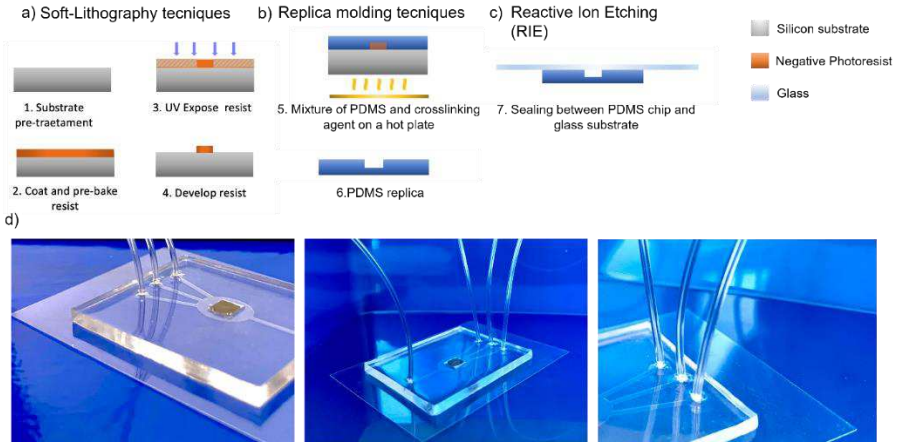

Figure 1.4. a-b-c) Fabrication process based on soft lithography, replica molding, and sealing using RIE (Reactive Ion Etching); and d) Images of the fabricated device.

1.5 Device Performance Evaluation as a Function of Flow Rate

Flow analyses were conducted using a red food-grade dye to verify the uniformity of filling, emptying, and coverage of the entire plasmonic sensor at the flow rates defined during the design phase, which were determined to be optimal for the system configuration. Additional flow rates were also explored for further testing. The device was filled using an external pumping system, connected via a syringe and tubing to the microchip, as shown in Figure 1.5 a-b.

The device was tested at various flow rates to assess the stability of the plasmonic substrate with respect to the shear stress generated. The goal was to determine whether the flow caused deterioration of the substrate, particularly the detachment of gold nanoparticles. For this purpose, images were acquired with an optical microscope (100X magnification, NA = 0.8) every minute for 30 minutes of continuous flow. The analysis showed that, at a flow rate of Q=1 ml/min, corresponding to a shear stress of 11.20 Pa in the microchannel geometry, significant nanoparticle detachment occurred. This deterioration was

observed by comparing images of the substrate before and after 30 minutes of flow, highlighting the damaged areas (circled) in Figure 5c.

Subsequently, robustness tests were conducted at flow rates lower than 1 ml/min, specifically between 10 µl/min and 100 µl/min. The images of the plasmonic substrate, taken after 30 minutes of flow, did not show significant damage to the nanoclusters. This flow range, which does not cause substrate deterioration, was selected to optimize the biochemical functionalization of the nanoclusters. Once the uniformity of filling and emptying was confirmed, functionalization was carried out.

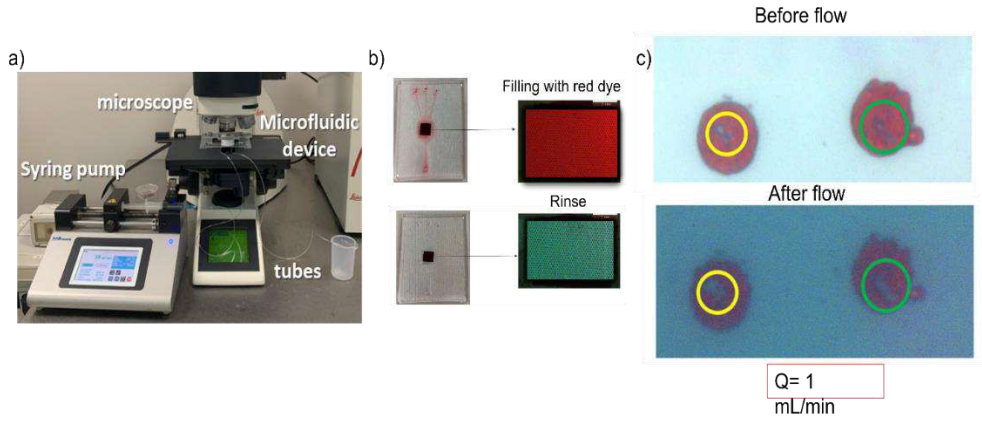

Figure 1.5. a) External pumping system in the microfluidic device; b) Verification of uniform filling, emptying, and coverage of the plasmonic nanostructures; and c) Deterioration of the gold nanoparticle substrate at a flow rate of 1 ml/min with a shear stress of 11.20 Pa.

1.6 Functionalization

The plasmonic substrate functionalization strategy (Fig. 1.6) was developed to create a highly specific surface capable of selectively capturing target biomarkers. In this study, a cysteine-folic acid (C-FA) chemical complex was used to interact with anti-folic acid (A-FA), an antibody specific for recognizing folic acid receptors (FR), which are overexpressed in many cancer cells.

Cysteine was chosen for its thiol group (-SH), which forms strong covalent bonds with metallic surfaces, such as gold nanoparticles (AuNPs). This stable bond ensures long-lasting anchoring of the molecule to the substrate, creating

a robust platform for subsequent functionalization with folic acid. Cysteine acts as a linker between the substrate and the specific ligand, stabilizing the entire structure and ensuring that folic acid is correctly oriented for A-FA antibody recognition. The functionalization was performed using an L-cysteine solution (3.6 mg/ml), which was flowed through the microfluidic device channels and onto the substrate surface for 30 minutes at a flow rate of 10 μl/min in the first experiment and 100 μl/min in the second. The thiol groups of cysteine spontaneously adsorb onto the AuNPs, forming a stable covalent bond.

Folic acid (FA) was chosen as a specific ligand for recognizing FR receptors. An FA solution (0.025 M) was injected into the microfluidic chip and incubated for 8-9 hours to allow interaction with the amino groups (-NH_2) of the immobilized cysteine. The carboxyl groups (-COOH) of folic acid were activated with EDC (0.05 M) and NHS (0.05 M) in dimethyl sulfoxide (DMSO), facilitating the conjugation reaction with the -NH_2 group of cysteine while leaving the pteroyl portion of folic acid free to interact with FR receptors.

After incubation, the substrate was exposed to an anti-folic acid (A-FA) solution. A-FA specifically interacts with the folic acid bound to the plasmonic surface, causing a change in the optical properties of the sensor. The flow was controlled with a syringe pump connected to the microfluidic device to ensure uniform distribution of the solutions and facilitate the conjugation reactions, leading to the formation of a highly selective plasmonic substrate.

Thanks to this functionalization strategy, the plasmonic substrate with C-FA complexes can selectively interact with A-FA, causing a detectable change in the optical properties through plasmonic resonance or spectroscopic measurements. This change allows for the specific identification of cancer cells,

providing a sensitive and targeted diagnostic platform for analyzing complex biological samples, such as those from liquid biopsies.

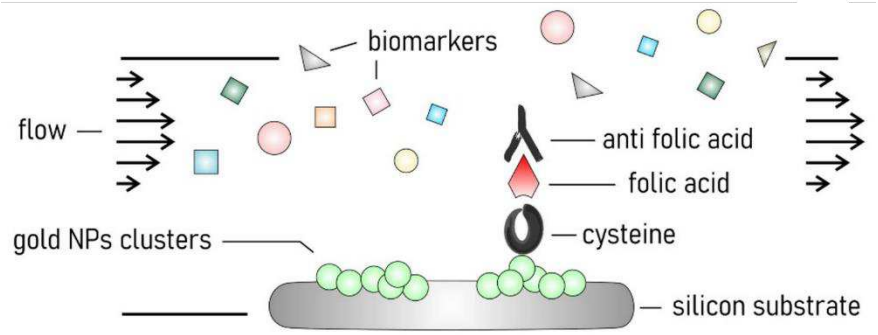

Figure 1.6. Functionalization Process

1.7 Optical Characterization

SEM Measurements

The nanopatterned substrate developed in this study consists of arrays of gold nanoparticle clusters. Each cluster is contained within a circular region with a diameter of 10 micrometers, with a distance of 20 micrometers from the structure edges. Within each region, the gold nanoparticles are randomly distributed, forming compact clusters. Scanning Electron Microscopy (SEM) measurements were performed to verify the nanoparticle distribution and analyze the chemical composition of the plasmonic substrate (Fig. 1.7). SEM images reveal an accurate distribution of gold and silicon in the expected positions, confirming the effectiveness of the electroless deposition process.

Post-analysis of high-resolution SEM micrographs, at magnification factors between 60,000 and 100,000, determined the average particle size to be s = 69 ± 24 nm.

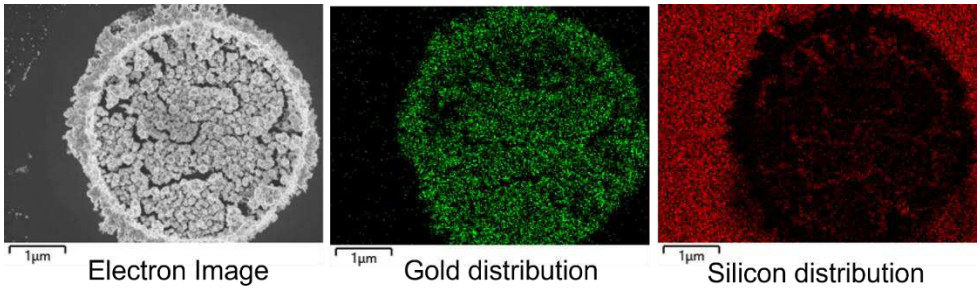

Figure 1.7. SEM Characterization

AFM Measurements

For a more detailed analysis of the surface characteristics, Atomic Force Microscopy (AFM) was used. AFM images of the gold nanoparticles were initially acquired over a large area of 13 micrometers × 13 micrometers and, for a more specific measurement of roughness, over a smaller area of 3 micrometers × 3 micrometers. The surface topography was represented both as a two-dimensional contour map and as a three-dimensional image. Data reveal that gold nanoparticles form dense aggregates, with a solid fraction of approximately sv = 1, an average height of z = 32 ± 8 nm, and an average roughness Ra = 17 ± 3 nm. The solid fraction represents the percentage of area occupied by the nanoparticles relative to the total area considered. Additionally, surface profile heights close to half the particle diameter suggest a spherical shape, consistent with an isotropic synthesis process [27].

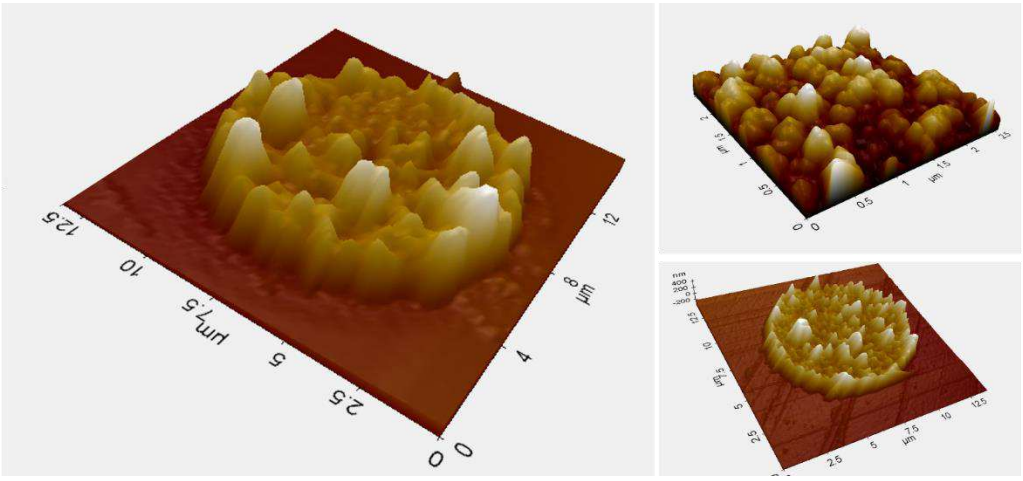

Figure 1.8. AFM Characterization

1.8 Fluorescence Analysis

Fluorescent images of the substrate were acquired to verify the conjugation between cysteine and folic acid. After the initial functionalization with cysteine, the gold nanoparticle substrate was incubated for 1 hour in an aqueous solution of Tetramethylrhodamine (TRICT) at room temperature and in the dark. TRITC reacts with the amine group of cysteine, making the functionalization visible under a fluorescence microscope. The substrate was then analyzed using confocal microscopy with an excitation wavelength of λex = 558 nm, which conferred a red fluorescence (λem = 575 nm) to the functionalized gold islands. The fluorescence of folic acid was detected using its autofluorescence, with emission at λex = 540 nm.

The effectiveness of the device in selectively binding folic acid was evaluated through fluorescence microscopy. The images obtained (Fig. 1.9a) show intense red fluorescence of FA, visible under irradiation with λex = 540 nm, localized on the gold nanoparticle clusters, indicating effective immobilization and colocalization of the receptors. The images were then processed to calculate the fluorescence intensity distribution. In Figure 1.9b, the analysis of the average intensity, normalized to the area occupied by the gold nanoparticles, revealed that lower flow rates (10 μl/min) are more effective than higher flow rates (100 μl/min) in achieving optimal surface functionalization.

These results indicate that at lower flow rates, the substrate has a longer interaction time with the folic acid solution, improving immobilization efficiency and ensuring a uniform distribution of the receptor. Therefore, flow

rates of 10 μl/min are preferable for obtaining a uniform and stable functionalization of the plasmonic substrate compared to higher rates.

1.9 Raman Analysis

The system based on gold nanoparticles functionalized with cysteine and folic acid (Au-CYS-FA) was developed to selectively capture anti-folic acid (A-FA) molecules present in the microfluidic channel and interact with the sensor. The effectiveness of the functionalization and the specific binding between A-FA and the Au-CYS-FA complex were evaluated using Raman spectroscopy, exploiting the SERS effect generated by the aggregation of the gold nanoparticles.

To verify the binding between A-FA and the substrate, a solution of anti-folic acid at a concentration of 3 mg/mL was distributed over the sensor surface. Raman measurements acquired on functionalized and non-functionalized areas (Fig. 1.9c) showed distinctive peaks for cysteine and folic acid, confirming successful conjugation.

The interaction with A-FA caused further variations in the Raman peaks, altering the intensity of the folic acid signals due to the increased structural complexity of the system. The Raman map (Fig. 1.9c) shows the signal distribution over an 8 μm × 8 μm area sampled at 9 points along the x and y axes. Each point represents the area under the Raman spectrum curve, providing a quantitative measure of the presence of molecules on the surface.

The results highlight a uniform signal distribution over the nanoparticle clusters, with maximum intensity at the cluster center, where the SERS effect is amplified, reaching 3.75×10^5 a.u. In non-functionalized areas (Fig. 1.9 d), the anti-folic acid distribution is irregular, with significantly lower values

(maximum of 2.5 × 10^4 a.u.), indicating a lack of selective binding with the nanoparticles.

The average Raman spectrum of A-FA, measured on the functionalized (f) and non-functionalized (nf) sensor in Figure 1.9e, indicates that the binding and recognition of the target molecule on the functionalized device are effective, unlike the n-f sensor, where the most relevant features of the A-FA Raman spectrum are lost, and much of the original molecular information is destroyed.

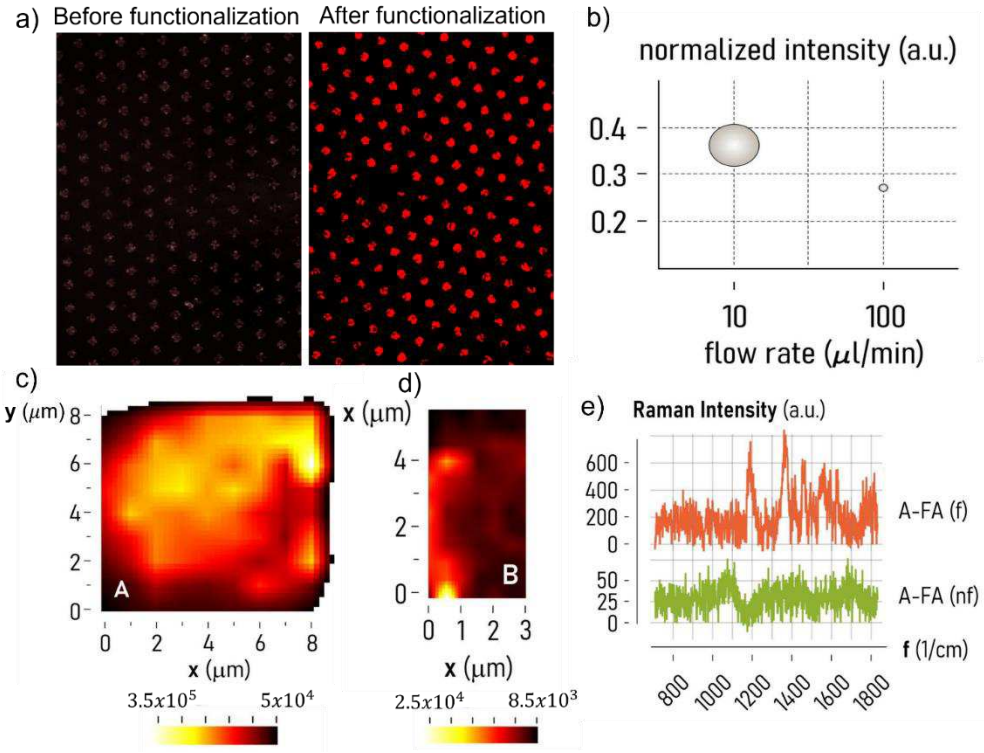

Figure 1.9. a) Image of the non-functionalized sensor and fluorescence images of the functionalized sensor; b) Mean value of fluorescent intensity of folic acid captured by the sensor under different flow conditions (10 and 100 µl/min). The mean was calculated over more than 20 technical replicates, with the marker diameters in the plot proportional to the standard deviation of the measurements; c-d) Raman map of A-FA activity measured on the functionalized plasmonic substrate (c) and on the non-functionalized plasmonic substrate (d); and e) Comparison between the average Raman spectra of A-FA measured on the functionalized and non-functionalized plasmonic substrate.

1.10 Conclusions

The device functionalized with the Au-CYS-FA complex has demonstrated the ability to selectively and reproducibly bind anti-folic acid, providing a reliable platform for the detection of specific biomarkers.
The results show a high degree of functionalization uniformity on the plasmonic substrate, thanks to the integration with the developed microfluidic system, which ensures uniform flow and eliminates stagnant zones. The optimization of the microfluidic chamber geometry and operational parameters contributed to improving the process quality, ensuring homogeneous and reproducible coverage. While the sensor exhibited excellent specificity and sensitivity in detecting target molecules, even in the presence of potential interferences, and the ability to detect very low concentrations of biomarkers, these aspects are further demonstrated and discussed in the next chapter, where selectivity and sensitivity are analyzed in greater detail.
These results provide a solid foundation for further developments in the field of high-precision diagnostic sensors. The next goal is to transfer the technology onto a fully flexible substrate, developing a plasmonic platform adaptable to deformable surfaces. This step, described in the next chapter, is critical for the realization of wearable sensors and portable devices designed to operate in dynamic environments, where flexibility and adaptability are essential requirements for advanced biomedical applications and in situ diagnostics.

References

1. Granata, F., Coluccio, M. L., Minopoli, A., Cuzzola, P., Costa, R., Malara, N., ... & Gentile, F. (2022). Optimization of microfluidic functionalization of a plasmonic-based device for selective capture of anti-folic acid in solution. Biosensors and Bioelectronics: X, 12, 100226.

2. Homola, J., Yee, S. S., & Gauglitz, G. (1999). Surface plasmon resonance sensors. Sensors and Actuators B: Chemical, 54(1-2), 3-15.

3. Chen, Y., & Ming, H. (2012). Review of surface plasmon resonance and localized surface plasmon resonance sensor. Photonic Sensors, 2, 37-49.

4. Löfås, S., Malmqvist, M., Rönnberg, I., Stenberg, E., Liedberg, B., & Lundström, I. (1991). Bioanalysis with surface plasmon resonance. Sensors and Actuators B: Chemical, 5(1-4), 79-84.

5. Hou, W., & Cronin, S. B. (2013). A review of surface plasmon resonance-enhanced photocatalysis. Advanced Functional Materials, 23(13), 1612-1619.

6. Berger, C. E., Beumer, T. A., Kooyman, R. P., & Greve, J. (1998). Surface plasmon resonance multisensing. Analytical Chemistry, 70(4), 703-706.

7. Van Der Merwe, P. A. (2001). Surface plasmon resonance. In Protein-ligand interactions: hydrodynamics and calorimetry (Vol. 1, pp. 137-170).

8. Bauch, M., Toma, K., Toma, M., Zhang, Q., & Dostalek, J. (2014). Plasmonic sensors for biosensing applications. Plasmonics, 9, 781-799.

9. Brolo, A. G. (2012). Plasmonics for sensing and spectroscopy. Nature Photonics, 6, 709-714.

10. Kneipp, K., Kneipp, H., Abdali, S., Berg, R., & Bohr, H. (2004). Surface-enhanced Raman scattering (SERS) for biosensing applications. Spectroscopy, 18, 433-440.

11. Kneipp, J., Kneipp, H., & Kneipp, K. (2008). Surface-enhanced Raman scattering in biomedical diagnostics. Chemical Society Reviews, 37, 1052-1060.

12. Kneipp, K., Wang, Y., Kneipp, H., Perelman, L. T., Itzkan, I., Dasari, R. R., & Feld, M. S. (1997). Single molecule detection using surface-enhanced Raman scattering (SERS). Physical Review Letters, 78, 1667-1670.

13. Deng, W., Xie, F., Baltarac, H. T. M. C. M., & Goldys, E. M. (2013). Metal-enhanced fluorescence in the life sciences: here, now and beyond. Phys. Chem. Chem. Phys., 15, 15695-15708.

14. Monat, C., Domachuk, P., & Eggleton, B. (2007). Photonic crystal structures for on-chip sensing applications. Nat. Photonics, 1, 106-114.

15. Jahn, I., Zukovskaja, O., Zheng, X.-S., Weber, K., Bocklitz, T., Cialla-May, D., & Popp, J. (2017). Surface-enhanced Raman scattering for biosensing applications. Analyst, 142, 1022-1047.

16. Wang, C., & Yu, C. (2015). Applications of nanotechnology in biosensors and diagnostics. Nanotechnology, 26.

17. Chen, H., Das, A., Bi, L., Choi, N., Moon, J. I., Wu, Y., Park, S., & Choo, J. (2020). Plasmonic nanostructures for surface-enhanced Raman spectroscopy. Nanoscale, 12(42), 21560-21570.

18. Li, B., Zhang, W., Chen, L., & Lin, B. (2013). Microfluidic electrophoresis: Recent advances and applications. Electrophoresis, 34(15), 2162-2168.

19. Gao, R., Ko, J., Cha, K., Ho Jeon, J., Rhie, G.-E., Choi, J., de Mello, A. J., & Choo, J. (2015). Microfluidic biosensors based on surface-enhanced Raman scattering. Biosens. Bioelectron., 72, 230-236.

20. Krafft, B., Panneerselvam, R., Geissler, D., & Belder, D. (2020). Microchip electrophoresis integrated with surface-enhanced Raman scattering for chemical sensing. Anal. Bioanal. Chem., 412(2), 267-277.

21. Oh, Y. J., & Jeong, K.-H. (2014). Fabrication of nanostructured substrates for surface-enhanced Raman scattering. Lab Chip, 14, 865-868.

22. Pryor, R. W. (2000). Multiphysics modeling using COMSOL: A first principles approach. Jones and Bartlett Publishers.

23. Xia, Y., & Whitesides, G. M. (1998). Soft lithography. Annu. Rev. Mater. Sci., 28, 153-184.

24. Duffy, D., McDonald, J., Schueller, O., & Whitesides, G. (1998). Rapid prototyping of microfluidic systems in poly(dimethylsiloxane). Anal. Chem., 70, 4974-4983.

25. Whitesides, G. M., Ostuni, E., Takayama, S., Jiang, X. Y., & Ingber, D. E. (2001). Soft lithography in biology and biochemistry. Annu. Rev. Biomed. Eng., 3, 335-373. 26. Sia, S. K., & Whitesides, G. M. (2003). Microfluidic devices

fabricated in poly(dimethylsiloxane) for biological studies. Electrophoresis, 24, 3563-3576.

27. Coluccio, M. L., Gentile, F., Francardi, M., Perozziello, G., Malara, N., Candeloro, P., & Di Fabrizio, E. (2014). Electroless deposition and nanolithography can control the formation of materials at the nano-scale for plasmonic applications. Sensors, 14(4), 6056-6083.

2
Flexible Plasmonic Device for Biomedical Applications

In the context of developing microsystems on flexible materials for biomedical applications, I focused on creating a sensor similar to the one previously described, but entirely developed on soft material. This involved the study and fabrication of plasmonic structures on flexible materials, particularly PDMS. In this chapter, I present the development of a fully flexible plasmonic device, fabricated by creating clusters of gold nanoparticles (AuNPs) on thin, flexible PDMS membranes (Fig. 2). The project aims to produce a flexible device functionalized with human immunoglobulin G (IgG), which has demonstrated the ability to recognize, capture, and amplify anti-human IgG at concentrations of 25 µg/ml, ensuring high reproducibility and reliability. Furthermore, the device was tested as a biosensor through Raman spectroscopy analysis of interleukin 8 (IL8), achieving a detection limit below 1 ng/ml. These results highlight the potential of the plasmonic flexible platform for highly sensitive biomolecular detection, reinforcing its applicability in real-world biomedical scenarios [1].

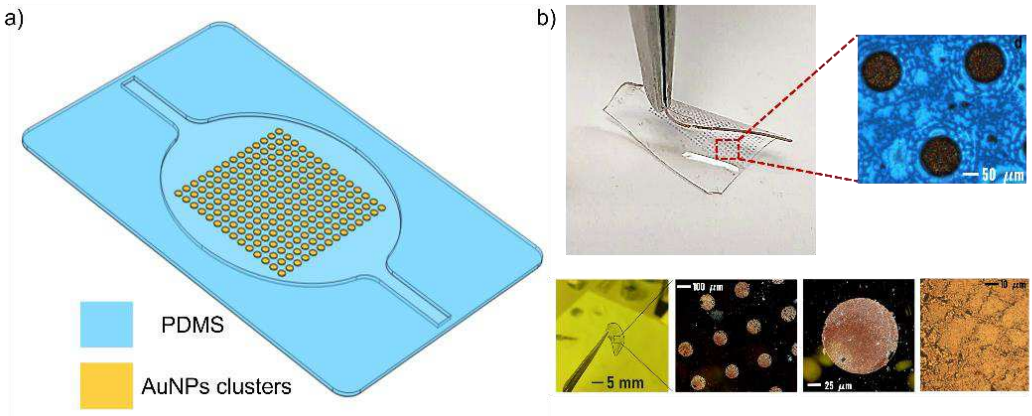

Figure 2. a) Schematic of a plasmonic sensor on flexible material integrated with microfluidics, along with fabrication images; and b) Optical microscope images are shown to illustrate the morphology of the sensor.

2.1 Soft Material for Plasmonic Biosensing

The development of plasmonic devices on rigid substrates has led to remarkable advancements in sensitivity and resolution for optical and spectroscopic measurements [2-4]. However, these devices face structural limitations that reduce their applicability in dynamic environments and portable solutions. The rigidity of the substrate prevents the sensor from adapting to curved or deformable surfaces, making it unsuitable for wearable devices or use in complex environments where flexibility is crucial.

To overcome these limitations, recent research has focused on integrating gold nanoparticles (AuNPs) onto flexible and cost-effective substrates such as polymers, elastomers, and nanofibers, paving the way for more versatile, flexible, and scalable plasmonic devices [4-11]. Among the most promising flexible materials, PDMS has emerged as an ideal substrate due to its unique properties, including optical transparency, biocompatibility, and the ability to conform to non-planar surfaces.

Various techniques for creating flexible nanoplasmonic substrates have been categorized in the scientific literature. One approach involves physical blending and curing, where metal nanoparticles are uniformly dispersed within a polymer precursor using physicochemical techniques. The material is then solidified, creating a stable structure with nanoparticles evenly distributed within the polymer [12–14]. Although this method allows for relatively simple fabrication, the control over the spatial distribution of the nanoparticles is limited.

Another common technique is the template method, where an external template is used to transfer a pattern onto a soft polymer matrix, such as PDMS, through imprinting, evaporation, or sputtering processes. The macroscopic pattern replicates the shape of the template, while the metal nanostructures formed exhibit internal features determined by the evaporation or sputtering parameters. Examples of this approach include three-dimensional cauliflower-like gold nanoparticle films on PDMS and wavy arrays of silver nanoparticles on flexible substrates [15, 16]. While this technique offers greater control over surface geometries, it is constrained by the limitations of the template transfer process.

An alternative approach is embedded co-growth, which enables plasmonic nanostructures to form directly within the polymer matrix during the

fabrication process. This method significantly improves adhesion between the metal material and the polymer substrate, enhancing the mechanical and optical stability of the device. Additionally, it reduces physical and optical mismatches between the metal and polymer phases, resulting in more robust and durable devices [17, 18].

Examples of PDMS functionalization with metal nanoparticles include multi-step growth of gold nanoparticles forming three-dimensional conglomerates on the PDMS surface, or inkjet printing to create silver nanoparticle patterns on polymer substrates. However, these methods tend to produce random dispersions of nanoparticles or are limited by the geometry of the template and deposition parameters [19, 20].

In contrast, my work combines advanced techniques, including optical lithography and site-selective electroless deposition, to achieve precise functionalization of PDMS membranes with clusters of gold nanoparticles. Lithography allows for highly accurate definition of the substrate areas where nanoparticles are positioned, while electroless deposition enables nanometric and highly controlled growth of the nanoparticles, improving localization and device efficiency. Compared to traditional methods, this approach offers superior control over the distribution and size of the nanostructures, enhancing the performance of the device in plasmonic and biosensing applications [20-22].

The device represents a significant advancement over traditional plasmonic sensors, offering a versatile platform for detecting low-concentration biomarkers and real-time monitoring of biological parameters. It opens the door to the creation of wearable health monitoring devices. A fabrication and functionalization protocol for the flexible substrate has been developed, allowing for selective capture of target biomolecules and amplification of optical signals thanks to the properties of gold nanoparticles.

2.1 Fabrication

The fabrication of the flexible plasmonic device is divided into three main phases: the preparation of PDMS membranes, the deposition of gold nanoparticles, and the integration of the flexible plasmonic substrate into the final device (Fig.2.1).

The flexible substrate was created by depositing PDMS onto a silicon wafer using a spin coating process. The preparation was optimized to achieve uniform membranes, ensuring mechanical stability and excellent optical properties. PDMS was prepared by mixing the polymer base with the curing agent in a 10:1 ratio, then homogenized and degassed to remove any air bubbles. It was then spin-coated onto the silicon wafer at 1000 rpm for 60 seconds and cured at 100°C for 30 minutes, resulting in a final thickness of approximately 300 μm. This uniformity is essential for ensuring a homogeneous distribution of the gold nanoparticles and preventing optical inconsistencies in the device.

The PDMS surface was then treated with lithographic techniques to create geometric patterns. A layer of positive resist (OIR 9060) was applied by spin coating, achieving a thickness of approximately 1.3 μm, with 100 μm diameter holes arranged in a 1 cm × 1 cm square matrix. Then, a 160 nm layer of amorphous silicon was deposited across the PDMS membrane via PECVD (Plasma-Enhanced Chemical Vapor Deposition). Using the lift-off technique in acetone, amorphous silicon islands were created on the PDMS.

The geometric pattern consisted of a square array of islands divided into three size types: islands of 100 μm, 150 μm, and 200 μm, along with a small square with a side of 250 μm. On each membrane, I successfully created at least 6 distinct patterns, as seen in Figure 2.2.

Finally, gold nanoparticles were deposited on the flexible substrate through an electroless deposition process, which allows for the reduction of gold ions into metallic gold on the autocatalytic silicon surface, producing nanoparticles with controlled size and uniform distribution across the PDMS surface, thus enhancing the optical and functional properties of the device.

The deposition solution was composed of hydrofluoric acid (HF) and gold chloride (AuCl3) at a concentration of 5 mM, maintained at 50°C for 40 minutes. The nanoparticles formed on the amorphous silicon surface through electrochemical reduction, creating clusters with an average diameter of about

50 nm and random distribution. This process ensures uniform surface coverage of the PDMS without the formation of unwanted aggregates that could compromise the quality of the optical signal.

In Figure 2.3, the fabricated flexible plasmonic device is shown.

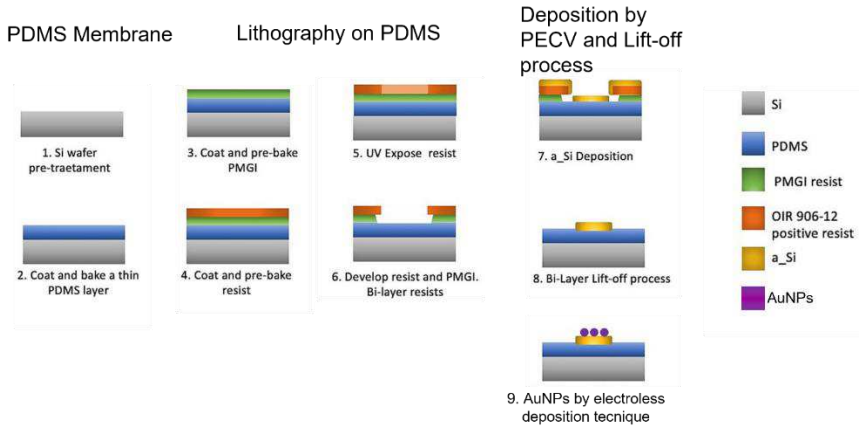

Figure 2.1 Fabrication Process**.**

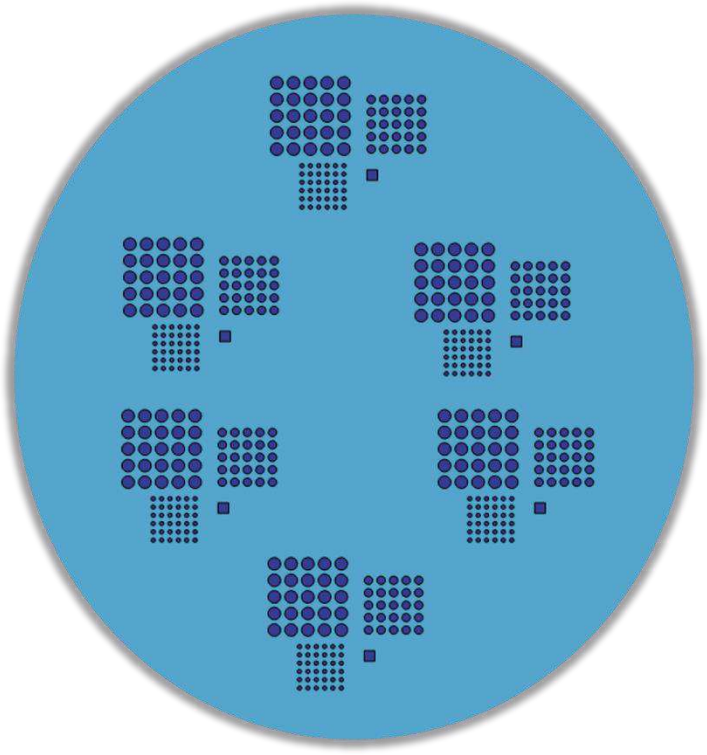

Figure 2.2. Geometrical pattern by optical lithography.

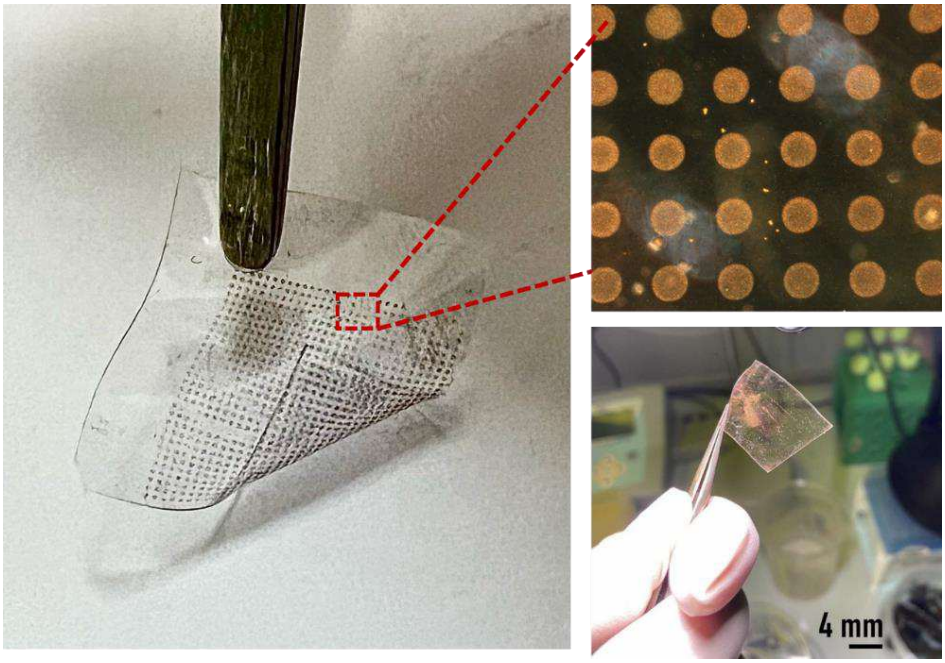

Figure 2.3. The fabricated flexible plasmonic device.

2.3 Characterization

2.3.1 Mechanical Properties of Flexible Plasmonic Devices

Once the gold nanoparticles were deposited, the PDMS was separated from the silicon wafer and characterized in terms of its mechanical and functional properties for use as a biosensor.

Tests were conducted to evaluate the chemical and mechanical properties of the device. The wettability of the PDMS surface was analyzed using an automatic contact angle meter, which measures the angle formed between the sample surface and a droplet of deionized water. This contact angle reflects the hydrophobicity of the surface or hydrophilicity: an angle greater than 90° indicates a hydrophobic surface, while an angle below 90° indicates a hydrophilic one. The tests showed that the device is moderately hydrophilic, with a contact angle of about 81°, suggesting a reasonable interaction with water.

The mechanical characterization was performed through tensile tests and deformation analysis using digital image correlation (DIC). This method

allowed for the mapping of the stress-strain curve, which describes the relationship between the applied stress and the resulting deformation of the material. The curve provides information about the mechanical strength of the material and its ability to deform under load. The results indicated that the PDMS device has a stiffness of approximately 2.8 MPa, which is higher than the typical Young's modulus of human tissues and organs (E ~10-1000 kPa), but lower than conventional engineering materials such as metals or ceramics, making it suitable for biomedical applications that require flexibility (Fig. 2.4).

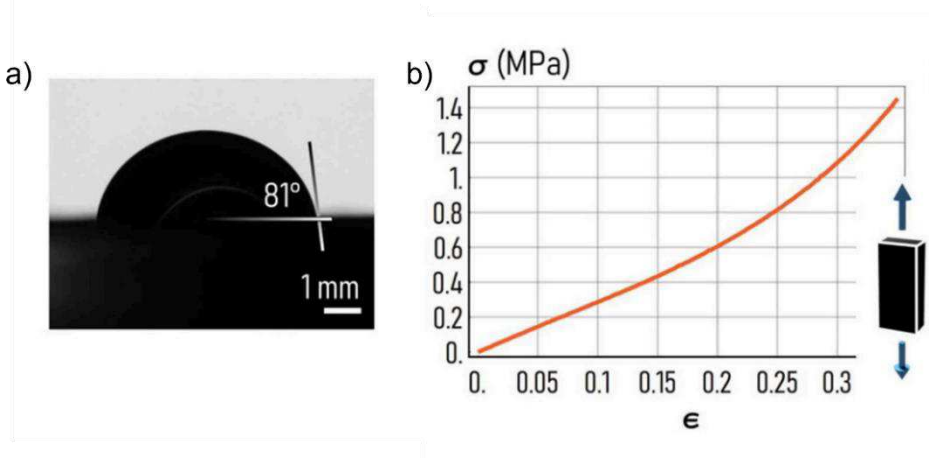

Figure 2.4. a) Contact angle of a microliter drop of DI water with the PDMS plasmonic surface; and b) Stress strain curve of the PDMS device.

2.3.2 Optical Characterization

SEM Measurements

Characterization measurements were performed using SEM on plasmonic samples fabricated on PDMS substrates. As previously described, the samples consist of amorphous silicon islands (with dimensions of 250, 200, and 100 μm) deposited on PDMS membranes. Gold was grown on these islands through the electroless deposition process, resulting in clusters of gold nanoparticles.

SEM images clearly show the presence of gold nanoparticle clusters randomly distributed within the silicon islands. The deposition appears less uniform compared to that observed on rigid substrates, likely due to the intrinsic roughness of the PDMS, which typically exhibits a surface roughness (RMS) of

8–10 nm. In comparison, rigid silicon substrates often have a much lower roughness, typically below 1 nm. This significant difference in surface roughness likely influences the distribution and uniformity of the gold nanoparticle clusters, as rougher surfaces tend to promote a more random and less homogeneous deposition. Including this observation provides additional insight into the relationship between substrate morphology and the resulting nanostructure uniformity.

Nevertheless, the characteristic granular structure is clearly identifiable, confirming the correct formation of gold nanoparticle clusters. The analysis of the micrographs, conducted at magnifications ranging from 20,000 to 50,000, revealed precise details of the morphology of the clusters (Fig. 2.5).

The nanoparticle clusters exhibit a compact arrangement, with particles displaying irregular shapes and variable sizes, consistent with an uncontrolled nucleation and growth process. This behavior is typical of the electroless deposition technique and contributes to the creation of an active plasmonic surface, characterized by an optimal granular texture for advanced applications.

Furthermore, SEM measurements highlighted good adhesion between the nanoparticles and the amorphous silicon substrate, along with the stability of the structure on the flexible PDMS membrane. These results confirm the effectiveness of the fabrication process and the suitability of the samples for advanced plasmonic applications, such as biosensing and optical detection.

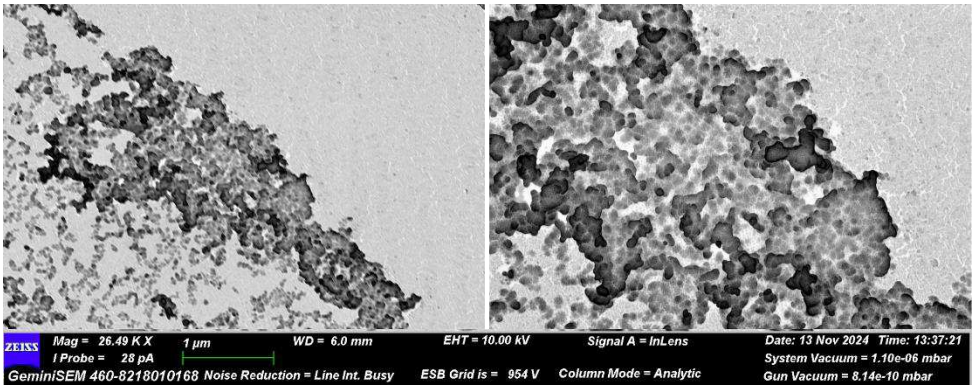

Figure 2.5. SEM images of plasmonic sensor on PDMS substrates.

Atomic force microscopy (AFM) was used to examine the geometric characteristics of the device at the nanoscale. Figure 2.5 shows an AFM image of the sample surface over an area of 8 µm × 8 µm. Post-processing of the AFM data allowed us to determine the average roughness (RA) and root mean square (Rrms) of the plasmonic gold substrate, with values of approximately RA ~15 nm and Rrms ~20 nm.

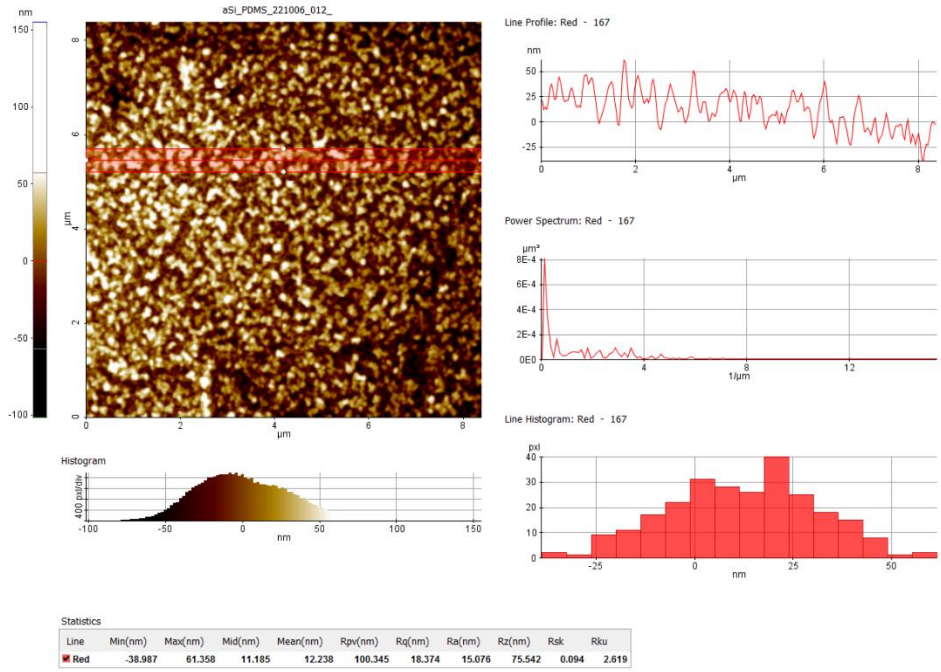

Figure 2.6. AFM image of the gold nanoparticle cluster surface (8µm × 8µm)

A area of 6 µm × 6 µm was also scanned (Fig. 2.7) to observe the profile of the islands where the nanoclusters are positioned, allowing us to trace the overall cluster profile. The complete cluster shows a height of approximately 260 nm, consistent with the expected thicknesses based on the applied protocols.

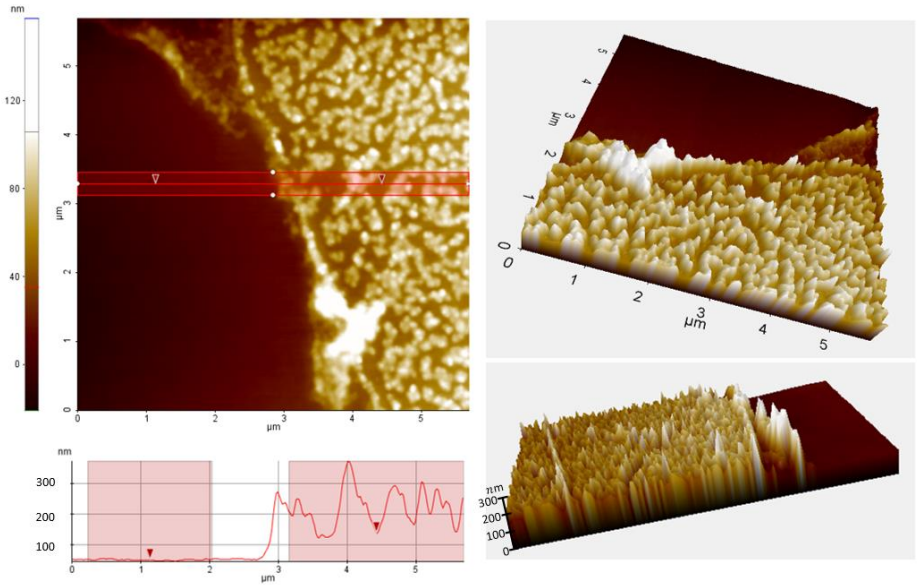

Figure 2.7. AFM measurement of the profile of islands containing gold nanoparticle clusters over a 6 µm × 6 µm area.

2.4 Functionalization

The functionalization process of the plasmonic PDMS substrates was carried out using human IgG antibodies as recognition molecules, followed by incubation with anti-human IgG antibodies labeled with FITC (fluorescein isothiocyanate) to demonstrate specific antigen-antibody binding and verify the amplification effect of the device (Fig. 2.8 a). The functionalization process involved the following steps:

- Preliminary cleaning: The plasmonic PDMS devices were initially washed with 200 µl of deionized MilliQ water to remove any surface impurities and then dried with a nitrogen jet.
- Functionalization with IgG antibodies: 20 µl of a solution containing human IgG antibodies at a concentration of 25 µg/µl was deposited on each sample. The samples were incubated for 20 minutes, allowing the antibodies to bind to the PDMS surface. After incubation, excess antibodies were removed, and the samples were washed once with 200 µl of PBS and twice with 200 µl of deionized MilliQ water.

- Binding with labeled anti-IgG antibodies: To form the antigen-antibody complex, 20 µl of a solution containing anti-human IgG antibodies labeled with FITC at the same concentration (25 µg/µl) was added. The solution was left to adsorb on the surface for another 20 minutes.
- Final washes: After incubation, the samples were washed twice with 200 µl of PBS and three times with 200 µl of deionized MilliQ water to remove unbound molecules and ensure a clean surface for subsequent analysis.

This functionalization protocol ensures the effective immobilization of human IgG antibodies on the surface of the device and the formation of the antigen-antibody complex with labeled anti-IgG antibodies, demonstrating the specificity and capability of the device to selectively capture target molecules.

2.5 Fluorescence Analysis

To demonstrate the analytical capabilities of the device, human immunoglobulin G (h-IgG) was adsorbed onto the surface of the gold nanoparticle clusters. After functionalizing the device with IgG, it was exposed to a solution containing fluorescently labeled anti-human IgG (FITC), the target molecule, to verify the ability of the device to recognize and capture the specific biomarker.

The success of antigen-antibody immobilization was confirmed via fluorescence microscopy. The obtained images (Fig. 2.7 b, c) show high signal intensity and good colocalization of fluorescence with the plasmonic active sites of the device, indicating selective capture and identification of the biomarker in solution.

The specific and selective functionalization of the plasmonic nanostructures with h-IgG was achieved due to the physical and chemical properties of the gold nanoparticles (NPs) on the sensor surface. These gold NPs, characterized by high surface energy density, strongly interact with biomolecules and proteins, including immunoglobulins, with a binding constant of 10^{-9} M^{-1} s^{-1}.

To verify the specificity of h-IgG functionalization on the nanostructures, an experimental campaign was conducted on flat silicon substrates coated with gold nanoparticles, following the same functionalization protocol used for the devices described in the study. The samples were exposed to a solution containing anti-human IgG, and fluorescence images showed that the signal intensity was about 1 arbitrary unit on the nanoparticle clusters and around 0.04 arbitrary units on the flat silicon, indicating a fluorescence enhancement factor of about 20 times, consistent with theoretical predictions and finite element simulations of the electromagnetic field.

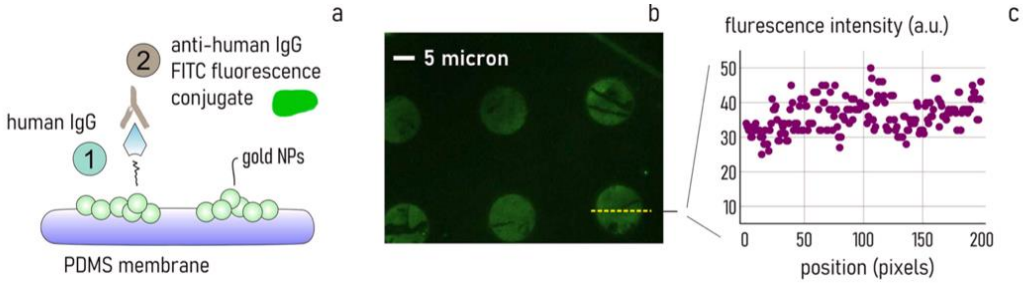

Figure 2.8. a) Scheme of the antigen-antibody immunoassay test performed by the sensor device; b) Upon functionalization with humang IgG, and exposure to anti-human IgG, the sensor device correctly captured anti-human IgG in solution, evidenced by bright green fluorescence of samples; and c) Fluorescence intensity profile measured across a cluster of gold-nanoparticles after incubation with anti-human IgG.

2.4 Comparative Evaluation of Fluorescent Sensitivity on Flexible and Rigid Substrates

One of the main questions was whether using a flexible substrate, such as PDMS, could reduce sensitivity compared to a rigid substrate like silicon. To address this, a series of studies were conducted to quantify the sensitivity variation of gold nanoparticles on both types of substrates. Test devices with clusters of gold nanoparticles were prepared on both PDMS and silicon substrates, using FITC-labeled fluorescent solutions (fluorescein isothiocyanate), a dye commonly used for fluorescence measurements. To determine the minimum detection limit for fluorescence, the solution

concentrations were progressively reduced, starting from 0.0015 mg/ml down to a minimum concentration of 0.000023425 mg/ml.

For each measurement, 10 μl of solution was diluted with 20 μl of water, halving the concentration. The resulting solution was applied to PDMS samples and allowed to be fully absorbed; in this case, the absorption time for the PDMS samples was significantly longer than for silicon, with a waiting period of approximately one hour.

Microscope images and light intensity measurements at different concentrations showed that the PDMS substrates displayed the same behavior observed in silicon: as the FITC-labeled solution was diluted, fluorescence intensity decreased, and the solution distribution became progressively less uniform, concentrating only in specific areas of the wells.

After collecting light intensity data for both substrates, graphs were created to represent the fluorescence variation as a function of concentration. A comparison between the silicon and PDMS curves revealed a similar exponential decreasing trend in both cases, despite the structural differences in the materials. Surprisingly, the analyses showed that PDMS exhibited slightly better performance than silicon, contrary to initial expectations. Further analyses will be conducted to explore and confirm this preliminary and promising result (Fig. 2.9).

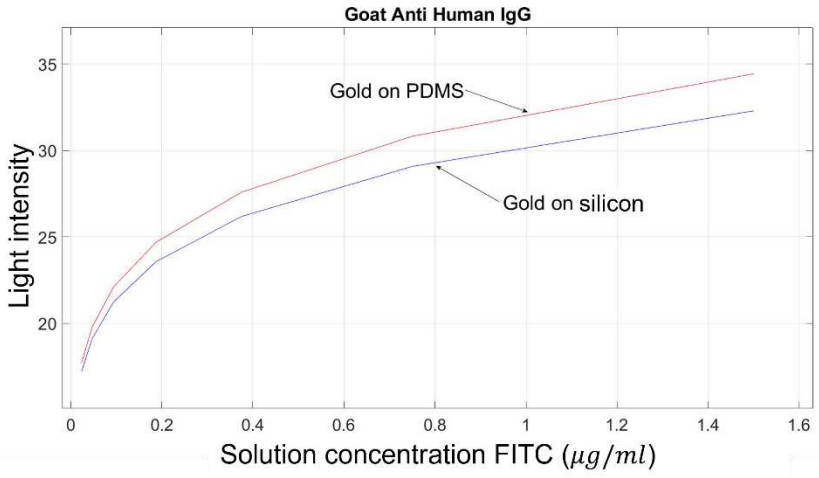

Figure 2.9. Comparison of fluorescence intensity on PDMS and silicon substrates with varying FITC solution concentrations. Results show a similar exponential decrease in fluorescence for both materials, with PDMS demonstrating slightly higher sensitivity than expected.

2.7 Verifying Site-Selective Amplification of Fluorescence Signal by Gold Nanoparticles

To verify whether the gold nanostructured surface effectively enhanced the sensitivity of the sensor, a series of experiments was conducted, comparing two types of plasmonic sensors: one with a gold nanostructured surface on PDMS and the other with a nominally flat gold surface on silicon. The goal was to evaluate which configuration provided greater fluorescence signal amplification.

Both surfaces were exposed to a fluorescent FITC solution at a concentration of 100 µg/ml for 10 minutes. After incubation, the surfaces were washed with deionized water and dried using a nitrogen flow. Fluorescence images were acquired using a fluorescence microscope. The images were then processed to measure fluorescence intensity in various areas of the device.

10The results, illustrated in the box-and-whisker plot in Figure 2.9, showed that the average fluorescence intensity on the gold nanostructured surface on PDMS was approximately three times higher than that measured on the flat gold surface on silicon. This demonstrates that the nanostructuring of the surface significantly enhances the amplification of the fluorescent signal compared to the smooth surface.

These experiments clearly show that the gold nanoparticle clusters generate plasmonic "hot spots" that amplify the local electromagnetic field, thereby increasing the fluorescence signal intensity. In contrast, the flat gold surface does not provide effective plasmonic amplification, which explains the weaker signal observed.

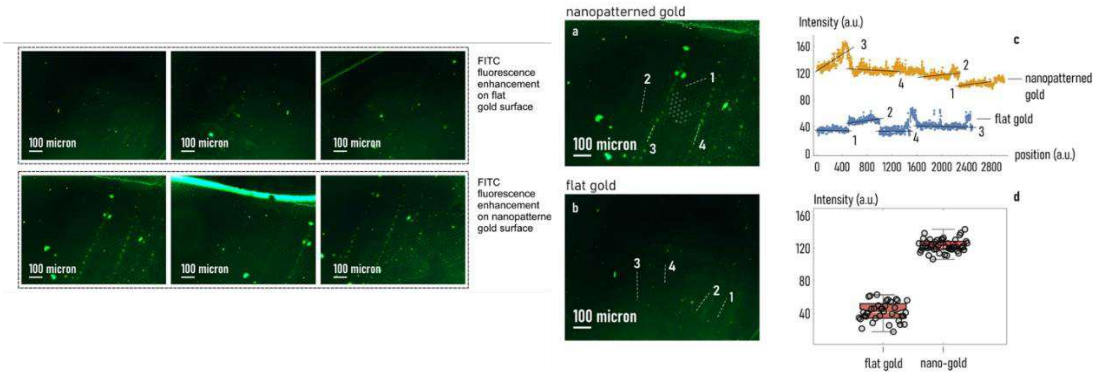

Figure 2.10. Comparison of fluorescence intensity between flat gold on silicon and clustered gold nanoparticles on PDMS. After exposure to FITC solution (100 μg/ml), the nano-patterned gold surface)showed approximately 3 times higher fluorescence intensity than the flat gold surface, demonstrating superior signal enhancement.

2.8 Verifying Selectivity and Specificity of the Sensor Device

To demonstrate the selectivity and specificity of the device, additional experiments were conducted in which the PDMS sensor was functionalized with human immunoglobulins G (h-IgG), the ligand molecule. The device was then exposed to complex artificial mixtures containing goat anti-human IgG (g-Ah-IgG), the target molecule, along with a green fluorescent FITC conjugate bound to g-Ah-IgG and various interferents that could potentially hinder the proper recognition and measurement of g-Ah-IgG.

Two different interferents were used:

1. Bovine Serum Albumin (BSA): A globular protein with a high molecular weight (~60 kDa) that could interfere with the binding between h-IgG and g-Ah-IgG due to steric hindrance.

2. Rabbit anti-goat IgG (r-Ag-IgG): An antagonist of anti-human IgG, which directly competes with g-Ah-IgG by binding to h-IgG and potentially replacing g-Ah-IgG either partially or entirely.

The fluorescence values are proportional to the efficiency of the (h-IgG)-(g-Ah-IgG) binding:

- In the case of simple mixtures without interferents, the fluorescence intensity of the (h-IgG)-(g-Ah-IgG) complex is approximately 79 arbitrary units (a.u.).
- The intensity decreases to about 65 a.u. in the presence of BSA and to approximately 39 a.u. in the presence of r-Ag-IgG, both of which interfere with the adhesion of g-Ah-IgG.
- By comparison, in the case of non-specific binding (incubation of fluorescent g-Ah-IgG on a non-functionalized device), the measured intensity is around 33 a.u.

Quantitative analysis of the data indicated that:

- The selectivity of the device is approximately 81% in the presence of BSA (weak antagonist).
- The selectivity drops to 49% in the presence of r-Ag-IgG (strong antagonist).

For comparison, in the case of non-specific binding (i.e., incubation of fluorescent g-Ah-IgG on a non-functionalized device), the selectivity was around 40%. These values were calculated relative to the human IgG-anti-human IgG complexation without interferents (Fig. 2.11).

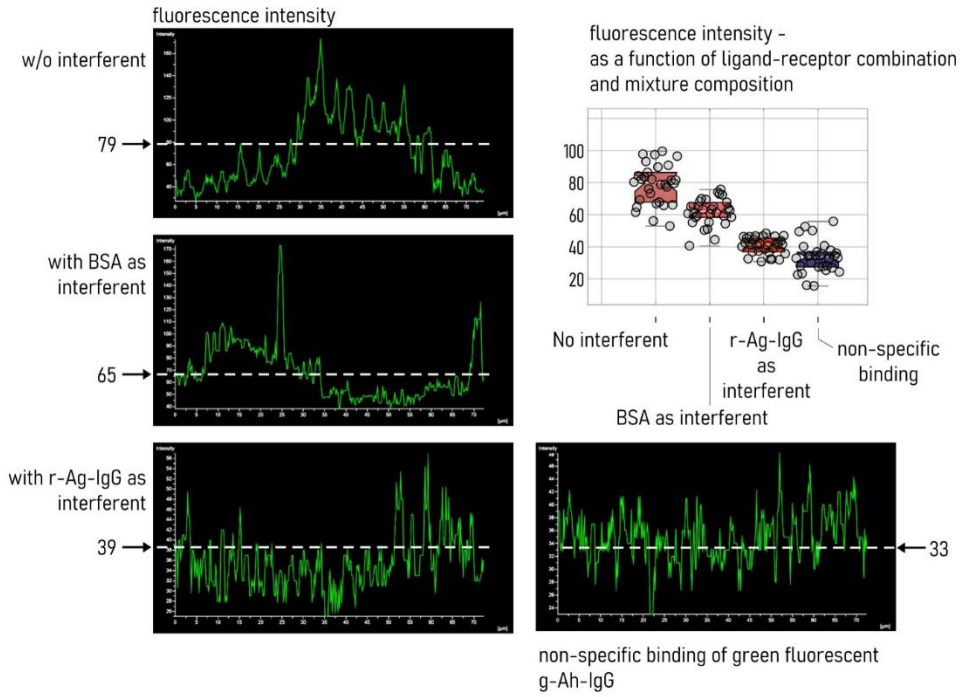

Figure 2.11. FITC green fluorescence intensity and the mean fluorescence intensity on different substrates as a function of the ligand-receptor combination and mixture composition.

2.9 Raman Analysis

Flexible plasmonic devices have been tested and evaluated as biosensors also through Raman measurements. In particular, interleukin 8 (IL8), a pro-inflammatory cytokine involved in numerous physiological and pathological processes, including immune response and the development of inflammatory

and cancerous diseases, was studied. The sensitive and selective detection of IL8 is therefore of great interest for advanced diagnostic applications. For this purpose, aqueous solutions of IL8 at different concentrations (1 ng/ml, 5 ng/ml, 10 ng/ml, and 100 ng/ml) were analyzed using Raman SERS spectroscopy, employing PDMS membranes functionalized with plasmonic nanostructures. Measurements were performed by depositing IL8 solutions onto PDMS membranes via drop casting. The analysis was conducted in two experimental configurations:

- Direct: in this mode, the laser radiation directly impacts IL8 adsorbed onto gold nanoparticles, maximizing the plasmonic interaction.
- Inverse: the laser is applied from below, first passing through the PDMS membrane before reaching IL8 on the gold nanoparticles, allowing an assessment of the substrate's influence on the Raman signal.

For comparison, an IL8 solution at a concentration of 1 mM/ml was deposited on a calcium fluoride (CaF_2) slide, whose Raman spectra were used as a reference. The Raman spectra collected for IL8 in both the direct and inverse configurations are shown in Figures 2.12a and 2.12b. Some key IL8 peaks, including those at 853, 950, 1339, 1450, and 1655 cm^{-1}, were identified and highlighted in the colored bands, as they are indicative of the presence of the biomolecule. Other Raman signals, however, overlapped with background contributions from the gold nanoparticles or PDMS and were excluded from the analysis. Although the two spectra exhibit a similar structure, a significant reduction in the intensity of IL8 characteristic peaks is observed in the inverse configuration compared to the direct one. This attenuation is mainly due to the absorption and scattering of laser radiation as it passes through the PDMS membrane, with signal loss being more pronounced at lower frequencies.
Figures 2.12c and 2.12d show the variation in Raman intensity of the 1450 cm^{-1} band as a function of IL8 concentration for both configurations. In both cases, the Raman signal increases with the biomolecule concentration. The best fit of the experimental data to a linear model yielded the following relationships:

- Direct configuration: $I = 570 + 10.4c$
- Inverse configuration: $I = 190 + 3.6c$

where I represents Raman intensity in arbitrary units and c is the IL8 concentration in ng/ml. The accuracy of the linear model is confirmed by the determination coefficient $r^2 = 0.83$ for the direct configuration and $r^2 = 0.87$ for the inverse one). The determination coefficient is a statistical parameter that indicates how well a mathematical model describes experimental data: a value of r^2 close to 1 suggests a high correlation between the measured data and the model's prediction. Moreover, the model parameters suggest that the device can detect IL8 even at concentrations below 1 ng/ml. Figure 2.12e presents a density map representing the attenuation factor, defined as the ratio of Raman intensity in the direct configuration to that in the inverse configuration, as a function of concentration and frequency. The data indicate that attenuation is highest (~16) at the highest measured concentration (100 ng/ml) and frequency (1655 cm^{-1}), while it is lowest (~0.6) at lower concentrations (5 ng/ml).

The attenuation factor, which describes the signal quality in both configurations, is influenced by concentration and reflects the balance between the quantity of deposited biomolecules, the interfering contribution from PDMS, and the SERS effect. For concentrations between 1 and 5 ng/ml, the attenuation value is close to 1, indicating a good trade-off between plasmonic amplification and reduced substrate interference. In this range, signal loss in the inverse configuration is minimized, making the device reliable even in this mode. Figures 2.12f and 2.12g show Raman maps acquired on clusters of gold nanoparticles, with spectra collected over an area of approximately 20 μm × 20 μm with a step size of 1 μm. The obtained signals are well-defined, confirming the effectiveness of the deposition for spectroscopic analysis. Finally, to further explore the Raman response as a function of concentration, principal component analysis (PCA) was performed on Raman maps obtained in the two experimental configurations (Figures 2.12h and 2.12i). This technique allowed

for data dimensionality reduction, summarizing spectra into a few principal components. In the resulting graphs, Raman data related to IL8, described by the first two principal components (PC1 and PC2), are distributed along a continuous trajectory, gradually shifting from the upper right to the lower left of the graph, corresponding to concentration variations from 1 ng/ml to 100 ng/ml. This clear separation among the different concentrations confirms the device's ability to effectively distinguish the presence of IL8 based on the deposited amount, demonstrating the sensor's potential for high-sensitivity biosensing applications.

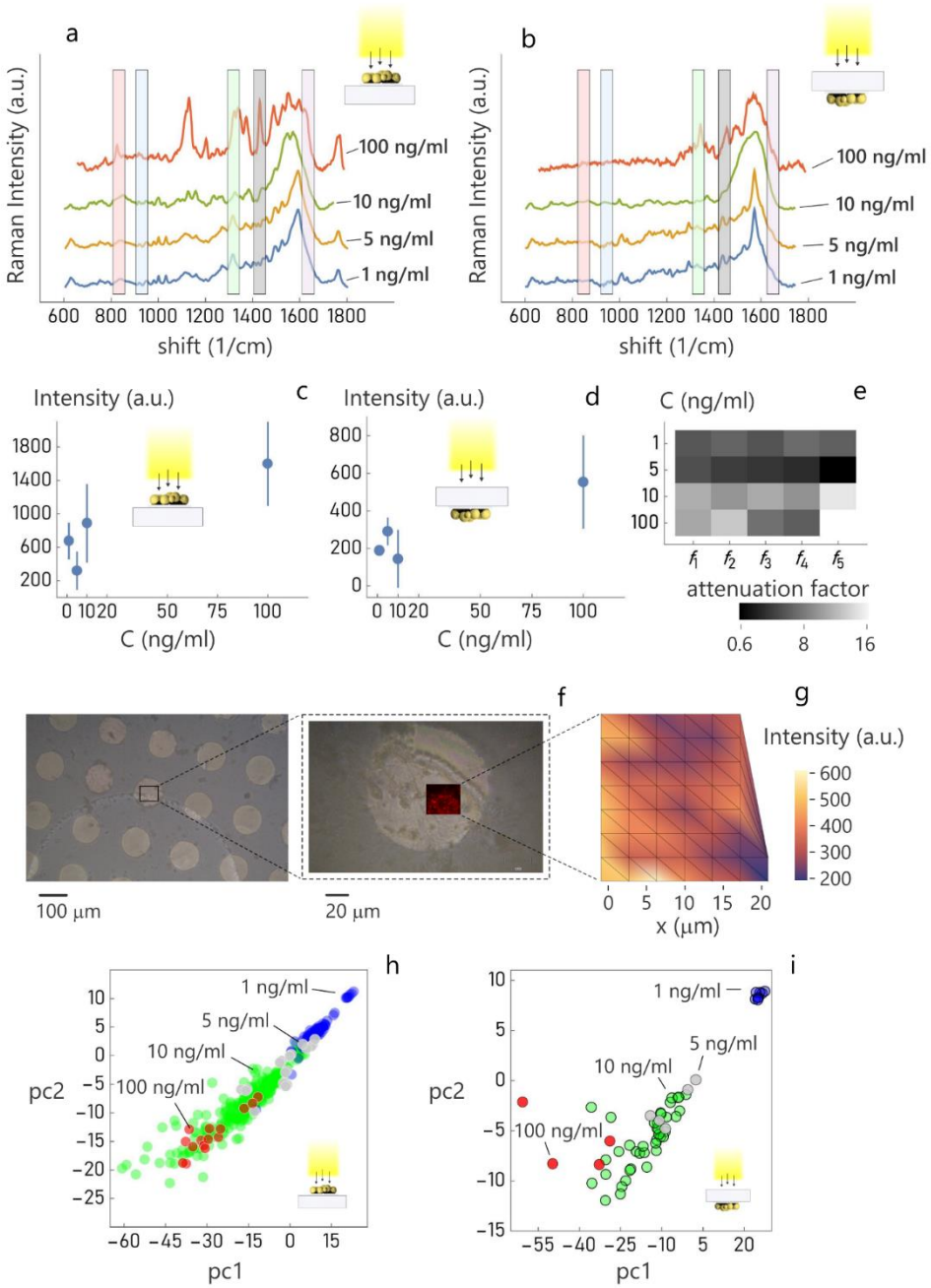

Figure 2.12. a)Raman spectra of IL-8 molecules acquired on soft plasmonic devices for different values of concentration of the starting solution, the system is interrogated from the top (*direct*, top-down configuration); b) Raman spectra of IL-8 molecules acquired on soft plasmonic devices for different values of concentration of the starting solution, the system is interrogated from the bottom (*inverted*, bottom-up configuration); c)Mean Raman intensity of IL-8 molecules for values of concentration varying from 1 ng/ml to 100 ng/ml measured adopting a *direct* configuration and using as a refence a band centered around 1450 cm^{-1} with a bandwidth of 4 cm^{-1};d) Mean Raman intensity of IL-8 molecules for values of concentration varying from 1 ng/ml to 100 ng/ml measured adopting an *inverted* configuration and using as a refence a band

centered around $1450\ cm^{-1}$ with a bandwidth of $4\ cm^{-1}$; e) In some cases, Raman analysis of samples was performed on an array of points partially overlapping the cluster of nanoparticles onto which the solute was adsorbed (f) so that resulting spectra can be displayed in the form of a density plot of values – i.e. a map (g). Raman maps measured for values of concentration of IL-8 ranging in the $1\ ng/ml - 100\ ng/ml$ were processed using principal components analysis (PCA); h) The diagram in reports the first (pc1) versus the second (pc2) principal component of Raman spectra in the considered range of a concentration, measured adopting a *direct* configuration. i) The diagram in reports the first (pc1) versus the second (pc2) principal component of Raman spectra in the considered range of a concentration, measured adopting an *inverted* configuration. In both cases, points in the PCA plot are clustered according to the concentration of the originating solution.

2.10 Conclusions

I have developed a method to integrate clusters of gold nanoparticles onto soft PDMS materials. The shape and size of these nanoparticles generate plasmonic effects, enhancing the spectroscopic and fluorescence signals of biomarkers anchored to the nanostructured surface. To validate the effectiveness of the device as a biosensor, two clinically relevant biomarkers were selected: immunoglobulin G (IgG), essential for monitoring immune response, and interleukin-8 (IL-8), used to detect inflammatory states and infections. The analysis of IgG was conducted through fluorescence microscopy, demonstrating the device's ability to detect and quantify the biomolecule with a linear signal over a wide concentration range. The obtained performance was comparable to or superior to that of rigid silicon substrates functionalized with gold nanoparticles, confirming the sensor's effectiveness in monitoring low-concentration biomolecules. Raman spectroscopy was used to evaluate the amplification of the spectroscopic signal of IL-8, examining two experimental configurations: a direct one, where the laser interacts directly with the plasmonic surface, and an inverse one, which simulates the sensor's behavior in a PDMS microfluidic channel, with the radiation passing through the membrane before reaching the biomarker. The tests revealed a clear dependence of the signal on concentration, with high sensitivity even in more complex experimental conditions and a very low detection limit. Unlike other

fabrication techniques for plasmonic devices on soft materials, the developed method allows optimal control over the shape and size of metal nanostructures on PDMS. This was achieved by combining different techniques, including optical lithography, PECVD silicon deposition, and electroless growth, enabling precise patterning on the substrate and nanometric localization of the nanoparticles. The described method, along with its future developments, has the potential to surpass existing techniques in terms of dimensional control and precision of plasmonic nanostructures, allowing for the fabrication of nanometric devices on surfaces ranging from millimeter to centimeter scales. Furthermore, due to the biocompatibility and biostability of PDMS, the developed device could potentially be implanted into tissues or organs for localized, site-selective biomolecule detection. The obtained results confirm that the device meets the diagnostic requirements for IgG detection and is highly sensitive to IL-8 detection, with potential for further optimizations in Raman measurements. Thanks to its versatility and high sensitivity, the device represents a promising solution for advanced biosensing applications. The next step is to make the device more compact by eliminating the need for an external pumping system. To achieve this, I focused on studying capillarity in microfluidic systems. During my research abroad, I deepened my understanding of capillarity principles to apply them to a specific context, which will be discussed in the next chapter.

References

1. Granata, F., Pirillo, N., Alabastri, A., Schirato, A., Bruno, L., Costa, R., ... & Gentile, F. (2023). Synthesis of plasmonic gold nanoparticles on soft materials for biomedical applications. Micro and Nano Engineering, 19, 100207.

2. Bauch, M., Toma, K., Toma, M., Zhang, Q., & Dostalek, J. (2014). Plasmon-enhanced fluorescence biosensors: a review. Plasmonics, 9, 781–799.

3. Brolo, A. G. (2012). Plasmonics for future biosensors. Nature Photonics, 6, 709–714.

4. Strobbia, P., Languirand, E., & Cullum, B. M. (2015). Recent advances in Plasmonic nanostructures for sensing: a review. Optical Engineering, 54, 100902.

5. Gontier, A., Marae-Djouda, J., Hmima, A., Proust, J., Bercu, N.-B., Le Joncour, L., Stagon, S., Konoplev, G., Tarasov, S.-A., Adam, P.-M., Gardan, J., Panicaud, B., Molinari, M., & Maurer, T. (2020). Flexible plasmonic and strain sensors: fabrication, design and perspectives. IOP Conference Series: Journal of Physics, 1461, 012096.

6. Kumari, S., Mohapatra, S., & Moirangthem, R. S. (2018). Development of flexible Plasmonic sensor based on imprinted nanostructure array on plastics. Materials Today: Proceedings, 5, 2216–2221.

7. Song, L., Chen, J., Xu, B. B., & Huang, Y. (2021). Flexible plasmonic biosensors for healthcare monitoring: progress and prospects. ACS Nano, 15, 18822–18847.

8. Torino, S., Conte, L., Iodice, M., Coppola, G., & Prien, R. D. (2017). PDMS membranes as sensing element in optical sensors for gas detection in water. Sensors and Bio-Sensing Research, 16, 74–78.

9. Peng, J., Jeong, H.-H., Smith, M., Chikkaraddy, R., Lin, Q., Liang, H.-L., De Volder, M.-F.-L., Vignolini, S., Kar-Narayan, S., & Baumberg, J. J. (2021). Fully-printed flexible plasmonic metafilms with directional color dynamics. Advanced Science, 8, 2002419.

10. Wang, Y., Zhao, C., Wang, J., Luo, X., Xie, L., Zhan, S., Kim, J., Wang, X., Liu, X., & Ying, Y. (2021). Wearable plasmonic-metasurface sensor for noninvasive and universal molecular fingerprint detection on biointerfaces. Science Advances, 7, eabe4553.

11. Jia, P., Kong, D., & Ebendorff-Heidepriem, H. (2020). Flexible plasmonic tapes with nanohole and nanoparticle arrays for refractometric and strain sensing. ACS Applied Nano Materials, 3, 8242–8824.

12. Chen, W. C., Shiao, J. H., Tsai, T. L., Jiang, D. H., Chen, L. C., Chang, C. H., Lin, B. H., Lin, J. H., & Kuo, C. C. (2020). Multiple scattering from electrospun nanofibers with embedded silver nanoparticles of tunable shape for random lasers and white-light-emitting diodes. ACS Applied Materials & Interfaces, 12, 2783–2792.

13. Dai, L., Lu, X., Song, L., Huang, Y., Liu, B., Zhang, L., Zhang, J., Wu, S., & Chen, T. (2018). Macroscopic-oriented gold nanorods in polyvinyl alcohol films for polarization-dependent multicolor displays. Advanced Materials Interfaces, 5, 1800026.

14. Yun, T. G., Park, M., Kim, D. H., Kim, D., Cheong, J. Y., Bae, J. G., Han, S. M., & Kim, I. D. (2019). All-transparent stretchable electrochromic supercapacitor wearable patch device. ACS Nano, 13, 3141–3150.

15. Li, J., Yan, H., Tan, X., Lu, Z., & Han, H. (2019). Cauliflower-inspired 3D SERS substrate for multiple mycotoxins detection. Analytical Chemistry, 91, 3885–3892.

16. Yang, K., Zong, S., Zhang, Y., Qian, Z., Liu, Y., Zhu, K., Li, L., Li, N., Wang, Z., & Cui, Y. (2020). Array-assisted SERS microfluidic chips for highly sensitive and multiplex gas sensing. ACS Applied Materials & Interfaces, 12, 1395–1403.

17. Liu, Z., Wang, H., Huang, P., Huang, J., Zhang, Y., Wang, Y., Yu, M., Chen, S., Qi, D., Wang, T., Jiang, Y., Chen, G., Hu, G., Li, W., Yu, J., Luo, Y., Loh, X. J., Liedberg, B., Li, G., & Chen, X. (2019). Highly stable and stretchable conductive films through thermal-radiation-assisted metal encapsulation. Advanced Materials, 31, e1901360.

18. Choi, S., Han, S. I., Jung, D., Hwang, H. J., Lim, C., Bae, S., Park, O. K., Tschabrunn, C. M., Lee, M., Bae, S. Y., Yu, J. W., Ryu, J. H., Lee, S. W., Park,

K., Kang, P. M., Lee, W. B., Nezafat, R., Hyeon, T., & Kim, D. H. (2018). Highly conductive, stretchable and biocompatible Ag-Au core-sheath nanowire composite for wearable and implantable bioelectronics. Nature Nanotechnology, 13, 1048–1056.

19. Scarano, S., Berlangieri, C., Carretti, E., Dei, L., & Minunni, M. (2017). Tunable growth of gold nanostructures at a PDMS surface to obtain plasmon rulers with enhanced optical features. Microchimica Acta, 184, 3093–3102.

20. Zhang, Q., Xu, J. J., Liu, Y., & Chen, H. Y. (2008). In-situ synthesis of poly(dimethylsiloxane)-gold nanoparticles composite films and its application in microfluidic systems. Lab on a Chip, 8, 352–357.

21. Coluccio, M. L., Das, G., Mecarini, F., Gentile, F., Pujia, A., Bava, L., Tallerico, R., Candeloro, P., Liberale, C., De Angelis, F., & Di Fabrizio, E. (2009). Silver-based surface enhanced Raman scattering (SERS) substrate fabrication using nanolithography and site selective electroless deposition. Microelectronic Engineering, 86, 1085–108.

3
Wettability Study for Optimizing Sample Spreading on Cryo-EM Grids

During my period at the Vrije Universiteit Brussel (VUB), I conducted an extensive study of capillarity phenomena, focusing specifically on how varying surface wettability properties affect the complex dynamics of droplet spreading upon impact. In Belgium, I applied this knowledge to critical applications in cryo-electron microscopy (cryo-EM), where precise control of sample distribution is essential. The research group I was part of specialized in cryogenic imaging and measurements through cutting-edge approaches, and my contribution involved an in-depth analysis and the development of numerical models to predict the spreading behavior of sample droplets impacting cryo-EM grids. This modeling work was supported by advanced simulations using COMSOL Multiphysics and required detailed parameterization of variables like droplet size, impact velocity, and surface properties. The importance of this spreading dynamic is paramount in cryo-EM. By optimizing sample spreading on the grid, my work enabled the creation of thinner sample layers, which are essential for achieving high-quality measurements. Thinner layers provide optimal electron transparency and superior image quality, both of which are critical for high-resolution imaging in cryo-electron microscopy. This research also led to the design of new, optimized grid prototypes incorporating pillars and channels to enhance droplet spreading. These innovations represent a significant step forward in cryo-EM grid design, improving sample distribution and enabling more reliable and accurate measurements in cryogenic applications.

Figure 3. Droplet spreading dynamics.

3.1 Introduction to Cryo-EM

Single-particle cryo-electron microscopy (cryo-EM) has established itself as a reliable method for obtaining detailed high-resolution structures of biological molecules [1]. However, sample preparation represents one of the main obstacles in cryo-EM, sparking a growing interest in researching new approaches for grid preparation. In conventional practice, a few milliliters of solution are applied to a cryo-EM grid for analysis. The grid is then subjected to a drying process, leaving a thin layer of liquid on the surface, typically between 100 and 200 nm thick, using blotting paper. This layer is then vitrified, usually by plunging it into liquid ethane, to be subsequently examined under an electron microscope [2-4]. Despite the evident success of this technique in producing high-resolution structures, the widespread adoption and growing popularity of cryo-EM have revealed significant limitations in this methodology.

Most of the sample is dispersed during drying, with 99.9% being removed by the blotting paper. The interactions with the paper are not fully understood and can lead to sample contamination. In fact, during the drying phase, the sample can undergo denaturation, compromising the accuracy in determining high-resolution structures. Moreover, this relatively prolonged time interval prevents the observation of reaction intermediates on a millisecond time scale [5].

Current research focuses on new approaches to overcome these limitations and improve sample preparation in cryo-electron microscopy [7-14]. These approaches involve blot-free methods for applying the sample to cryo-EM grids. In most of them, the protein solution is deposited onto the grid in picoliter droplets.

In this context, it is crucial, for the development of highly reproducible methods, to thoroughly understand how these small droplets spread when they reach the grid surface.

In a previous work by this group [15], a system was designed that combines a low-consumption rapid mixer with a drop-on-demand (DOD) spray generator. It was demonstrated that cryo-EM grids could be prepared with a temporal resolution of 5 ms, using about 100 nL of protein solution per EM grid. The developed system enabled the analysis and visualization of transient conformational states with high precision. However, controlling the spreading

of the jet-generated droplets on the grid remains a significant challenge for obtaining high-quality cryo-EM images. The first obstacle to overcome is achieving an optimal sample thickness on the grid, essential for cryo-EM studies. It is evident that many physical parameters, such as droplet size, surface contact angle, and sample properties, influence the final outcome. Therefore, the success of a good cryo-EM measurement depends on the surface properties of the grid and, consequently, on the behavior of the sample droplet upon contact.

Currently, various studies are exploring this innovative direction. For example, the NIH National Resource for Automated Molecular Microscopy has developed an advanced approach to reduce sample inefficiency and freezing delays [16-17]. The Spotiton device uses technology similar to inkjet printers to apply small droplets onto an EM grid. A recent innovation from this group has been the creation of self-wicking EM grids, achieved by treating EM grids with an ammonium persulfate solution, promoting the growth of Cu(OH)2 nanowires [17-19]. These nanowires, acting as a sort of miniature "blotting paper," quickly remove excess liquid, improving the quality of sample films for analysis. However, engineering certain aspects of the described approaches can be challenging for non-specialized laboratories [16-17].

There is, however, no work demonstrating a precise and detailed analysis of the spreading of a sample droplet on the cryo grid surface to monitor the time required to achieve a suitable sample thickness for cryogenic measurements before the grid itself is frozen.

For this study, I investigated the spreading dynamics of a sample droplet on a cryo-EM grid. The droplet impacting the grid is generated through optical cavitation using a laser within a microfluidic circuit (Fig. 3.1a). Specifically, I analyzed a single cryo grid-cell, i.e., on a single well of the overall grid (Fig. 3.1a). To determine which configuration allows the most optimal spreading, I conducted a numerical simulation using three different types of cryo grid-cells (*simple* cryo grid-cell*, pillars* cryo grid-cell*, channels* cryo grid-cell) as shown in

Figure 3.1(b-d). I considered parameters such as contact angle and other geometric factors.

The analysis was performed using the commercial software COMSOL Multiphysics, specifically utilizing its *Microfluidics* module. This allowed us to precisely trace the interface between the liquid sample and the impact surface of the cryo grid-cell. The droplet impact analysis was conducted to highlight the droplet shape and the velocity field trend during spreading on a solid substrate with characteristics similar to the grids used in cryo-EM. The results of the numerical analysis were compared with experimental data, achieving a satisfactory match regarding droplet spreading parameters.

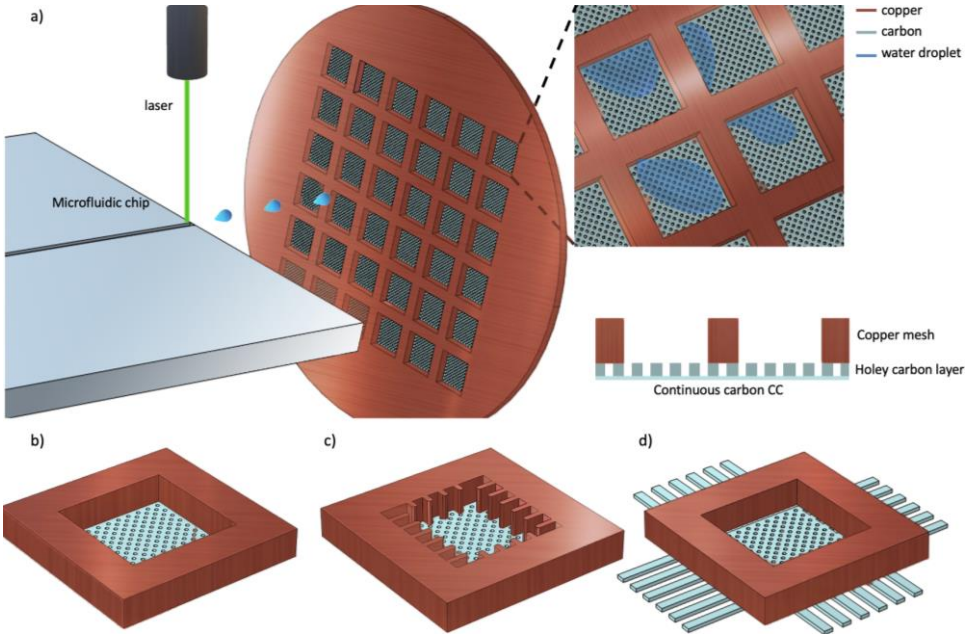

Figure 3.1. a) Sketch of the droplet spreading process: a laser targets the end of a microfluidic channel, generating a microjet through optical cavitation. The droplets are propelled and spread onto the grid. Tested configurations include: b) simple cryo grid-cell, c) pillars cryo grid-cell, and d) channels cryo grid-cell. Numerical simulations aim to optimize sample droplet spreading while keeping wettability, size, and distance from the substrate constant.

3.2 Materials and Methods

3.2.1 Contact angle measurements

Contact angle measurements were conducted on the surfaces of the cryo grid-cells to estimate the achievable wettability, aiming to obtain realistic parameters for simulations. The apparatus used for the contact angle measurement (Fig. 2a) consisted of a camera and a support on which the grid was fixed using double-sided adhesive tape. Measurements were performed both before and after plasma treatment of the grids. Two types of grids were evaluated: one where the droplet spreading layer was carbon and another where the spreading layer was gold.

Specifically, the two grids were subjected to two different oxygen plasma treatments. The first treatment was performed with an RF power of 25 W, an airflow of 50 sccm, and a duration of 1 minute. The second treatment used an RF power of 100 W, with the same airflow of 50 sccm and a duration of 1 minute.

To measure the contact angle, a 0.5 μL water droplet was deposited on the cryogenic grids using a pipette. The contact angles for the different surfaces before plasma treatment were: 19° for carbon, 82° for gold and 120° for copper.

After plasma treatment at 25 W power, the contact angles changed as follows: 7° for carbon, 31° for gold and 68° for copper. With plasma treatment at 100 W, the contact angles further improved, resulting in: 5° for carbon, 17° for gold and 48 for copper.

These results show that plasma treatment is effective in improving the wettability of the cryogenic grid surfaces, with a more pronounced improvement at 100 W power. Optimizing the surface wettability is critical for cryo-EM sample preparation, as it directly influences droplet spreading and, consequently, the quality of the obtained images. These optimized parameters were then used in the simulations to ensure they accurately reflected the behavior of the droplets in reality.

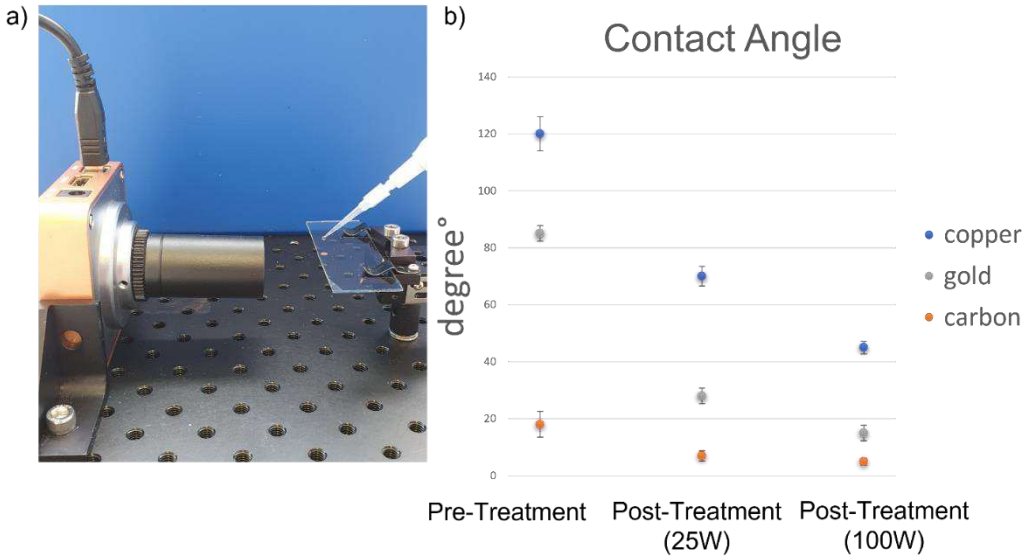

Figure 3.2 a) Experimental setup used for contact angle measurements on various surfaces (copper-carbon-gold); and b) Graph depicting the contact angle results as a function of surface type and associated treatment.

3.2.2 FEM Model Design

The study of the dynamic behavior of a water droplet impacting a solid substrate was conducted using the conservative Level Set method in COMSOL Multiphysics. The Level Set method in COMSOL Multiphysics is chosen for studying the dynamic behavior of a water droplet impacting a solid surface due to its accuracy in representing the interface and its ability to handle complex deformations of the droplet post-impact. Additionally, the method is known for its robustness and numerical stability, reducing the risk of calculation errors common in other interface tracking techniques. The theory governing this method is detailed in the Appendix A.

I started this study by designing a 2D axisymmetric model to understand how a droplet spreads on an unconfined substrate with open boundaries (Fig. 3.3 a-b). Our primary objective was to analyze the nanometric interface between the aqueous and gaseous (air) phases during the descent of the droplet and

subsequently observe the droplet deformation on a substrate with specific wettability properties.

Specifically, I considered several key parameters influencing the droplet spreading process. I examined the initial droplet diameters (5 μm, 10 μm, 20 μm), the contact angle between the droplet and the substrate (1°, 5°, 10°), and the initial droplet velocity (5 m/s). The choice of these parameters was motivated by the complexity of the spreading phenomenon, which requires precise modeling of the interactions between the liquid and gaseous phases.

The preliminary approach with 2D simulations allowed us to optimize these parameters and refine the model, preparing us for more detailed 3D simulations. I chose to focus on simulating a larger droplet among those examined in 2D, as these droplets are commonly generated experimentally through optical cavitation on a cryo grid-cell. The simulated droplet had an initial velocity of 5 m/s and a contact angle of 5 ° with the substrate (the lowest angle measured experimentally on the grid).

This methodological choice allowed us to compare and validate the results obtained from the simulations, ensuring a deeper understanding of the mechanisms underlying the droplet spreading process on complex surfaces. Our primary objective was to measure, as the parameters varied, the area of the droplet covered by an extremely thin layer of water (≤ 200 nm) to enable accurate and effective cryogenic measurements.

I then compared the results of the various simulations, both 2D and 3D, focusing on the length (in the case of 2D simulations) and the area (in the case of 3D simulations) of the region with a thickness less than 200 nm, while keeping the simulation time constant. This approach allowed us to identify the optimal conditions for achieving the desired droplet spreading, providing valuable insights for improving experimental cryo-electron microscopy techniques.

3.2.3 Meshing Strategy

The meshing strategy was thoroughly studied to optimize the simulations in this model. It was essential to have a dense mesh in the interface regions between the two phases. However, an excessively fine mesh would cause problems for the solver and limit the ability to perform long-term numerical simulations with variable parameters.

In the initial simulations, I observed water dispersion at the interface between the water droplet and the air as the droplet began to fall, causing a loss of water volume. It was necessary to create very small elements that could follow the discontinuity, allowing for detailed point-by-point tracking of the phase interface (Fig. 3.3 c).

To keep the model lightweight (approximately 5000 elements instead of 12000 elements), a narrower "dummy" domain was created, within which the mesh was made even finer, while the rest of the model was discretized with a much coarser mesh. Additionally, thin boundary layers along the no-slip boundaries were defined through a dense distribution of elements along specific boundaries.

With this meshing strategy, we were able to reasonably track the spreading of the droplet profile on the impact substrate, providing a solid foundation for tackling the meshing of the 3D model.

In the 3D model, I discretized the surface of the droplet using uniformly sized triangles of 0.8 μm. Within the droplet, I adopted a tetrahedral structure (Fig. 3.3 e) while maintaining the same triangle size on the surface. This approach allowed us to accurately capture the complex geometry of the droplet and its spreading behavior on the cryo grid-cell (Fig. 3.3 d).

For the meshing process, I focused on the top surface of the cell, discretized with triangles sized at 0.3 μm. Subsequently, I used a technique called sweeping to extend this mesh three-dimensionally. The swept meshing technique involves taking the mesh defined on a starting surface and projecting it through the three-dimensional domain to reach a target surface, creating intermediate layers. In this case, I divided the volume into 20 layers.

I also implemented a specific strategy to optimize the model in terms of the computational resources needed for thermal calculations. The top surface of

the cell was discretized with variably sized triangles, ranging from 19 μm to 1.7 μm, to better fit the complex geometry of the grid. Again, the interior of the cryo grid-cell was meshed using the sweep technique, dividing the volume into 8 layers.

Overall, the resulting mesh consisted of approximately 500,000 elements. This approach allowed us to balance the accuracy of the simulation with computational efficiency, ensuring a detailed representation of the droplet spreading phenomenon on a cryo grid-cell.

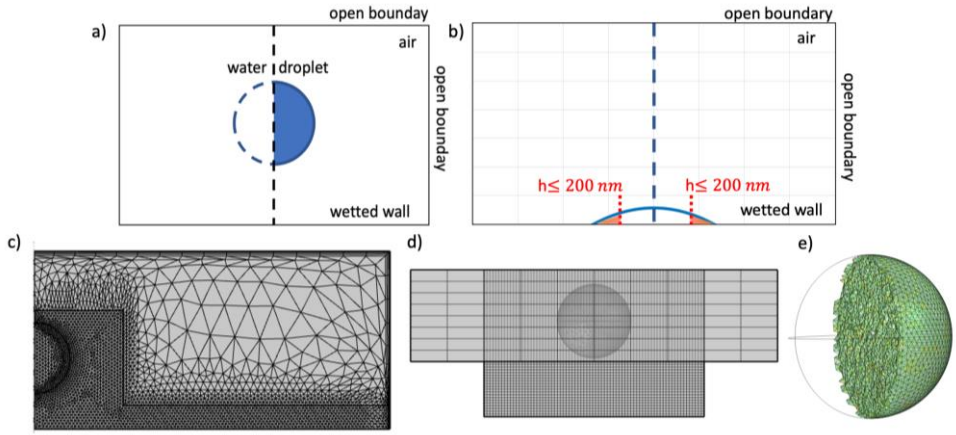

Figure 3.3 a) Configuration of the 2D axisymmetric simulation in Comsol, b) Spreading behavior of the droplet on a solid substrate with a focus on the area of interest: the region covered by a water thickness ≤ 200 nm; c) Detailed 2D meshing strategy with increased elements at the phase interface; and d) Comprehensive 3D structured meshing strategy.

3.3 2D Numerical Simulations

The 2D numerical simulations were conducted to explore the behavior of water droplets with varying diameters (5, 10, 20 μm) and different contact angles at the water/solid interface (1°, 5°, 10°). Initially, the droplet starts from a position approximately 2 μm from the substrate with an initial velocity of 5 m/s. The choice of this distance from the substrate was motivated by the desire to monitor the impact and spreading of the droplet in a short time, allowing the droplet to change shape due to the initial velocity before fully contacting the

substrate. This initial velocity was experimentally calculated in our previous work [15].

The simulations were performed in a 2D axisymmetric environment, where the images show only a section of the complete model, assuming the other part is symmetrical. Two distinct domains were defined for water and air, and the air domain surrounding the droplet had dimensions of 60 μm in length and 35 μm in height.

With a contact angle of 1°, the maximum radius of the droplet with initial diameters of 5-10-20 μm reaches final values of 11.5-18-34 μm, with corresponding maximum heights of 0.4-1.1-2.2 μm. The length covered by a water thickness ≤ 200 nm is 8 μm. With a contact angle of 5°, the maximum radius with initial diameters of 5-10-20 μm reaches final values of 8.6-16-31 μm, with maximum heights of 0.45-1.3-2.5 μm. The length covered by a water thickness ≤ 200 nm is 4 μm. With a contact angle of 10°, the maximum radius with initial diameters of 5-10-20 μm reaches final values of 6.7-14-29 μm, with maximum heights of 0.6-1.5-3 μm. The length covered by a water thickness ≤ 200 nm is 1 μm (Fig. 3.4 a-c).

The numerical simulations provided an in-depth understanding of the dynamics of water droplets, offering valuable insights into how the diameter and contact angle influence the final spreading of a droplet. Larger droplets resulted in a wider area with a thickness ≤ 200 nm compared to smaller droplets.

A key element that emerged from these simulations is that the wettability of the substrate is the crucial parameter. Indeed, regardless of the initial volume, once the droplets are fully spread on a surface, they cover the same length (in the 2D case) with a water thickness ≤ 200 nm. This suggests that improving the wettability of the substrate could be the key to optimizing the droplet spreading process.

Considering the results obtained from the 2D numerical simulations and taking into account the experimental information available to us, I decided to study a 3D model by selecting a droplet with a diameter of 20 μm and assigning a contact angle of 5° to the surface of the cryo grid-cell. Additionally, Figure 3.4 d-f, presents graphs of the spreading factor, which represents the change in the

radius of the droplet over time for different contact angles (θ = 1°, 5°, 10°). The spreading factor quantifies how quickly the droplet radius expands right after impact with the surface. This metric is essential as it allows us to measure the initial spreading phase, showing that the expansion of the droplet occurs almost entirely within the first moments and then significantly slows down. These results highlight that the initial moments of spreading are predominant and crucial compared to the subsequent regime, where spreading is slower and less significant.

Thanks to this analysis, I gained a essential insight for setting up our simulations: I configured the 3D simulation time at 20 μs, which is optimal for capturing the details of this rapid initial process.

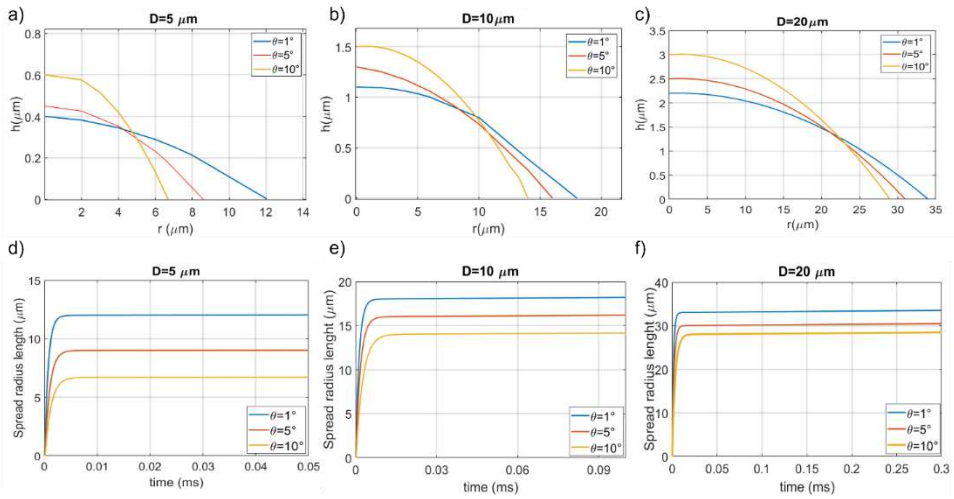

Figure 3.4 a-c) Radius length profile as a function of droplet height with varying contact angles (θ = 1°, 5°, 10°) for droplets fully spread on the substrate in a 2D axisymmetric simulation: a) droplet with an initial diameter of 5 μm, b) droplet with an initial diameter of 10 μm, c) droplet with an initial diameter of 20 μm; d-f) Radius length sprading factor as a function of time with varying contact angles (θ = 1°, 5°, 10°). The graph shows that droplet spreading occurs almost entirely in the initial moments after impact, followed by a much slower spreading.

3.4 3D Numerical Analysis - Comparative Analysis of Three Designs

The simulations were conducted on a cryo grid-cell, as illustrated in Figure 3.5. The cell size was set to 60 µm x 60 µm, and the contact angle on the surface was fixed at 5 degrees. A droplet was initially positioned exactly at the center of the cell, with a spherical shape and a diameter of 20 µm. The droplet was placed at an initial distance of 15 µm from the surface and reached a speed of 5 m/s after falling 1 µm.

The initial 3D studies focused on identifying the optimal position of the droplet within a single simple cell of the cryo-grid and assessing how this placement impacts the thickness and quality of the water film. As illustrated in Figure 3.5, the position of the droplet plays a critical role in achieving a uniform spread and maximizing the area covered by a water layer thinner than 200 nm—an essential parameter for accurate measurements.

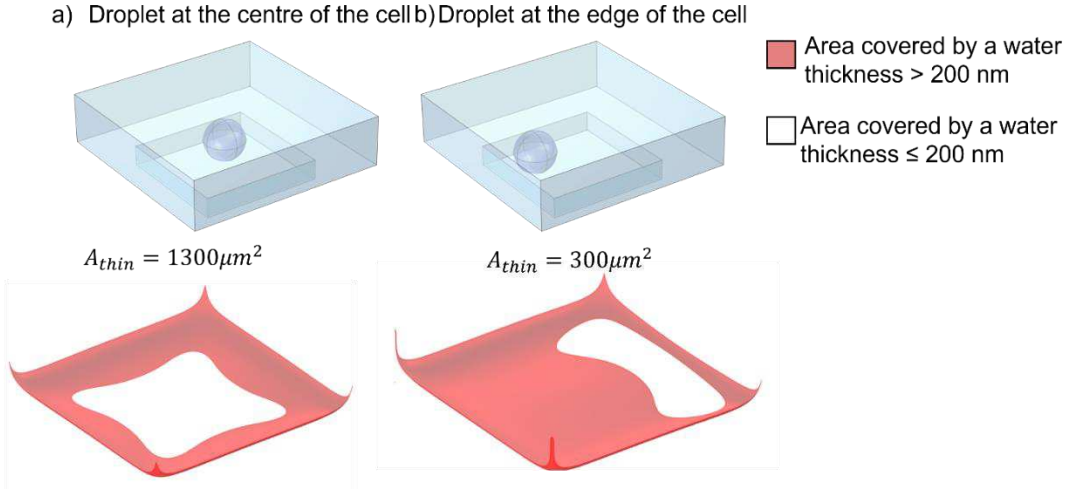

Figure 3.5 Distribution of water after a droplet has fallen into the cryo-grid cell and evaluation of the area with a water thickness ≤ 200 nm, which is useful for cryo-EM measurements: a) for a droplet at the center of the cell; and b) for a droplet near the edge of the cell

To gain a more detailed perspective, I created cross-sections (yz) of the cell in key areas: one at the center and two near the edges, with one closer to the droplet and the other farther away (Fig. 3.6). Then, I tracked the extent of the area where the thickness remains below 300 nm. The results reveal an interesting finding: in some configurations, it

is impossible to achieve such a thin layer, highlighting the need for an improved cell design.

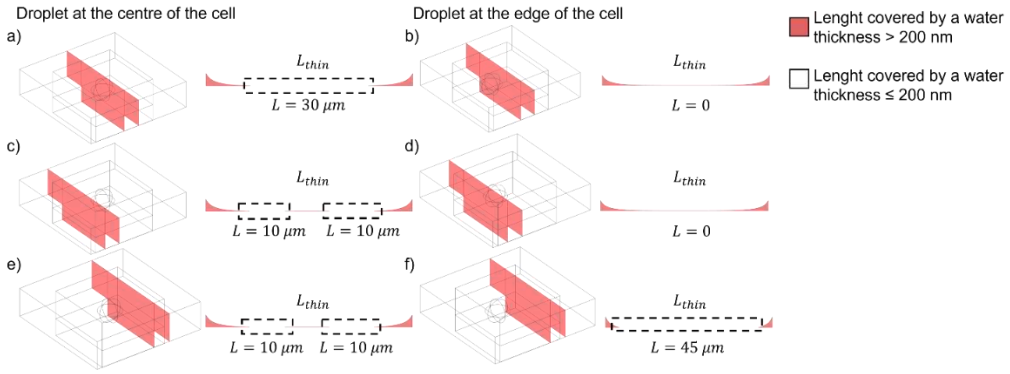

Figure 3.6 Cuts of the y-z planes at three different positions: a-b) at the center, c-d) near the left boundary, e-f) and near the right boundary, for both configurations (droplet at the center (a-c-e) of the cell and droplet near the left boundary of the cell (b-d-f). The lengths of the water with a thickness ≤ 200 nm along the defined cut planes are reported, which are consistent with the area measurements.

These findings suggest that an optimized cell layout could reduce sample waste and ensure adequate coverage, allowing for a more controlled water film distribution and increasing the likelihood of obtaining reliable and consistent measurements.

Therefore, simulations were designed and carried out with two other cryo grid-cell configurations: the "pillars grid-cell" and the "channels grid-cell." In the first configuration, pillars were introduced inside the cell, distributed at intervals of 6 µm, with a length of 10 µm on two sides of the cell and 5 µm on the other two sides. The width of the pillars remained constant at 3 µm, and the contact angle was set to 5 degrees for the pillars as well.

In the second configuration, micro-channels were implemented under the grid bars. These channels, 20 µm long and 5 µm wide, were designed to interconnect the various cells of the cryo grid, with walls having a constant contact angle of 5 degrees.

The idea behind the new configurations was to exploit the capillary phenomenon with the addition of high-wettability walls. The water rise

along these walls, due to the greater adhesive force between the water and the surfaces of the pillars and channels, overcomes the cohesive force between the liquid molecules. This behavior allows for an increase in the thin and uniform area available for cryogenic measurements, improving the effectiveness of cryogenic grids for advanced applications.

In just 20 μs, the design with pillars showed a significant improvement in droplet spreading compared to the classic simple cell. The area with a water thickness less than 200 nm increased from 1300 to 2200 μm² (Fig. 3.7 c i-ii). The volume risen by capillarity along the pillar walls was about 22% of the total volume. Through sectional analyses, I examined the heights reached by the liquid sample. As expected, the height of the liquid and thus the capillary rise at the points where the pillars are present reached much higher values than those at the center of the cell. Specifically, the minimum height of the liquid sample in the central pillar (the one closest to the droplet) is 1.5 μm, while in the outermost peripheral pillar it is 500 nm.

Moving the droplet towards the edge of the cell, an even more significant improvement is observed from the simple cell to the one with pillars. In particular, the area with a thickness less than 200 nm increases from 300 to 1500 μm² for the two mentioned configurations respectively (Fig. 3.7 d i-ii). In this case, the water volume captured by the pillars reaches the total volume.

In the channel configuration, a uniform spreading is observed during the 20 μs of simulation, although the areas with thin layers are significantly smaller compared to the other models. The water within the channels is drawn upwards by capillarity, and the heights are very similar to those found in the pillars. Through a cross-sectional cut at the center of the cell, I assessed that the thickness of the liquid sample is extremely thin, with a thickness not exceeding 200 nm. At the boundaries, the situation is different. Since the droplet is closer to the end of the channel, the water can already escape in this short period. In fact, in 20 μs, the initial water volume is lost, and the volume captured

by the channels is the total volume. Comparing the simple configuration with the one with channels, a significant increase in the area suitable for cryogenic measurements is observed, that is, with a thickness less than 200 nm. This increases from 300 µm² (simple configuration) to 1700 µm² (channel configuration) when the droplet is positioned centrally (Fig. 3.7 c i-iii). When the droplet is at the edges of the cell, the area increases from 300 µm² (simple configuration) to 1300 µm² (channel configuration) (Fig. 3.7 d i-iii).

Comparing all three simulations, it is evident that for a time interval of 20 µs, the pillar configuration is the most effective, whether the droplet is at the center or at the edges.

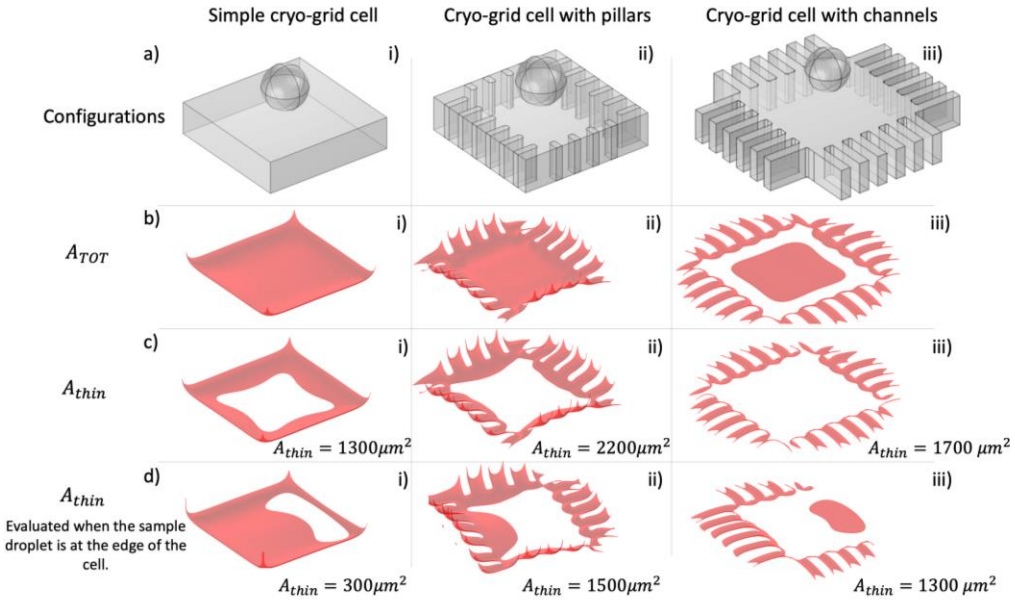

Figure 3.7. a) Representation of individual cryo-grid cells in the three analyzed configurations: (i) simple, (ii) with pillars, and (iii) with channels; b) Representation of the total area; c) Representation of the thin area with a thickness derived from the sample drop at the center of the model; and d) Representation of the thin area with a thickness obtained from the sample drop at the edge of the model.

3.5 Conclusions

I compared three distinct cryo-grid configurations: a conventional grid, one with pillars, and another with microchannels. The results indicate that the pillar configuration is particularly effective in improving droplet spreading compared to the other designs, both at the center and the edges of the grid cell, significantly optimizing sample preparation. The pillar configuration proved to be the most effective for several reasons. The pillars introduce highly wettable walls that harness capillary action. This effect is due to the increased adhesive force between the water and the pillar walls, which exceeds the cohesive force between the liquid molecules. Thanks to this behavior, the volume of water risen by capillarity along the pillar walls was about 22% of the total volume, promoting water spreading along the pillars and increasing the area covered by a very thin layer, ideal for cryogenic measurements.

Additionally, I addressed the issue of grid surface wettability, which is crucial for the quality of cryo-EM images. By measuring the contact angles before and after plasma treatment, I observed substantial improvements in surface wettability, in particular with treatments at 100 W. The plasma treatment modifies the surface properties depending on the material of the grid. For carbon grids, oxygen-containing functional groups such as hydroxyl (-OH), carbonyl (-C=O), and carboxyl (-COOH) are introduced, enhancing hydrophilicity and stabilizing the interaction with water. For copper grids, a thin layer of copper oxide forms, improving wettability without significantly altering mechanical properties. In the case of gold grids, the plasma primarily removes organic contaminants, resulting in a cleaner and more hydrophilic surface. These changes promote better interaction with water through hydrogen bonding, enabling the formation of thin, uniform water layers ideal for freezing and cryo-EM imaging. However, the potential impact on the structural stability of biomolecules requires further investigation.

This optimization of grid properties, combined with the new geometry, provides a strong foundation for improving cryo-EM image quality. Our work successfully tackled the challenge of controlling droplet spreading on cryo-grids by introducing new configurations and improving surface wettability.

These advances have significant implications for cryo-EM sample preparation, paving the way for a better understanding of biological reactions in dynamic and non-equilibrium systems. The optimized grid configurations and enhanced wettability offer a solid platform for future developments in this research field

References

1. Yip, K. M., Fischer, N., Paknia, E., Chari, A., & Stark, H. (2020). Atomic-resolution protein structure determination by cryo-EM. *Nature*, *587*(7832), 157-161.
2. Fischer N, Konevega AL, Wintermeyer W, Rodnina MV, Stark H (2010) Ribosome dynamics and tRNA movement by time- resolved electron cryomicroscopy. Nature 466(7304):329–333.
3. Chen B, Kaledhonkar S, Sun M, Shen BX, Lu ZH, Barnard D, Lu TM, Gonzalez RL, Frank J (2015) Structural dynamics of ribosome sub- unit association studied by mixing-spraying time-resolved cryogenic electron microscopy. Structure 23(6):1097–1105.
4. Feng X, Fu Z, Kaledhonkar S, Jia Y, Shah B, Jin A, Liu Z, Sun M, Chen B, Grassucci RA, Ren Y, Jiang H, Frank J, Lin Q (2017) A fast and effective microfluidic spraying-plunging method for high-resolution single-particle cryo-EM. Structure 25(4):663–670 e663.
5. Klebl, D. P., Monteiro, D. C., Kontziampasis, D., Kopf, F., Sobott, F., White, H. D., ... & Muench, S. P. (2020). Sample deposition onto cryo-EM grids: from sprays to jets and back. *Acta Crystallographica Section D: Structural Biology*, *76*(4), 340-349
6. Fu Z, Kaledhonkar S, Borg A, Sun M, Chen B, Grassucci RA, Ehrenberg M, Frank J (2016) Key intermediates in ribosome recycling visual- ized by time-resolved cryoelectron microscopy. Structure 24(12):2092–2101.
7. Lu ZH, Shaikh TR, Barnard D, Meng X, Mohamed H, Yassin A, Mannella CA, Agrawal RK, Lu TM, Wagenknecht T (2009) Monolithic microfluidic mixing-spraying devices for time- resolved cryo-electron microscopy. J Struct Biol 168(3):388–395.
8. Shaikh TR, Yassin AS, Lu ZH, Barnard D, Meng X, Lu TM, Wagenknecht T, Agrawal RK (2014) Initial bridges between two

ribosomal subunits are formed within 9.4 milliseconds, as studied by time-resolved cryo-EM. Proc Natl Acad Sci U S A 111(27)

9. Dashti, A. et al. Trajectories of the ribosome as a Brownian nanomachine. Proc. Natl Acad. Sci. USA 111, 17492–17497 (2014).
10. Frauenfelder, H., Sligar, S. & Wolynes, P. The energy landscapes and motions of proteins. Science 254, 1598–1603 (1991).
11. Bai, X. Chen, McMullan, G. & Scheres, S. H. W. How cryo-EM is revolutionizing structural biology. Trends Biochem. Sci. 40, 49–57 (2015).
12. Haselbach, D. et al. Structure and conformational dynamics of the human spliceosomal bact complex. Cell 172, 454–464.e11 (2018).
13. Fiedler, E. et al. Snapshot of a key intermediate in enzymatic thiamin catalysis: crystal structure of the α-carbanion of (α,β-dihydroxyethyl)-thiamin diphosphate in the active site of transketolase from Saccharomyces cerevisiae. Proc. Natl Acad. Sci. USA 99, 591–595 (2002).
14. Leiros, I., McSweeney, S. & Hough, E. The reaction mechanism of phospholipase D from Streptomyces sp. strain PMF. Snapshots along the reaction pathway reveal a pentacoordinate reaction intermediate and an unexpected final product. J. Mol. Biol. 339, 805–820 (2004).
15. Torino, S., Dhurandhar, M., Stroobants, A., Claessens, R., & Efremov, R. G. (2023). Time-resolved cryo-EM using a combination of droplet microfluidics with on-demand jetting. *Nature Methods*, *20*(9), 1400-1408.
16. Jain, T., Sheehan, P., Crum, J., Carragher, B., & Potter, C. S. (2012). Spotiton: a prototype for an integrated inkjet dispense and vitrification system for cryo-TEM. *Journal of structural biology*, *179*(1), 68-75.
17. Wei, H., Dandey, V. P., Zhang, Z., Raczkowski, A., Rice, W. J., Carragher, B., & Potter, C. S. (2018). Optimizing "self-wicking" nanowire grids. *Journal of structural biology*, *202*(2), 170-174.

18. Razinkov, I., Dandey, V. P., Wei, H., Zhang, Z., Melnekoff, D., Rice, W. J., ... & Carragher, B. (2016). A new method for vitrifying samples for cryoEM. *Journal of structural biology*, *195*(2), 190-198.
19. Rubinstein, J. L., Guo, H., Ripstein, Z. A., Haydaroglu, A., Au, A., Yip, C. M., ... & Kwok, T. (2019). Shake-it-off: a simple ultrasonic cryo-EM specimen-preparation device. *Acta Crystallographica Section D: Structural Biology*, *75*(12), 1063-1070.
20. Wang, X., Xu, B., Guo, S., Zhao, Y., & Chen, Z. (2023). Droplet impacting dynamics: Recent progress and future aspects. *Advances in Colloid and Interface Science*, 102919
21. Zhang, H., Zhang, X., Yi, X., He, F., Niu, F., & Hao, P. (2021). Effect of wettability on droplet impact: Spreading and splashing. *Experimental Thermal and Fluid Science*, *124*, 110369
22. Aksoy, Y. T., Eneren, P., Koos, E., & Vetrano, M. R. (2022). Spreading of a droplet impacting on a smooth flat surface: How liquid viscosity influences the maximum spreading time and spreading ratio. *Physics of Fluids*, *34*(4).
23. Liu, X., Zhang, X., & Min, J. (2019). Spreading of droplets impacting different wettable surfaces at a Weber number close to zero. *Chemical Engineering Science*, *207*, 495-503.
24. Unwin, N. & Fujiyoshi, Y. Gating movement of acetylcholine receptor caught by plunge-freezing. J. Mol. Biol. 422, 617–634 (2012).
25. Berriman, J. & Unwin, N. Analysis of transient structures by cryo-microscopy combined with rapid mixing of spray droplets. Ultramicroscopy 56, 241–252 (1994).
26. Subramaniam, S. & Henderson, R. Electron crystallography of bacteriorhodopsin with millisecond time resolution. J. Struct. Biol. 128, 19–25 (1999).
27. Šrajer, V. & Schmidt, M. Watching proteins function with time-resolved X-ray crystallography. J. Phys. D. Appl. Phys. 50, 373001 (2017).

28. Miller, T. C. R., Locke, J., Greiwe, J. F., Diffley, J. F. X. & Costa, A. Mechanism of head-to-head MCM double- hexamer formation revealed by cryo-EM. Nature (2019).
29. Chen, C.-Y., Chang, Y.-C., Lin, B.-L., Huang, C.-H. & Tsai, M.-D. Temperature-resolved Cryo-EM uncovers structural bases of temperature- dependent enzyme functions. J. Am. Chem. Soc. jacs.9b10687 (2019).
30. Frank, J. Time-resolved cryo-electron microscopy: recent progress. J. Struct. Biol. 200, 303–306 (2017).

4

Analytical Model Development for Capillary Microfludic System with Experimental Validation

The expertise gained in capillarity during my research abroad was applied to the enhancement of the flexible microsystems discussed in Ch. 1 and 2, leading to the development of a capillary microdevice on flexible material. In these systems, the flow within microchannels is entirely driven by the surface tension of the liquid and the properties of the channel walls, offering portability without the need for external pumps and greater energy efficiency through self-sustained flow (Fig.4). The absence in the literature of a clear, general analytical model to predict meniscus movement in microchannels with variable wettability, particularly in the initial stages of motion, made it necessary to develop a new analytical model. The model was specifically designed to describe behavior under these conditions and was then rigorously validated experimentally across a range of microchannel configurations, demonstrating accuracy and effectiveness in controlling flow within flexible microsystems. Moreover, the capillary filling of a flexible microfluidic system with an integrated plasmonic sensor, was demonstrated, showing that proper filling occurs even under conditions of high curvature.

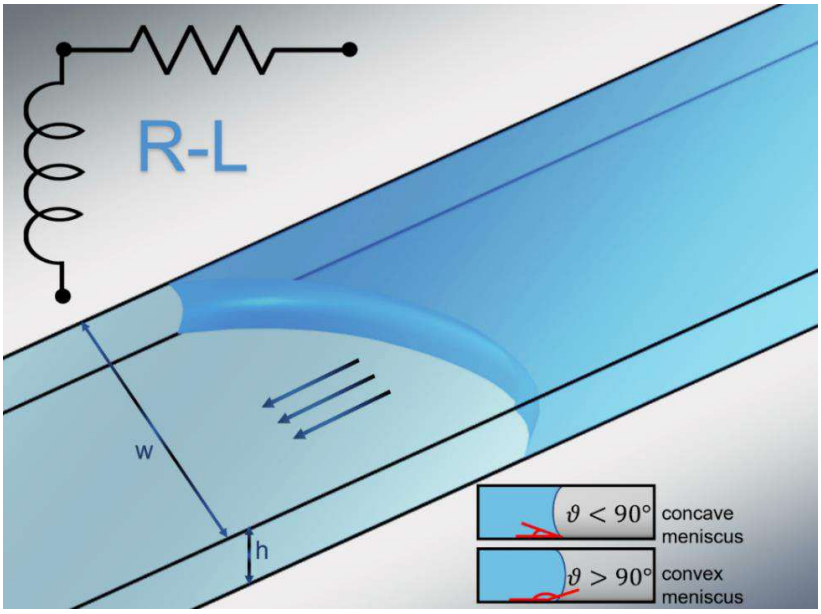

Figure 4. Sketch of the formation of the meniscus in a fluid within a rectangular microfluidic channel. Formation of a concave and convex meniscus depending on the contact angle.

4.1 Capillary System (CS)

Capillary systems utilize surface interactions between a liquid and the walls of a channel to generate fluid movement without relying on external energy sources. Their operation is based on capillarity, where the surface tension of the liquid and the contact angle with the channel walls influence both the shape of the meniscus and the advancement of the fluid speed within the microchannel [1-10]. Capillary flow is spontaneously triggered when the liquid comes into contact with a highly wettable surface, pushing the fluid through the channels due to differences in surface tension. This eliminates the need for external pumps, resulting in devices that are more energy-efficient, portable, and user-friendly [19].

The passive transport offered by capillary systems is used in numerous applications, including diagnostic devices [11], immunoassays [12-13], cooling systems such as heat pipes [14], and even in microgravity environments in space, where conventional pumping methods are unsuitable [15]. In diagnostic devices like biosensors, precise control of capillary flow is essential, as the signal depends on the correct timing of biochemical reactions and the precise localization within the device. The ability to manage flow accurately improves the efficiency and sensitivity in the transport of biological samples or reagents. The speed of capillary flow depends on several factors, including surface energy, the viscosity of the liquidy, and the wettability of the channel walls. Careful design of microchannels allows for flow optimization. This phenomenon has been thoroughly studied over the years by numerous researchers.

In 1991, White [20] analyzed the momentum balance for fully developed laminar flow in a two-dimensional (2D) channel. His analysis provided analytical solutions for the velocity profile and pressure distribution, highlighting key characteristics of laminar flow, such as the typical parabolic velocity profile and the linear pressure drop along the channel. This investigation offered important insights into how viscous forces dominate over

inertial forces, which is critical for the design of fluid systems in various engineering applications. Later, Zimmermann et al. [21] expanded White's theory by addressing the problem in a three-dimensional (3D) context in channels with surfaces of different wettability. However, their analysis was limited to stationary fluid in a fully filled channel, following the Poiseuille approximation, and did not consider the dynamics of a moving meniscus.

In 2011, Song [22] developed a model to describe the behavior of the meniscus in a rectangular channel, assuming uniform wettability for all walls, implying a constant contact angle. Later, Mohammed [23] modified Song's model to compare experimental data on the average velocity of fluid moving by capillarity in microchannels. Although Mohammed's model was valid in stationary conditions, uncertainties and discrepancies were observed during the early stages of flow.

Despite the growing interest in capillary-based microfluidics, a clear and comprehensive understanding of fluid dynamics in microfluidic channels with walls made of materials with varying wettability properties was still lacking. Specifically, the behavior of the fluid during the initial stages of channel filling had not been thoroughly studied. This gap motivated us to develop a general analytical model, supported by experimental validation, capable of dynamically predicting the displacement and speed of the meniscus, influenced solely by capillary forces.

The model developed can be applied to both microfluidic systems built using conventional techniques and simpler, more cost-effective methods. It allows for an accurate estimation of the average capillary flow velocity in a three-dimensional rectangular microfluidic channel, taking into account the interactions between the fluid and the channel walls, which vary depending on the wettability of the materials used. This makes it suitable for use in capillary microfluidic systems made with traditional techniques, such as soft lithography, where typically three walls are made of a hydrophobic material (PDMS) and the fourth is hydrophilic (glass), as well as with more modern techniques like xurography and laser cutting, which allow for the combination of different materials for the walls. Experimental validation of the model, conducted on microfluidic devices fabricated using these techniques, demonstrated its

reliability in predicting the dynamic of the fluid behavior in various channel configurations.

4.2 Analytical model

The model developed in this work is based on the well-established analogy between the behavior of fluid systems and electrical circuits [24]. Under laminar and steady flow conditions, Poiseuille's law can be used to describe the pressure variation along the microfluidic channel, expressed by the equation:

$$\Delta Pc = R_{\mathrm{h}} Q \qquad (1)$$

Here, ΔPc represents the pressure difference between the ends of the channel, Q is the fluid flow rate, and R_{h} is the hydraulic resistance of the channel, which depends on the shape of the meniscus and the geometry of the channel. This relation is analogous to Ohm's law, where ΔPc behaves like a voltage difference, Q represents the electrical current, and R_{h} represents resistance. Based on this analogy, Kirchhoff's law for capillary systems (CS) can be written as:

$$\Delta Pc - R_{\mathrm{h}} Q = 0 \qquad (2)$$

In the case of steady flow, $\frac{dQ}{dt} = 0$. However, during the initial stages of channel filling, a transient behavior must be considered, where the flow rate varies with time, i.e. $\frac{dQ}{dt} \neq 0$. To describe this transient phase, a hydraulic concept analogous to electrical inductance L is introduced, which in a circuit relates the change in electrical current to the potential difference. Similarly, hydraulic inductance L_{h} connects the variation in flow rate to the pressure difference:

$$\Delta P = -L_{\mathrm{h}} \frac{dQ}{dt} \qquad (3)$$

As in the electrical case, hydraulic inductance depends on the geometric characteristics of the circuit. To derive the relationship between hydraulic inductance and the geometry of the CS, one must consider that variations in the flow rate over time induce a pressure change within the CS. Therefore, the second law of dynamics can be applied, where the tension force is related to the pressure variation across the cross-section of the channel. The hydraulic inductance can thus be expressed as:

$$L_{\mathrm{h}} = \frac{\rho l}{S} \tag{4}$$

Where ρ is the fluid density, l is the length of the filled channel, and S is its cross-sectional area. During the filling process, the length l varies over time, so hydraulic inductance is not constant. Therefore, the pressure difference is affected not only by the flow rate variation over time but by the entire flow:

$$\Delta P = -\frac{d(L_{\mathrm{h}}(t)Q)}{dt} \tag{5}$$

$$\Delta Pc - R_{\mathrm{h}}(t)Q = \frac{d(L_{\mathrm{h}}(t)Q)}{dt} \tag{6}$$

To describe the filling of the CS, it is necessary to analyze in detail the capillarity and resistive terms. The model developed can be applied to both microfluidic systems built using conventional techniques and simpler, more cost-effective methods. The capillary pressure inside a microfluidic channel can generally be derived from the free energy associated with the solid-liquid-gas interface [25-26]:

$$U_T = A_{\mathrm{sl}}\,\sigma_{\mathrm{sl}} + A_{\mathrm{sl}}\sigma A_{lg}\;\sigma_{lg} + A_{sg}\;\sigma_{sg} \tag{7}$$

where A_{sl}, A_{lg} , A_{sg} are the areas of the solid-liquid, liquid-gas, and solid-gas interfaces, respectively, and σ_{sl}, σ_{lg}, σ_{sg} are the corresponding surface energies per unit area. In general, capillary pressure is the change in interfacial energy with respect to the liquid volume:

$$\Delta Pc = -\frac{dU_T}{dV_{\mathrm{l}}} \tag{8}$$

The three surface energies are related through the contact angle θ , defined by Young's equation:

$$\sigma_{sg} = \sigma_{\mathrm{sl}} + \sigma_{lg}cos(\theta) \tag{9}$$

Substituting the previous relations, and assuming that both the height h and width w of the channel remain constant during the flow, the capillary pressure can be written as [26]:

$$\Delta Pc = \sigma[cos(\theta)\frac{dA_{\mathrm{sl}}}{dV_{\mathrm{l}}} - \frac{dA_{lg}}{dV_{\mathrm{l}}}] \tag{10}$$

In this context, σ represents the liquid-gas surface tension σ_{lg} and θ indicates the contact angle on a generic surface. As the liquid front advances, the shape and area of the liquid-gas interface A_{lg} remain constant, implying that the variation of the interface area with respect to the liquid volume is zero, i.e.:

$$\frac{dA_{lg}}{dV_l} = 0 \tag{11}$$

However, the contact area between the liquid and solid A_{sl}, varies with the liquid front displacement, and this variation can be described as:

$$\frac{dA_{sl}}{dV_l} = \frac{\frac{dA_{sl}}{ds}}{\frac{dV_l}{ds}} = \frac{\frac{(2w+2h)ds}{ds}}{\frac{(hw)ds}{ds}} \tag{12}$$

Substituting this expression into the capillary pressure equation, we obtain:

$$\Delta Pc = 2\sigma cos(\theta)[\frac{1}{w} + \frac{1}{h}] \tag{13}$$

This formula is valid only if the contact angle is the same on all surfaces of the rectangular channel. However, in a more general situation, the contact angles on the four channel surfaces (top, bottom, right, and left) may differ. In this case, the capillary pressure must be calculated considering distinct contact angles for each surface θ_b, θ_t , θ_l, θ_r. The general formula becomes (27):

$$\Delta P_c = \frac{\sigma(\cos(\theta_t) + \cos(\theta_b))}{h} + \frac{\sigma(\cos(\theta_r) + \cos(\theta_l))}{hw} \tag{14}$$

For the resistive term, represented as $R_\mathrm{h}Q$, the hydraulic resistance R_h for a rectangular channel is defined as:

$$R_h = \frac{12\mu l}{\gamma b^3 a} \tag{15}$$

where μ is the fluid viscosity, l is the channel length, and a and b are the channel dimensions with the condition that $a > b$.

The parameter γ is a geometric factor related to the meniscus shape inside the rectangular channel and is defined as [26]:

$$\gamma = 1 - 192\beta \sum_{i=odd} \frac{\tanh(i2\pi\beta)}{(i\pi)^5} \tag{16}$$

where $\beta = \frac{b}{a}$. The flow rate Q for a rectangular channel can be expressed as:

$$Q = Sv = ab\frac{dl}{dt} \tag{17}$$

since the cross-sectional area S is defined as ab, and the average velocity of the liquid along the channel can be described as:

$$v = \frac{dl}{dt} \tag{18}$$

By combining the expressions for hydraulic inductance L_{h} capillary pressure ΔPc and hydraulic resistance R_{h} we arrive at a differential equation that describes the dynamics of capillary filling within the channel. This equation is:

$$\rho \frac{dlv}{dt} = \frac{\sigma(cos\theta_t + cos\theta_b)}{h} + \frac{\sigma(cos\theta_r + cos\theta_l)}{w} - \frac{12\mu lv}{\gamma b^2} \tag{19}$$

This equation can be rewritten in a more compact form as:

$$\dot{z} + Bz = A \tag{20}$$

where:

$$A = \frac{\sigma(cos\theta_t + cos\theta_b)}{\rho h} + \frac{\sigma(cos\theta_r + cos\theta_l)}{\rho w} \tag{21}$$

And

$$B = \frac{12\mu}{\rho\gamma b^2} \tag{22}$$

The solution of the differential equation is:

$$z(t) = c_0 e^{-Bt} + \frac{A}{B} \tag{23}$$

where c_0 is an arbitrary constant of the differential equation. Imposing the initial condition $z(0) = 0$ for a fluid starting from zero velocity, the solution for $z(t)$ is:

$$z(t) = \frac{A}{B}(1 - e^{-Bt}) \tag{24}$$

Since $z = l_v$ and $v = \frac{dl}{dt}$, the equation for the filling length $l(t)$ can be expressed as:

$$l\frac{dl}{dt} = \frac{A}{B}(1 - e^{-Bt}) \tag{25}$$

Integrating, we obtain:

$$\int ldl = \int \frac{A}{B}(1 - e^{-Bt})dt \tag{26}$$

$$\frac{l^2}{2} = \frac{At}{B} + \frac{A}{B^2}e^{-Bt} + c_0 \tag{27}$$

Assuming a general initial condition for the fluid position $l(0) = l_0$, the filling length can be expressed as:

$$l(t) = \sqrt{{l_0}^2 + 2\frac{A}{B^2}(e^{-Bt} - 1) + 2\frac{At}{B}} \tag{28}$$

Moreover, considering the previous equation and the relationship $z = l_v$, the following result for the average velocity of fluid is obtained:

$$v(t) = \frac{A}{Bl}(1 - e^{-Bt}) \tag{29}$$

From this equation, the flow rate $Q(t)$ as a function of time can be derived:

$$Q(t) = \frac{SA}{Bl}(1 - e^{-Bt}) \tag{30}$$

This result closely resembles the solution for the current in an LR electrical circuit with zero initial current, given by:

$$\frac{\Delta V}{R}(1 - e^{-1/\tau}) \tag{31}$$

where $\tau = {}^{L}/_{R}$To demonstrate this analogy, the electrical terms $\Delta V, I(t), R$ and L are replaced with their hydraulic counterparts ΔPc, Q(t), R_{h} and L_{h} in the previous equation, yielding:

$$\frac{\Delta P_c}{R_h}(1 - e^{-t/\tau_h}) \tag{32}$$

con $\tau_h = L_{\mathrm{h}}/\ R_{\mathrm{h}}$.

If we consider $w > h$ and substitute the expressions for $\Delta Pc\ R_{\mathrm{h}}$ and $L_{\mathrm{h}}$the flow rate equation takes the following form:

$$Q(t) = [\frac{\gamma hS\sigma}{12\mu l}(cos\theta_t + cos\theta_b) + \frac{\gamma h^2 S\sigma}{12\mu lw}(cos\theta_l + cos\theta_r)]((1 - e^{-\frac{12\mu t}{\rho\gamma h^2}}) \tag{33}$$

Recalling the definitions of the coefficients A and B in the previous equations, the flow rate equation simplifies further as:

$$Q(t) = \frac{SA}{Bl}(1 - e^{-Bt}) \tag{34}$$

This formulation is consistent even when $h > w$, confirming the analogy between capillary filling and the behavior of an LR electrical circuit.

This model allows for an accurate description of capillary filling dynamics, accounting for variable geometry and complex physical interactions between the fluid and the channel.

4.3 Numerical Analysis Model Validation

A series of numerical analyses was conducted by designing microfluidic channels and simulating the flow within them under various wettability conditions, using the Phase Field module in COMSOL Multiphysics. This approach allowed us to track the interface between two phases (air and water)

and control the flow based on the interaction between surface tension, channel wall properties, and fluid characteristics.

The simulated channels have a length of 20 mm, a width of 0.5 mm, and a height of 0.1 mm. The surface properties of the channel walls were modified from hydrophilic to hydrophobic to observe how the meniscus shape changes. The Figure 4.1 shows the initial domains of water and air before the simulation begins and immediately afterward, highlighting the meniscus formation influenced by the surface of channels properties.

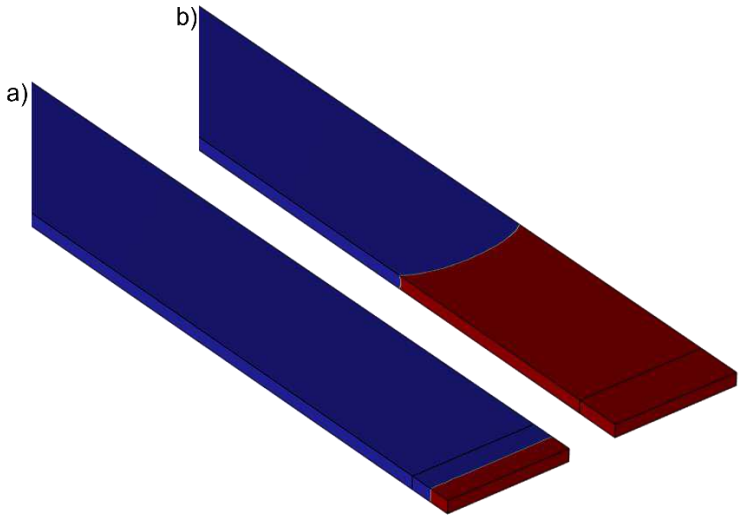

Figure 4.1. a) Initial domains of water and air before the simulation starts; b) Meniscus formation, influenced by the surface properties of the channel.

To monitor the flow velocity, probes were inserted within the channel, and a graph of the average velocity trend was generated. The results were compared with those from the analytical model, and, as the comparison shows (Fig. 4.2), the trends are similar, though not perfectly matching. A more in-depth analysis, conducted with technical support from the software, revealed that the primary issue lies in the initial velocity of the numerical model: despite being set to zero, a non-zero initial value was observed, affecting the subsequent trend. Nonetheless, the behavior remains consistent with expectations for capillary

flow, characterized by a rapid initial decrease in velocity, followed by stabilization toward a "terminal velocity."

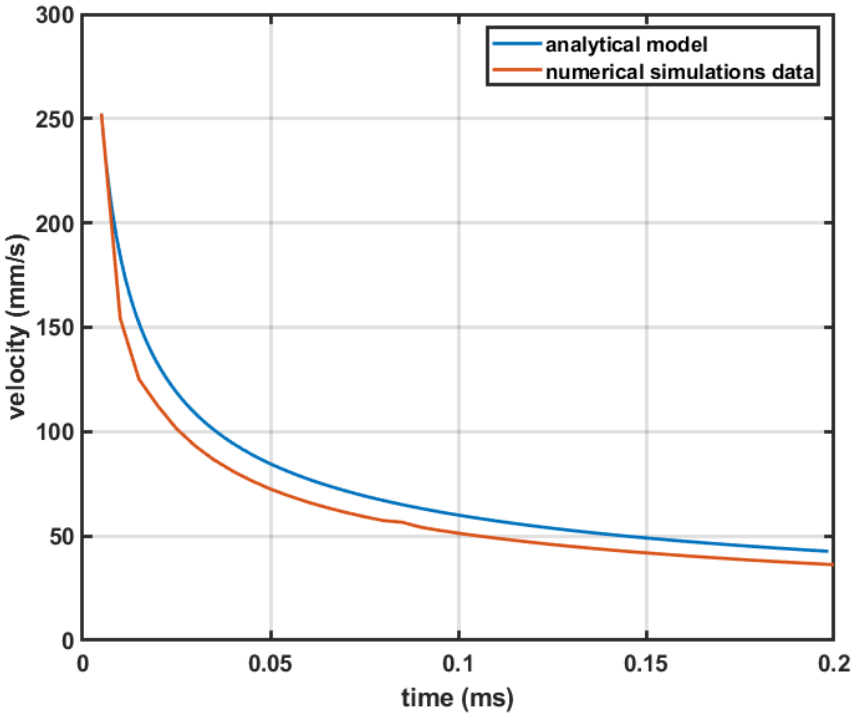

Figure 4.2 Comparison between the analytical model and numerical simulation data.

The main hypothesis is that there is a numerical issue with the acceleration applied to the meniscus, due to the absence of a capillary curve at the interface. While a preformed interface could mitigate this effect, our goal is to simulate both the initial conditions and the steady-state regime under various wettability conditions. The simulations confirm the expected trend and produce a

meniscus shape consistent with experimental observations, effectively capturing the crucial initial moments of flow before stabilization (Fig. 4.3)

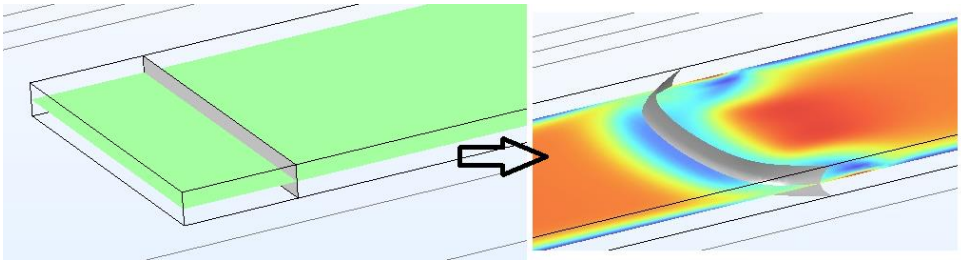

Figure 4.3. Velocity profile of the fluid flow over time. The initial peak represents the acceleration of the fluid as it rapidly adheres to the channel walls, defined by the contact angle. Following this, the velocity stabilizes at a terminal value, indicating the formation of a fully developed and stable meniscus.

4.4 Experimental Model Validation by Development of CS

We validated our model through a series of experiments conducted on microfluidic channels manufactured using both traditional methods and innovative approaches (Fig. 4.4) (as shown in Table II).

Conventional techniques for fabricating microfluidic devices, such as soft lithography and replica molding, require well-equipped laboratories to create small-scale structures, typically using PDMS. Devices produced with these methods usually have three walls made of PDMS and one of glass, which leads to significant differences in wettability properties: untreated PDMS tends to be hydrophobic, while glass is naturally hydrophilic. With the increasing demand for more accessible and portable solutions, new fabrication techniques have been introduced, such as xurography, which allows the precise creation of devices and the combination of different materials, each with specific

wettability properties. This offers greater flexibility in the design and production of microfluidic channels.

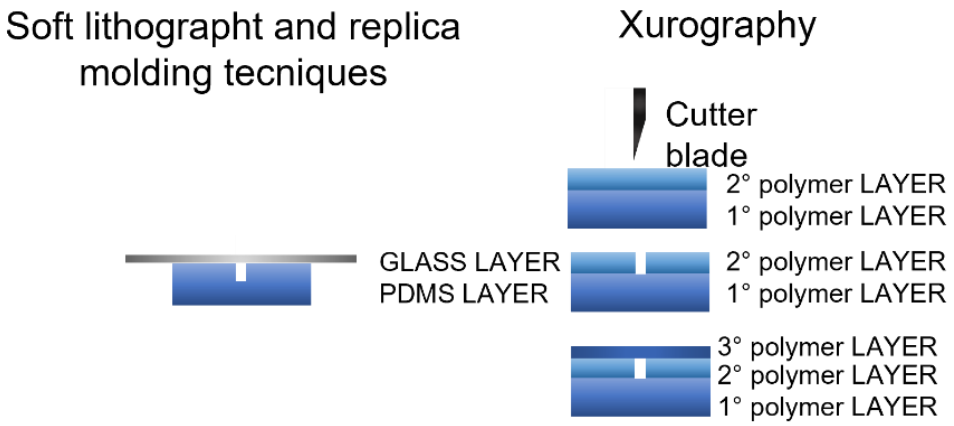

Figure 4.4. Two fabrication methods for CS were used: soft lithography: the classic method for creating precise microstructures in PDMS; xurography: fabrication using a cutting plotter, a fast and low-cost alternative for flexible materials.

The proposed model was validated using microfluidic channels, whose wettability was experimentally characterized by measuring the contact angle. The microfluidic channels were fabricated using both soft lithography and xurography techniques.

The structures obtained through soft lithography were designed with channels of varying widths, ranging from 50 μm to 500 μm. The process began with the exposure of a negative photoresist (SU8-3010) to UV light, creating a raised pattern that defines the channel height on the substrate. The photoresist thickness, which determines the channel height, was set at 15 μm. This resulted in a β ratio of 0.3 for the 50 μm wide channels and 0.03 for the 500 μm ones. I then used the mold to replicate the channels in PDMS, sealing the structure with a 160 μm thick glass substrate through oxygen plasma treatment, which ensured good adhesion. In this way, the final channels had three walls made of PDMS and one of glass. After plasma treatment, the measured contact angle was 80° for the PDMS and 10° for the glass (for details, see Table II, materials labeled with superscript 1).

Materials (t/b/l/r)	*Technology*	$\beta(h/w)$	R^2
PDMS[1]/Glass[1]/PDMS[1] /PDMS[1]	SL	0.03	0.93
*PVA/Glass/Tape/Tape	XG	0.10	0.98
PVA/PDMS/Tape/Tape	XG	0.10	0.96
PVA/PMMA/Tape/Tape	XG	0.10	0.81
PVA/Si/Tape/Tape	XG	0.10	0.95
PVA/Glass/Tape/Tape	XG	0.13	0.98
PVA/PDMS/Tape/Tape	XG	0.13	0.90
*PVA/Glass/Tape/Tape	XG	0.20	0.98
PDMS[1]/Glass[1]/PDMS[1] /PDMS[1]	SL	0.30	0.75
PVA/Glass/Tape/Tape	XG	0.50	0.90
*PDMS/Glass/PDMS/PDMS	XG	1.00	0.95
*PDMS/Glass/PDMS/PDMS	XG	1.30	0.90
PDMS/Glass/PDMS/PDMS	XG	2.00	0.97

Table II. Analysis of the results obtained for rectangular microfluidic channels fabricated using soft lithography (SL) or xurography (XG), with different materials for the top, bottom, left, and right walls, and varying values of β. Channels marked with an asterisk (∗) are those analyzed in detail in Fig.4.5, while those indicated with a superscript (1) denote cases where an oxygen plasma treatment was applied to enhance the hydrophilicity of the material, ensuring effective sealing between the channel walls

I adopted a cost-effective approach for the fabrication of microfluidic channels, using xurography with a cutting plotter to create the devices. This method allowed us to produce channels that were 2 cm long and 100 μm high, with variable widths between 200 μm and 1000 μm, corresponding to β values of 0.5, 0.2, 0.13, and 0.1. The channel design, developed using CAD software, was transferred to the plotter to etch an adhesive tape applied to a polyvinyl acetate (PVA) substrate. We selected PVA for its wettability properties (contact angle of 60°), transparency, and flexibility. The channels were sealed using double-sided adhesive tape. This sealing system was tested on various substrates,

including glass, silicon, PDMS, and PMMA, which presented contact angles of 40°, 80°, 100°, and 70°, respectively.

We also used xurography to create channels of different widths (500 μm, 750 μm, and 1000 μm) by cutting PDMS layers with thicknesses of 1000 μm. This allowed us to examine capillary flow behavior even in conditions where the height h was greater than or equal to the width w, with β values of 2, 1.3, and 1. The channels produced had three walls made of PDMS and one of glass.

During the experiments, we placed a drop of red dye (30 μL) at the entrance of each channel, and the fluid movement was driven by capillary forces and recorded with a digital microscope at 30 frames per second (FPS). The video data were analyzed using MATLAB software, which tracked the meniscus movement over time, identifying position changes based on the color difference of the dye between consecutive frames. From this data, a graph illustrating the fluid velocity inside the channel was extracted. Table II summarizes the channel configurations produced to compare the experimental results with our theoretical model. For each configuration, the material used for the four walls (top, bottom, left, and right), the fabrication technique used, the β ratio between height h and width w, and the coefficient of determination R^2, which represents the correlation between the experimental data and the model, are reported.

To demonstrate the effectiveness of the model, the average velocity over time was plotted for specific cases. Figures 4.5 a and 4.5 b show the cases with $\beta = 1, w = 1\,mm;\ h = 1\,mm$ and $\beta = 1.3, w = 0.75\,mm, h = 1\,mm$, obtained using materials with well-defined contact angles on all channel surfaces. The experimental results were compared with the analytical model, showing good values of ε_v and R^2 (see Table II). The graphs include error bars representing the trend of the experimental data, calculated as the average deviations from the theoretical model and obtained from an experimental campaign of 10 measurements. The exeperimental data show an error of $\pm 3.1\ mm/s$ for β = 1.3 and $\pm 1.5\ mm/s$ for β = 1 , demonstrating a good agreement between the analytical model and the experimental data. In contrast,

Figures 4.5 c and 4.5 d illustrate the cases where $\beta = 0.1, w = 1\ mm, h = 100\ \mu m$ *and* $\beta = 0.2, w = 500\ \mu m, h = 100\ \mu m$, with an error of $\pm 1.5\ mm/s$ was observed for β = 0.1 and $\pm 2.2\ mm/s$ for β = 0.2. In these experiments, the top layer was made of PVA, the bottom layer of glass, while the side walls of channel were defined by double-sided adhesive tape with a thickness of 100 μm.

Due to the reduced thickness of the tape making it difficult to accurately measure the contact angle of the sidewalls, the analytical model was used to fit the experimental data, treating the contact angles as unknown parameters. To achieve convergence, the Levenberg-Marquardt algorithm was applied. The results of the fit are shown in Table II, and as seen in Figures 4.5 a and 4.5 b, the theoretical and experimental velocities are very similar, with estimated contact angles on the sidewalls around 85°, consistent with the hypothesis that adhesive residues on the tape reduce the wettability of the surfaces.

This same approach was applied to all configurations using double-sided adhesive tape to define the channels. The data presented in Table II confirm that the proposed model not only accurately describes the capillary flow dynamics in rectangular channels with varying wettability properties on the walls, but also accurately predicts the initial flow behavior, a frequently

overlooked aspect that is crucial for many practical applications where flow precision and predictability are essential.

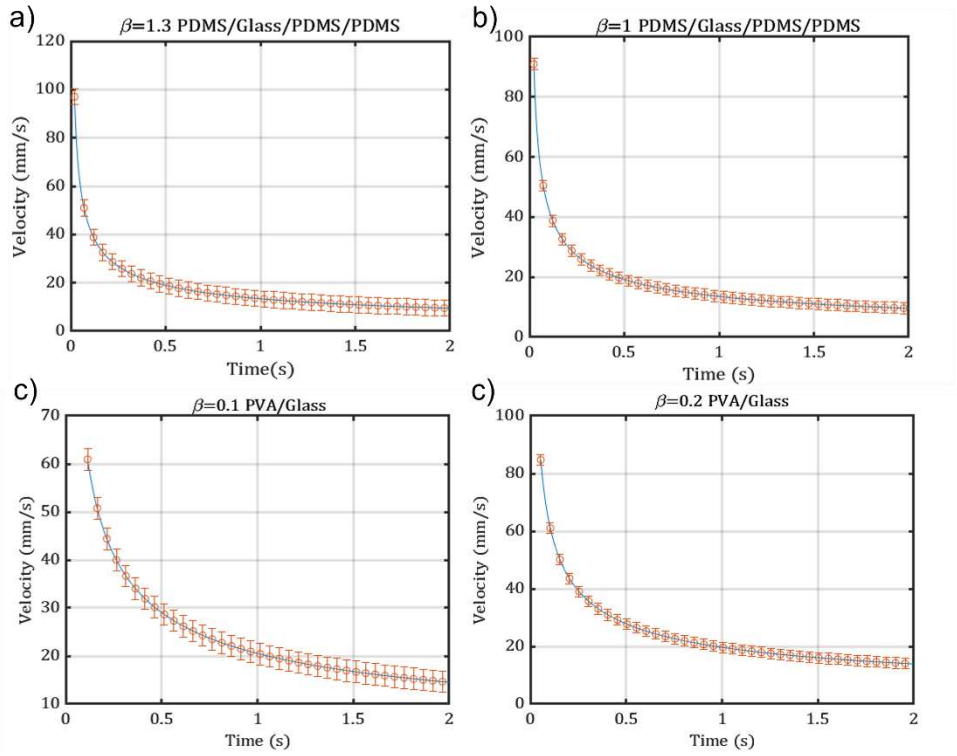

Figure 4.5. Fluid filling speed over time for rectangular microfluidic channels, including the relative errors, for rectangular microfluidic channels fabricated using: (a) PDMS/Glass/PDMS/PDMS and β = 1; (b) PDMS/Glass/PDMS/PDMS and β = 1.3; (c) PVA/Glass/Tape/Tape and β = 0.1; (d) PVA/Glass/Tape/Tape and β = 0.2.

4.5 Development and Characterization of a Flexible Microfluidic Capillary System with Integrated Plasmonic Sensor

After experimental validation of the analytical model, this technology was applied to achieve the ultimate research goal: developing a flexible capillary microsystem.

Flow tests were conducted on a fully flexible microdevice, fabricated using xurography (Appendix B), with a central chamber integrating a plasmonic sensor on PDMS, as described in Chapter 2. In a device designed in this way,

flow occurs without any external support. This microfluidic system is the result of meticulous design aimed at creating capillary-driven microfluidic pumps that optimize fluid transport. Figure 4.6 shows the device structure: a main channel leads to an elliptical area containing clusters of gold nanoparticles, followed by a network of parallel, narrower branching channels. This configuration allows for controlled resistance, creating a slower and more uniform flow, crucial in bioanalytical applications where specific fluid contact times with reactive surfaces are required, enhancing the precision and effectiveness of biochemical interactions [21].

Figure 4.6 illustrates an example of filling with red dye, where liquid movement is driven exclusively by capillary phenomena and the surface properties of the channel walls. It is evident how the liquid spreads uniformly through the channels, fully covering the sensor.

Figure 4.7 highlights the high flexibility of the sensor, showing images of the device during filling, even under significant stress, such as when highly curved. Functionalization of the plasmonic sensor follows the protocol outlined in Chapter 2, including surface treatments that optimize gold nanoparticle adhesion, enhancing plasmonic sensitivity and ensuring precise and reliable detection.

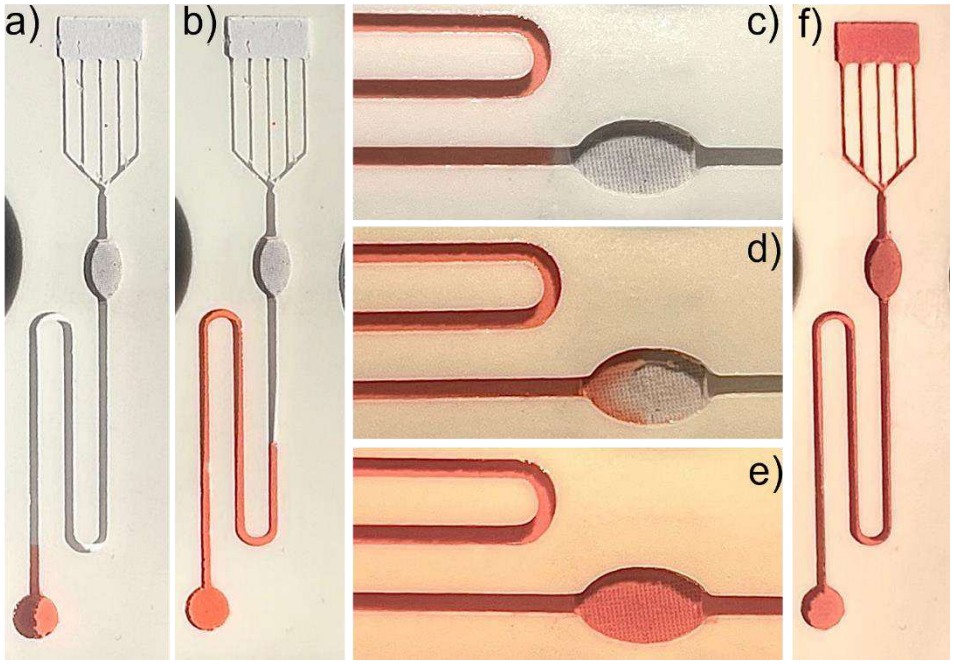

Figure 4.6 a-b) Start of flow within the fully flexible microfluidic system, activated solely by capillarity; c-e) progressive coverage of the entire plasmonic sensor positioned within the microfluidic chamber (gold nanoparticle cluster on PDMS); and f) end of flow and complete filling of the designed structure.

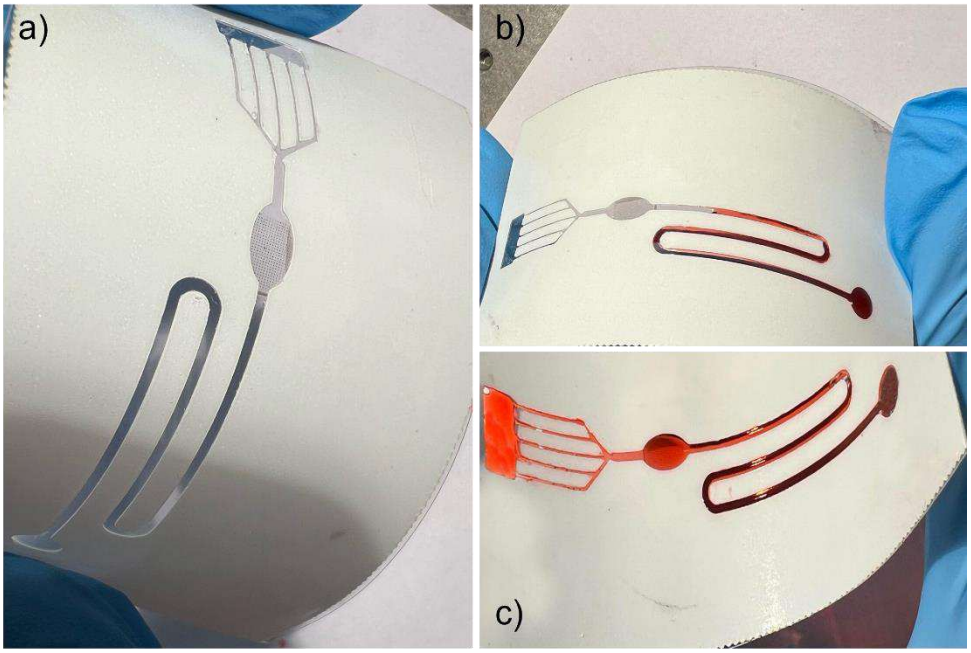

Figure 4.7 a) Fully flexible sensor integrated with the microfluidic pump and elliptical chamber containing AuNP clusters. b-c) Capillary-driven filling of the system, illustrating uniform liquid distribution without external support.

4.6 Conclusions

In this chapter, I examined the principles and practical applications of capillary systems, which leverage surface interactions to drive fluid movement without external energy sources. The chapter highlights the advantages of capillary microfluidics, such as energy efficiency, portability, and ease of use, particularly relevant for diagnostic devices where precise flow control can enhance sensitivity and efficiency.

Foundational work by researchers like White, Zimmermann, and Song was reviewed, each of whom contributed to understanding fluid dynamics in microchannels. This research focuses on an aspect previously unexplored: capillary flow in channels with walls of varying wettability. A general analytical model is proposed that considers the dynamic movement of the meniscus in three-dimensional channels. This model, validated experimentally, accurately describes capillary flow in systems fabricated through different techniques, such as soft lithography and xurography, predicting flow rate and meniscus displacement, even in channels with non-uniform wettability across surfaces. Experimental results confirm that our model captures the initial flow dynamics, a critical aspect for applications requiring precise and predictable fluid transport. The complete device was also developed, consisting of a flexible microfluidic system with a soft plasmonic sensor integrated within the microfluidic chamber. Flow tests were conducted while the system was fully bent, demonstrating that functionality remains consistent even under significant mechanical stress, such as high curvature. This approach confirmed the ability of the system to ensure stable capillary flow and reliable plasmonic detection even when deformed.

This work broadens the understanding of capillary flow in microfluidic systems, providing essential insights for designing advanced biomedical devices and microfluidic circuits with optimized flow dynamics. The next step will be to develop a compact, portable device, with a focus on illumination and signal detection—topics that will be further explored in the next chapter.

References

1. Xu, L., Wang, A., Li, X., & Oh, K. W. (2020). Passive micropumping in microfluidics for point-of-care testing. Biomicrofluidics, 14.

2. Elizalde, E., Urteaga, R., Koropecki, R. R., & Berli, C. L. (2014). Inverse problem of capillary filling. Physical Review Letters, 112, 134502.

3. Kolliopoulos, P., Jochem, K. S., Johnson, D., Suszynski, W. J., Francis, L. F., & Kumar, S. (2021). Capillary-flow dynamics in open rectangular microchannels. Journal of Fluid Mechanics, 911, A32.

4. Wang, X., Liu, Z., & Pang, Y. (2017). Concentration gradient generation methods based on microfluidic systems. RSC Advances, 7, 29966–29984.

5. Bayraktar, T., & Pidugu, S. B. (2006). Characterization of liquid flows in microfluidic systems. International Journal of Heat and Mass Transfer, 49, 815–824.

6. Gervais, L., & Delamarche, E. (2009). Toward one-step point-of-care immunodiagnostics using capillary-driven microfluidics and PDMS substrates. Lab on a Chip, 9, 3330–3337.

7. Safavieh, R., & Juncker, D. (2013). Capillarics: Pre-programmed, self-powered microfluidic circuits built from capillary elements. Lab on a Chip, 13, 4180–4189.

8. Olanrewaju, A., Beaugrand, M., Yafia, M., & Juncker, D. (2018). Capillary microfluidics in microchannels: From microfluidic networks to capillaric circuits. Lab on a Chip, 18, 2323–2347.

9. Safavieh, R., Tamayol, A., & Juncker, D. (2015). Serpentine and leading-edge capillary pumps for microfluidic capillary systems. Microfluidics and Nanofluidics, 18, 357–366.

10. Wang, Y., Zhao, J., Zhu, Y., Dong, S., Liu, Y., Sun, Y., Qian, L., Yang, W., & Cao, Z. (2021). Monolithic integration of nanorod arrays on microfluidic chips for fast and sensitive one-step immunoassays. Microsystems & Nanoengineering, 7, 65.

11. Gervais, L., Hitzbleck, M., & Delamarche, E. (2011). Capillary-driven multiparametric microfluidic chips for one-step immunoassays. Biosensors and Bioelectronics, 27, 64–70.
12. Hassan, S.-u., & Zhang, X. (2020). Design and fabrication of capillary-driven flow device for point-of-care diagnostics. Biosensors, 10, 39.
13. Tang, R., Yang, H., Choi, J. R., Gong, Y., You, M., Wen, T., Li, A., Li, X., Xu, B., Zhang, S., et al. (2017). Capillary blood for point-of-care testing. Critical Reviews in Clinical Laboratory Sciences, 54, 294–308.
14. Deyl, Z., Tagliaro, F., & Mikšík, I. (1994). Biomedical applications of capillary electrophoresis. Journal of Chromatography B: Biomedical Sciences and Applications, 656, 3–27.
15. Wang, G., Mishkinis, D., & Nikanpour, D. (2008). Capillary heat loop technology: Space applications and recent Canadian activities. Applied Thermal Engineering, 28, 284–303.
16. Juncker, D., Schmid, H., Drechsler, U., Wolf, H., Wolf, M., Michel, B., De Rooij, N., & Delamarche, E. (2002). Autonomous microfluidic capillary system. Analytical Chemistry, 74, 6139–6144.
17. Klug, K. E., Reynolds, K. A., & Yoon, J.-Y. (2018). A capillary flow dynamics-based sensing modality for direct environmental pathogen monitoring. Chemistry–A European Journal, 24, 6025–6029.
18. Li, X., Zhang, G., Wang, C., He, L., Xu, Y., Ma, R., & Yao, W. (2020). Water harvesting from soils by light-to-heat induced evaporation and capillary water migration. Applied Thermal Engineering, 175, 115417.
19. Rana, G., Sikarwar, B., Khandekar, S., & Panigrahi, P. (2014). Hydrodynamics of a confined meniscus in a square capillary tube at low capillary numbers. Frontiers in Heat Pipes (FHP), 5.
20. White, F. M., & Majdalani, J. (2006). Viscous fluid flow (Vol. 3). McGraw-Hill New York.
21. Zimmermann, M., Schmid, H., Hunziker, P., & Delamarche, E. (2007). Capillary pumps for autonomous capillary systems. Lab on a Chip, 7, 119–125.
22. Song, H., Wang, Y., & Pant, K. (2011). System-level simulation of liquid filling in microfluidic chips. Biomicrofluidics, 5.

23. Mohammed, M. I., & Desmulliez, M. P. Y. (2014). Characterization and theoretical analysis of rapidly prototyped capillary action autonomous microfluidic systems. Journal of Microelectromechanical Systems, 23, 1408–1416.

24. Man, P., Mastrangelo, C., Burns, M., & Burke, D. (1998). Microfabricated capillarity-driven stop valve and sample injector. In Proceedings MEMS 98. IEEE. Eleventh Annual International Workshop on Micro Electro Mechanical Systems. An Investigation of Micro Structures, Sensors, Actuators, Machines and Systems (Cat. No. 98CH36176) (pp. 45–50). IEEE.

25. Van Honschoten, J. W., Brunets, N., & Tas, N. R. (2010). Capillarity at the nanoscale. Chemical Society Reviews, 39, 1096–1114.

26. Bruus, H. (2007). Theoretical microfluidics (Vol. 18). Oxford University Press.

27. Van der Wijngaart, W. (2014). Capillary pumps with constant flow rate. Microfluidics and Nanofluidics, 16, 829–837

5
Conclusions and Future Prespective.

This research has addressed the development and optimization of microdevices for biochemical detection on flexible materials, with a particular focus on optical sensors and methodologies to achieve portable, cost-effective, and adaptable devices. The underlying idea was to transform initially rigid and complex devices into flexible platforms, reducing costs and enhancing operational autonomy through the integration of innovative fluid transport techniques.

Initially, the work focused on optimizing the functionalization of rigid plasmonic sensors, using a complex of gold and folic acid to create a surface that could selectively and reproducibly bind to specific biomarkers. The design and simulation of the microchannel geometry enabled a uniform flow distribution, reducing stagnant zones and improving the sensitivity of the sensor and specificity, even in the presence of interfering agents. Experimental measurements on the devices confirmed the effectiveness of the functionalization and the high uniformity of the coverage, highlighting the quality of the plasmonic substrate fabrication and the ability of the microfluidic system to ensure a constant and reproducible flow.

The next step was transferring this technology onto a flexible substrate, aimed at creating a plasmonic device directly integrated onto deformable materials. This approach required advanced fabrication techniques to obtain patterns of gold nanoparticles on PDMS. The choice of PDMS proved to be particularly effective due to its biocompatibility and stability, making it ideal for applications in flexible devices. To achieve precise control over the size and distribution of nanoparticle clusters, complementary techniques such as optical

lithography, PECVD, and autocatalytic chemical growth (electroless growth) were used.

The characterization of the device was completed with atomic force microscopy (AFM) measurements, which estabilished the conformity of the nanoparticle pattern and verified its structural stability on the deformable substrate. Additionally, mechanical tests were performed to assess the resistance and flexibility of the PDMS in the presence of nanoparticle clusters, ensuring that the device could maintain integrity and performance even under stress.

Experimental measurements through spectroscopy and fluorescence microscopy confirmed the results of the simulations, showing that the flexible structure could maintain high performance, amplify plasmonic signals, and effectively support biomarker detection even in dynamic conditions. These results demonstrate the ability the ability to operate in complex environments, opening new possibilities for using flexible sensors in advanced biomedical applications.

To make the device more portable and reduce its complexity, I focused on creating an autonomous system that eliminated the need for external pumps for fluid transport. At this stage, I leveraged capillarity to achieve autonomous and cost-effective fluid transport, optimizing the design of the device.

During the research period at the Vrije Universiteit Brussel (VUB), I focused on capillarity in cryo-EM applications, particularly on the spreading of droplets on cryogenic grids, an essential aspect for improving image quality. Through advanced fluid dynamic simulations and experiments on three different grid configurations—traditional, pillar-based, and microchannel—I analyzed and compared the effectiveness of each in spreading droplets.

Numerical analysis revealed that the pillar configuration introduced an enhanced capillary effect, promoting liquid expansion over a larger surface area, thereby increasing the contact area of sample with the grid. The pillars act as "capillary anchors," amplifying liquid adhesion and facilitating a more uniform spreading of droplets across the entire grid surface. This allows for better control of sample thickness, reducing concentration gradients and improving cryo-EM imaging quality.

The simulation results were promising, and the university has begun fabricating these optimized grids to conduct comparative experiments and imaging tests. Future studies will focus on a quantitative evaluation of droplet spreading capacity and uniformity, comparing traditional grids with those with pillars and microchannels to achieve higher-resolution cryo-EM images and optimal thickness. This approach offers new opportunities for improving sample preparation in cryo-EM and refining capillary control in microfluidic devices, expanding their potential in the biomedical field.

Back in the lab, I extended this approach to developing microfluidic devices capable of integrating capillary pumping systems specifically designed for biomedical applications. Creating capillary pumps required in-depth study and modeling of flow in microchannels made from materials with varying wettability. Since cost reduction was a priority, techniques for assembling heterogeneous materials were adopted, resulting in channels with variable wettability along the pathway.

To manage this complexity, it was essential to develop a general analytical model to predict capillary flow behavior under non-uniform conditions. In particular, I focused on channel sections with different wettability properties, studying the meniscus dynamics in the initial transient phase, an aspect previously unexplored in depth. The model integrates experimental results obtained from devices fabricated by soft lithography and xurography, cost-effective techniques that proved effective in creating heterogeneous microfluidic channels.

Simulations and experimental tests confirmed that the model accurately describes the meniscus advancement speed and capillary flow dynamics, even in the presence of walls with variable wettability. This model represents a fundamental contribution to designing advanced diagnostic devices, as it allows precise control of fluid transport, an essential feature for biomedical applications that require flow reliability and precision.

Finally, all the skills developed thus far have led to the creation of a flexible capillary microdevice with an integrated optical sensor on a fully flexible

material. Flow measurements, system filling, and sensor coverage were demonstrated, even under conditions of significant curvature.

Furthermore, preliminary tests have already been conducted to evaluate the functionality of the device when applied directly to the human body. A system capable of analyzing biological fluids, such as sweat, using a flexible plasmonic substrate integrated into a capillary-driven microfluidic circuit has been designed. This progress has been made possible thanks to the knowledge acquired and the design and fabrication phases described in this thesis.

The proposed device, as illustrated in the figure, consists of:

- An adhesive layer for attachment to the skin, featuring inlets that allow biological fluids to enter the device.
- A microfluidic circuit made of PDMS, with an active zone located in the ellipsoidal microfluidic chamber where the analysis takes place.
- A sealing layer made of PVA, which regulates and stabilizes the channels, facilitating capillary flow.

The figure illustrates two key aspects of the device's operation. First, it demonstrates the filling and rinsing of an analyte within the microfluidic circuit, simulating the functionalization of the substrate solely through capillarity, without the need for pumps or external components. This mechanism enables the uniform distribution of the solution within the system, ensuring proper substrate preparation for analysis. Additionally, the figure shows how, once applied to the skin, the device can facilitate the entry of a bodily fluid, such as sweat, through the designated inlets. The liquid, guided by capillary forces, spreads evenly throughout the microfluidic circuit and accumulates in the sensor's active zone, where the analysis occurs. This approach ensures a spontaneous and controlled flow of biological fluid, enhancing detection efficiency and system stability. Thanks to its ability to conform easily to the body surface, the device provides a flexible and comfortable solution for

advanced biosensing applications, with the potential for real-time, non-invasive monitoring.

.

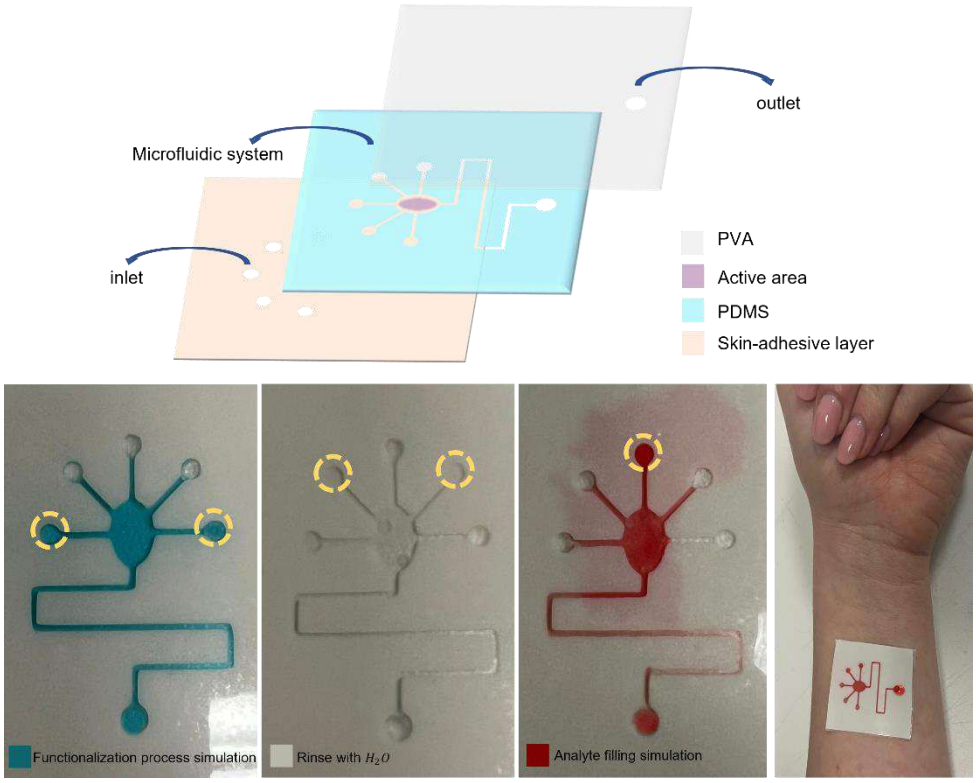

Figura 5.1 Schematic representation of a capillary-driven microfluidic circuit for optical sensing. Simulation process of functionalization with rinsing and direct application to the skin for the intake of a bodily fluid, enabling continuous analysis and monitoring.

For the next stage of device development, I will focus on further miniaturization and portability, specifically optimizing illumination and signal detection, which are crucial for achieving a flexible and autonomous biosensor. In a fully PDMS-based microfluidic device, emphasis will shift to an innovative approach to managing optical pathways. This strategy is inspired by previous studies that demonstrated potential of PDMS as an optical material, particularly in waveguide applications [1-3]. For instance, Martinček et al. [4] found that GHvariations in the refractive index at the interfaces between PDMS layers and other materials, initially viewed as defects, can guide light, forming natural optical pathways within PDMS.

Azmayesh-Fard et al. [5] expanded on the integration of optical waveguides in PDMS-based biochips with a method that bypasses the complexities of the "doctor-blading" technique. Doctor-blading involves spreading a thin layer of material using a blade, which requires precision to maintain uniformity and correct thickness. By adopting a simpler approach that precisely removes excess material, they created rectangular waveguides that minimized optical losses and improved efficiency. Later, Cai et al. [6] advanced this field by fabricating fully PDMS waveguides, using refractive index variations to create a core and cladding with different indices, thus simplifying the process and ensuring high compatibility with other microfluidic components.

Following these developments, our work plans to integrate diffractive elements created through holographic techniques (HOE), which are useful both for precisely channeling light and for reducing device size. A strategically positioned HOE will allow the light to be deflected at an angle greater than the critical angle of PDMS, achieving the total internal reflection (TIR) needed to confine the signal along the waveguide path.

TIR is an optical phenomenon that occurs when light passes from a medium with a higher refractive index (like PDMS) to one with a lower index (like air) at an angle that exceeds the so-called critical angle, calculable using Snell's law [7]. This law, expressed as:

$$n_1 sin\vartheta_1 = n_2 sin\vartheta_2$$

It relates the angles of incidence and refraction ϑ_1 and ϑ_2 and the refractive indices n_1 and n_2 of the two materials. When light strikes a surface at an angle above the critical angle:

$$\theta_c = \arcsin\left(\frac{n_2}{n_1}\right) \text{, where } n_1 > n_2,$$

it is completely reflected within the medium with the higher index. TIR is widely used in optical applications, such as optical fibers, where light remains confined within the core due to total reflection, allowing efficient signal transmission.

In this device, I will exploit this principle to create a waveguide in PDMS (Appendix C). Using an HOE, the light will be deflected at a sufficient angle to ensure total internal reflection, remaining confined and precisely directed

toward the optical sensor. In this case, the sensor will be represented by the flexible plasmonic gold nanoparticles on PDMS, which will interact with the confined light signal. Subsequently, a second HOE will direct the light toward a photodiode, completing the signal detection process.

The use of HOEs not only allows precise control of the light path but also eliminates the need for bulky or complex optical components, reducing the size of the device and simplifying its structure. With this system, I aim to create a device that, in addition to improving optical efficiency, is more robust and less susceptible to critical misalignments, thereby enhancing reliability and stability compared to traditional methods. A schematic of the device is shown in Figure 5, and an example of a practical application of this system is illustrated in Appendix C, in collaboration with TU Dublin.

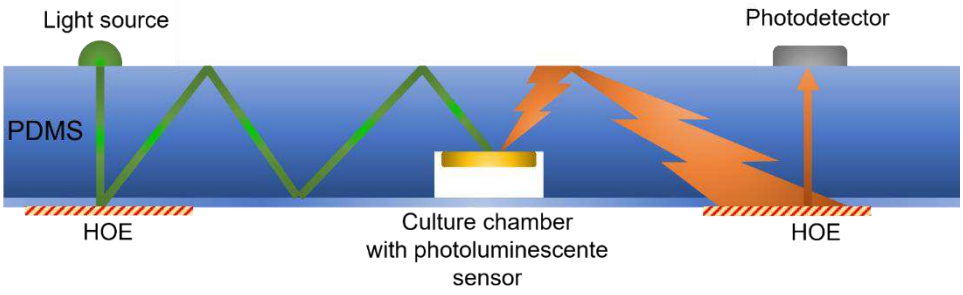

Figure 5.2 Sketch of HOE- based PDMS waveguide sensor.

The integration of this HOE technology represents a significant step toward the development of advanced biosensors capable of detecting weak signals with precision while maintaining a compact size. This advancement will increase not only the portability of device but also its versatility in the biomedical field, enabling a complete detection system in compact and flexible configurations. The next challenge will be to further refine the detection system by integrating more sensitive sensors and advanced optical signal processing strategies, so that the device can meet in situ biosensing requirements even in dynamic and complex environments.

In conclusion, this research has not only led to the creation of innovative diagnostic devices but has also contributed to consolidating a new understanding of capillarity phenomena applied to microfluidic biosensing. The results obtained provide a solid foundation for further developments in portable, low-cost diagnostics, paving the way for devices that can be used in situ and adapt to the dynamic challenges of biomedical applications.

The developed device represents an advancement compared to traditional plasmonic systems, which are typically based on rigid substrates such as glass, quartz, or silicon. These conventional materials limit applicability in contexts requiring flexibility, portability, or adaptability to curved surfaces. By employing PDMS, a flexible, transparent, biocompatible, and chemically stable material, the device overcomes these constraints, making it ideal for dynamic scenarios and portable applications.

A distinctive feature is the in situ synthesis of gold nanoparticles directly within the PDMS matrix. This approach resolves adhesion issues commonly associated with traditional methods and ensures a uniform distribution of nanoparticles, thereby enhancing the sensitivity of the device while simplifying the fabrication process. The reduction in production costs and improved scalability make this solution particularly promising for commercial applications.

The integration of capillary microfluidics further strengthens the innovation of the device. Fluid transport is entirely passive, requiring no external pumps or energy sources, thanks to the controlled wettability of PDMS surfaces. This ensures uniform and repeatable fluid flow, reducing system complexity and enhancing overall efficiency.

Overall, the developed device combines flexibility, sensitivity, and simplicity, opening new avenues for advanced biosensing and point-of-care diagnostics. The innovations introduced mark a significant step forward toward more accessible, portable, and adaptable diagnostic solutions tailored to real biomedical challenges. The following table summarizes the main focus areas, challenges addressed, and innovations introduced compared to the state of the art.

Focus Area	Advantages	Challenges	Innovations Compared to State-of-the-Art
Fully flexible device fabrication	Enables adaptability to curved and irregular surfaces	Mechanical stability under repeated deformation	Integration of plasmonic structures in PDMS using in-situ synthesis for a fully flexible biosensor
Fabrication techniques of plasmonic structure on soft material	Ensures uniform nanoparticle distribution	Challenges in adhesion and reproducibility on flexible substrates	Direct in-situ synthesis of gold nanoparticles within the PDMS network, avoiding transfer issues
Capillarity driven fluid transport	Energy-free operation and precise sample distribution	Limited control in highly variable flow conditions	Optimization of wettability in PDMS microchannels for consistent passive fluid motion
Signal detection	High sensitivity and real-time analysis	Susceptibility to environmental noise (e.g., lighting variations)	Robust plasmonic sensing integrated with flexible optical waveguides for enhanced performance

Table III

References

1. Cai, D. K., Neyer, A., Kuckuk, R., & Heise, H. M. (2008). Optical absorption in transparent PDMS materials applied for multimode waveguides fabrication. Optical Materials, 30(7), 1157-1161.

2. Valouch, S., Sieber, H., Kettlitz, S., Eschenbaum, C., Hollenbach, U., & Lemmer, U. (2012). Direct fabrication of PDMS waveguides via low-cost DUV irradiation for optical sensing. Optics Express, 20(27), 28855-28861.

3. Fleger, M., & Neyer, A. (2006). PDMS microfluidic chip with integrated waveguides for optical detection. Microelectronic Engineering, 83(4-9), 1291-1293.

4. Turek, I., Tarjányi, N., Martinček, I., & Káčik, D. (2014). Effect of mechanical stress on optical properties of polydimethylsiloxane. Optical Materials, 36(5), 965-970.

5. Azmayesh-Fard, S. M., Flaim, E., & McMullin, J. N. (2010). PDMS biochips with integrated waveguides. Journal of Micromechanics and Microengineering, 20(8), 087002.

6. Cai, Z., Qiu, W., Shao, G., & Wang, W. (2013). A new fabrication method for all-PDMS waveguides. Sensors and Actuators A: Physical, 204, 44-47.

7. Jackson, J. D. (1999). Classical Electrodynamics.

APPENDIX A

Numerical Simulation for Fluids Dynamic Design of Microfluidic Devices

In previous chapters, each device created was described as having undergone a detailed design phase using COMSOL Multiphysics software. In this section, I delve into the basics of simulation and the Finite Element Method (FEM), thoroughly exploring the physical models studied throughout my three years of research. To model the flow within microdevices, I used the "Microfluidics" module with the "Laminar Flow" physics, ideal for representing laminar flow behavior in microchannels. To analyze the filling and emptying processes of the devices, the "Transport of Diluted Species" module was employed, allowing observation of the spreading and mixing of chemical species within the microdevices. Special attention was dedicated to studying capillary phenomena, utilizing the Level Set physics to track the dynamic interface between two phases (liquid and gas, or between two immiscible liquids). This tool enables observation of how one phase influences the other and assesses the effects of wettability. Additionally, this chapter provides a comparison between the Level Set and Phase Field methods. While both are based on similar principles, they are applied in different contexts depending on specific modeling needs.

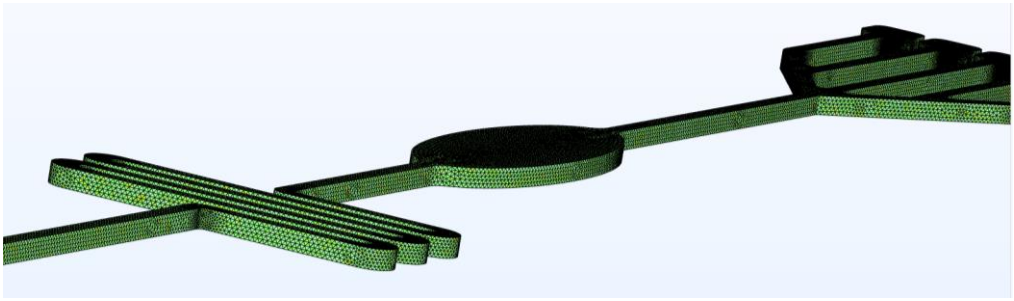

Figure A. Example of meshing a microfluidic structure in COMSOL Multiphysics

A.1 Introduction to Numerical Simulation and the Finite Element Method (FEM)

In experimental studies, it is essential to start from a solid theoretical foundation; however, finding analytical solutions to complex problems is often impossible. For this reason, numerical simulations are employed, allowing for the approximation of physical theories and providing solutions that closely mirror reality. Among the main methods of numerical simulation are FDTD (Finite Difference Time Domain), BEM (Boundary Element Method), and FEM (Finite Element Method). In this work, I focus on simulations based on FEM.

The Finite Element Method (FEM) relies on the discretization of a domain, dividing the continuous domain into a mesh composed of small subregions, called elements. This approach allows us to solve a system of equations that describes the physical behavior within each element, providing an approximation of the governing equations. Through FEM, complex partial differential equations are reduced to a system of linear or nonlinear equations, enabling an accurate representation of the boundaries of complex domains.

Solving a problem using the Finite Element Method involves several fundamental steps:

1. Domain Discretization: The domain is divided into non-overlapping elements of various shapes, such as triangles or quadrilaterals. Each element is defined by a certain number of nodes.
2. Selection of Interpolation Functions: An interpolation function is chosen to represent the variation of the field variable over each element.
3. Formulation of Element Equations.
4. Assembly of Element Equations to obtain a system of simultaneous equations.
5. Solution of the System of Equations.

In this thesis, particular attention is dedicated to the application of numerical simulations to study fluid flow behavior using the FEM simulation software COMSOL Multiphysics.

A.2 COMSOL Multiphysics

COMSOL Multiphysics is a powerful tool for solving partial differential equations (PDEs) using the Finite Element Method (FEM). The base version of COMSOL offers numerous add-on modules that expand the capabilities of the software across various application fields, including AC/DC, Acoustics, Chemical Engineering, Earth Sciences, Heat Transfer, MEMS (MicroElectroMechanical Systems), RF (Radio Frequency), and Structural Mechanics. The term *multiphysics* refers to simulations that involve multiple physical models or simultaneous physical phenomena, enabling applications where various physical-chemical mechanisms are present.

The COMSOL Microfluidics Module is used to understand, predict, and design microfluidic systems. The physics interfaces in this module allow users to set up a simulation by defining partial or ordinary differential equations along with appropriate initial and boundary conditions. Each added feature within the interface represents a term or condition in the underlying equations. In this work, the Microfluidics Module and its associated physics have been explored in detail.

A.3 Laminar Flow in COMSOL Multiphysics

The Laminar Flow interface in COMSOL Multiphysics is an advanced tool for simulating and analyzing laminar flow behavior across a wide range of applications, from simple to complex geometries. This physics has been instrumental at every stage of designing the microdevices studied over the years, proving essential in developing accurate and optimized solutions. In microfluidics, due to the small dimensions of these systems, flow typically occurs in laminar conditions, where inertial forces are negligible. Laminar flow is characterized by a smooth, orderly fluid motion, with particles moving along

parallel lines without mixing or creating vortices. This flow regime occurs when the Reynolds number Re is sufficiently low to make viscous forces dominant over inertial forces. The Reynolds number is a dimensionless parameter, defined as:

$$Re = \frac{\rho \boldsymbol{u} L}{\mu} \quad (1)$$

where:

- ρ is the fluid density,
- $\boldsymbol{u}$ is the characteristic velocity of the fluid,
- L is the characteristic length of the system (such as the diameter of a conduit),
- μ is the dynamic viscosity of the fluid.

The Reynolds number is fundamental for classifying the flow type: for Re values below approximately 2000 in duct flows, the flow remains laminar. Above this threshold, fluid disturbances tend to grow, leading to a transition to turbulent flow, characterized by chaotic and swirling motion.

The equations solved by the Laminar Flow interface are the Navier-Stokes equations. The Navier-Stokes equations are essential for studying and analyzing fluid flow, as they enable accurate predictions of fluid behavior during interactions. These time-dependent equations describe the conservation of mass and momentum in fluid flow, making them essential for modeling and simulating fluid behavior across a wide range of applications, from engineering to biological fields, and are formulated as follows:

$$\nabla u = 0 \quad (2)$$

$$\rho\left(\frac{\partial u}{\partial t} + u\nabla u\right) = \nabla[-\rho I + \mu\nabla u + \nabla u^T] + \rho g + F_{st} \quad (3)$$

- t is the time

- p is the water pressure
- g is the gravitational acceleration
- F_{st} is the surface tension force
- I is the identity matrix

The Laminar Flow interface also enables the modeling of weakly compressible and compressible flows. A fluid is considered incompressible when its density remains constant despite changes in pressure and temperature, simplifying calculations. In compressible flow models, density varies as a function of pressure and/or temperature, which is necessary to describe phenomena where the fluid velocity is comparable to the speed of sound, such as in high Mach number flows.

The Mach number, M_a, represents the ratio between the flow velocity and the speed of sound in the fluid, defined as:

$$M_a = \frac{\boldsymbol{u}}{c} \tag{4}$$

where

- c is the speed of sound in the fluid.

For Mach numbers below 0.3, the flow can be considered low-Mach compressible, as density variations are limited and compressible effects are moderate. When M_a exceeds this threshold, the flow becomes transonic and then supersonic, requiring more complex models for accurate description.
A fundamental concept in fluid dynamics is Stokes Flow, which refers to flows where inertial terms in the Navier-Stokes equations are negligible compared to viscous terms, typically when Re < 1. Under these conditions, the fluid behaves as highly viscous, and velocity gradients are minimal. In this case, the Navier-Stokes equation simplifies to: is the speed of sound in the fluid.

For Mach numbers below 0.3, the flow can be considered low-Mach compressible, as density variations are limited and compressible effects are moderate. When M_a exceeds this threshold, the flow becomes transonic and then supersonic, requiring more complex models for accurate description.
A fundamental concept in fluid dynamics is Stokes Flow, which refers to flows where inertial terms in the Navier-Stokes equations are negligible compared to viscous terms, typically when Re < 1. Under these conditions, the fluid behaves as highly viscous, and velocity gradients are minimal. In this case, the Navier-Stokes equation simplifies to:

$$0 = -\nabla\rho + \mu\nabla^2 u + f \tag{5}$$

This simplified form, known as the Stokes equation, is used to model slow flows, such as fluid movement in porous media or in microfluidic systems.
When using these settings in the Laminar Flow interface, it is possible to define whether the fluid is compressible, weakly compressible, or incompressible based on the expected behavior of density and velocity.
Finally, the Laminar Flow interface also offers options for modeling flows in narrow channels, as is often the case in microfluidic applications. The Use Shallow Channel Approximation option accounts for the resistance exerted by parallel walls in channels with very thin rectangular cross-sections relative to their width. This approach introduces a resistance term that reduces the velocity field near the walls, improving simulation accuracy without requiring complex three-dimensional models.

The Laminar Flow interface in COMSOL is capable of simulating a wide range of fluid dynamics phenomena, adapting to various flow regimes and allowing detailed analysis of fluid-structure interactions, ensuring accuracy and versatility in multiphysics simulations.

A.4 Transport of Diluted Species in COMSOL Multiphysics

The Transport of Diluted Species interface in COMSOL Multiphysics is used to model and simulate the transport of diluted chemical species in a solvent, accounting for diffusion, convection, and chemical reaction mechanisms. This module is essential for analyzing how the concentration of one or more chemical species varies over time and space within systems under complex environmental conditions, predicting phenomena such as molecular diffusion, mixing in microchannels, chemical reactions between multiple solutes, and species separation in laboratory devices.

In particular, this method has been widely used to simulate different species within a microfluidic system, allowing for the evaluation of filling and emptying times for chemical species through concentration analysis. This process is crucial for designing optimized microdevices in terms of flow rates, time efficiency, and geometry to ensure uniform filling and effective rinsing. An optimal design, as discussed in previous projects, enables the reuse of devices without chemical residue, ensuring complete cleaning and reusability.

The transport of diluted species is governed by Fick's Law of diffusion and the convection-diffusion equation, which also considers convective transport due to fluid movement. The general equation that describes the behavior of diluted species is as follows:

$$\frac{\partial c}{\partial t} + \nabla \cdot (\mathrm{C}\mathbf{u}) = \nabla \cdot (\mathrm{D}\nabla \mathrm{C}) + \mathrm{R} \tag{6}$$

where:

- C is the concentration of the species $\frac{mol}{m^3}$
- $\mathbf{u}$ is the fluid velocity vector $\frac{m}{s}$,
- D is the diffusion coefficient of the species $\frac{m^2}{s}$
- R is the source or reaction term $\frac{mol}{m^2 s}$

This equation represents the mass balance for the chemical species, incorporating three primary transport mechanisms:

- Diffusion: the species moves from areas of higher concentration to lower concentration, following the concentration gradient.
- Convection: the species is transported by the moving fluid, which carries its particles along its path.
- Chemical Reaction: species can react with each other, producing or consuming substances based on defined kinetic equations.

The Transport of Diluted Species interface allows each species to be defined with specific properties, such as diffusion coefficient and reactivity, and enables detailed configuration of initial and boundary conditions for each domain and study case.

When using the Transport of Diluted Species interface, different solution modes can be selected based on problem complexity and physical phenomena involved. The main modes include:

- Pure Diffusion: considers only the diffusion process, described by Fick's First Law, which expresses mass flux as proportional to the concentration gradient:

$$\mathbf{J} = -\mathrm{D}\nabla\mathrm{C} \tag{7}$$

where **J** is the diffusion flux $\frac{mol}{s \cdot m^2}$. This approach is useful for analyzing systems where the fluid is stationary or convective transport is negligible.

- Convection and Diffusion: the chemical species is transported both by diffusion and by fluid movement (convection). In this case, the transport equation becomes:

$$\frac{\partial c}{\partial t} + \mathrm{u} \cdot \nabla\mathrm{C} = \nabla \cdot (\mathrm{D}\nabla\mathrm{C}) + \mathrm{R} \tag{8}$$

This model is ideal for microfluidic systems or for studying the transport of chemical substances within lab-on-a-chip devices, where fluid movement significantly impacts species distribution.

- Reaction-Convection-Diffusion: this mode also accounts for chemical reactions between species within the system. The term R in the equation represents the rate of production or consumption of the species, based on user-defined kinetic laws. For example, for a first-order chemical reaction A → B the term R can be expressed as:

$$rR = -kc_A \quad (9)$$

where k is the reaction rate constant and c_A is the concentration of reactant A.

When the Transport of Diluted Species interface is added to the Model Builder in COMSOL, several predefined nodes are automatically generated, allowing for detailed configuration of the properties and conditions of the problem. For instance, the Transport Properties node enables the definition of the diffusion coefficient and fluid velocity, if present; the Reaction node allows for setting up any chemical reactions that affect species concentration, while Initial Values lets you specify initial concentrations within the domain. Finally, Boundary Conditions allows for configuring inlet and outlet flows, impermeable walls, or symmetry conditions.

Each node can be configured individually to adapt to specific boundary conditions: for example, you can set an inlet flow with a defined concentration and an outlet with neutral diffusion, where the concentration gradient is zero along the normal.

The Transport of Diluted Species interface also includes advanced options for modeling complex phenomena, such as adsorption and desorption on solid

surfaces, electrochemical reactions where species transport is coupled with electric current, and transport in porous media, accounting for interactions between the fluid phase and the porous material.

A.5 Level Set Method in COMSOL

The Level Set method is an Eulerian approach for tracking interfaces in multiphase flow problems on a fixed grid. In this work, it has been extensively explored to study capillarity phenomena, particularly to analyze the dynamic behavior of a water droplet impacting a dry solid substrate and to track its changes. In this context, the two phases considered are air and water. The numerical analysis enabled the prediction of the final shape of the droplet and the evolution of the velocity field during spreading on a surface with specific wettability, using the Navier-Stokes equations (eq. 2-3).

The conservative Level Set method, employed in this study for precise and reliable tracking of the interface between phases, ensures good conservation of mass during the simulation process. It is based on the definition of a scalar function called the *Level Set function*, which represents the position of the phase interface. The Level Set function is defined as the Euclidean distance from the surface of interest.

During the simulation, the Level Set function is propagated on the fixed grid using advection equations. Additionally, the Level Set function is updated to maintain its definition of the surface of interest.

In the Level Set method, the interface is captured by a level set function represented by a smoothed Heaviside function. The level set function changes gradually along the interface from 0 to 1, where φ equals 0 in the air and 1 in the liquid, and the interface is defined by the $\varphi = 0.5$ isocontour. The interface moves with the fluid velocity, u, at the interface. The following equation describes the convection of the reinitialized level set function:

$$\rho\left(\frac{\partial \phi}{\partial t} + \nabla(\phi u)\right) = \gamma\left[\varepsilon\nabla\cdot\nabla\phi - \nabla\cdot\left(\phi(1-\phi)\frac{\nabla\phi}{|\nabla\phi|}\right)\right] \quad (10)$$

where ε is a parameter that determines the thickness of the transition layer and should be taken as half of the typical mesh size in the region crossed by the droplet. The parameter γ determines the amount of stabilization reinitialization and must be carefully adjusted for each specific problem. If γ is too small, the interface thickness may not remain constant, and φ oscillations due to numerical instabilities may occur. On the other hand, a γ that is too large may result in an incorrect interface. A suitable value for γ is the maximum magnitude occurring within the velocity range.

The level set function is used to smooth density and viscosity jumps across the interface using the definitions:

$$\rho = \rho_a + (\rho_l - \rho_a)\phi \quad (11)$$

$$\mu = \mu_a + (\mu_l - \mu_a)\phi \quad (12)$$

- $\boldsymbol{\varrho a}$ air density
- $\boldsymbol{\varrho l}$ water density
- $\boldsymbol{\mu a}$ dynamic air viscosities
- $\boldsymbol{\mu l}$ dynamic water viscosities

The surface tension force is calculated as:

$$F_{st} = \nabla\mathrm{T} = \nabla\cdot[(\sigma(\mathrm{I} - nn^T))\delta] \quad (13)$$

- $\boldsymbol{I}$ identity matrix
- $\boldsymbol{n}$ is the normal at the interface
- **σ** surface tension
- **δ** is the Dirac delta function that is non-zero only at the fluid interface.

The normal at the interface is calculated as:

$$n = \frac{\nabla \phi}{|\nabla \phi|} \tag{14}$$

In our study, the wall on which the droplet impacts and spreads was considered as a wetted wall, with a boundary condition imposing the normal component of velocity at the wall to be zero and introducing a wall friction force, where η represents the fluid viscosity and β represents the wall length needed for the velocity profile to converge. For numerical calculations, it is common to choose β equal to the mesh element size.

$$un_{wall} = 0 \tag{15}$$

$$K_{nt} = -\frac{\eta}{\beta} u \tag{16}$$

The Wetted Wall function is particularly suitable for walls in contact with the fluid-fluid interface, as it allows the interface to move along the wall. This means that the Wetted Wall condition is an ideal solution for modeling complex flows where walls interact with the fluid interface.

The contact angle, defined as the angle between the fluid interface and the wall, can be calculated directly or using the Young's equation, which considers the components of forces in the surface plane. It is important to note that the contact angle θw does not apply to boundaries adjacent to porous domains. This must be taken into account when modeling complex systems where the fluid interacts with porous surfaces.

$$\sigma \cos(\vartheta_w) + \gamma_{s1} = \gamma_{s2} \tag{3}$$

Where γs1 is the surface energy density at the interface between fluid 1 and the solid (wall), and γs2 is the surface energy density at the interface between fluid

2 and the solid (wall). The contact angle θ influences the wetted diameter d and the height h of the droplets during their spreading process.

A.6 Phase Field in COMSOL Multiphysics

The phase field is another numerical method used to simulate the interface between two phases, such as between a liquid and a gas or between two immiscible liquids, within a continuous domain. In this approach, the interface is not represented by a sharp boundary but rather by a transition region where fluid properties, such as density and viscosity, change gradually. The phase function, ϕ is a continuous variable ranging from -1 to 1, where -1 represents one phase (e.g., liquid) and 1 represents the other phase (e.g., gas). The separation surface between the phases, or the interface, is given by the isocurve $\phi = 0$.

The distinctive aspect of the Phase Field method is how it handles the stability and shape of the interface: it minimizes the free energy of the system, a process that stabilizes the surface and ensures a gradual and uniform transition between phases. This minimization is achieved by adding higher-order terms to the phase function equation, which act to keep the interface compact even in the presence of complex deformations and movements. In this way, the Phase Field method provides a continuous and stable description of the interface, making it suitable for situations such as simulations of small-scale laminar flows where surface tension is a factor.

This approach differs from the Level Set method, which represents the interface with a function ranging from 0 to 1 and requires additional corrective terms to maintain interface stability, especially in the presence of deformations or changes in geometry.

For studying capillarity, the choice between the Level Set and Phase Field methods was made based on the specific requirements of each situation. The Level Set method was used to simulate the spreading of a droplet on a substrate. This approach is ideal for tracking interface deformation starting from a well-defined domain, such as a single droplet. The ability of the Level Set method to accurately represent interface curvature was essential for analyzing how the droplet spreads on the substrate and how wettability properties influence this process.

In contrast, for simulating capillary flow within a microfluidic channel, the Phase Field method was preferred. This method is more suitable in situations where the interface forms and evolves within complex geometries, such as a microfluidic channel, where the flow is driven solely by capillarity. Due to its numerical stability and gradual interface handling, the Phase Field method allowed for representing fluid movement within the channel without requiring a rigid starting geometry, offering a continuous and uniform description of the phase transition.

References

1. Griebel M., T. Dornseifer, and T. Neunhoeffer, Numerical Simulation in Fluid Dynamics: A Practical Introduction, Society for Industrial and Applied Mathematics (SIAM), 1998.

2. Zienkiewicz O.C., Taylor R. L., The Finite Element Method. Volume 1: The Basis, Fifth Edition, Butterworth Heinemann, 2000.

3. Clough R.W., "The Finite Element Analysis in Plane Stress Analysis," Proceedings of the 2nd ASCE Conference on Electronic Computation, Pittsburgh, PA, September 1960.

4. Zienkiewicz O.C. and Cheung K., "Finite Elements in the Solution of Field Problems," Engineer, 200, pp. 507–510, 1965.

5. Lewis R.W., Nithiarasu P., Seetharamu K.N., Fundamentals of the Finite Element Method for Heat and Fluid Flow, John Wiley & Sons, Ltd, 2004.

6. Pryor R. W., Multiphysics Modeling Using COMSOL: A First Principles Approach, Jones and Bartlett Publishers, 2000.

7. Zimmerman W. B. J., COMSOL Process Modeling and Simulation with Finite Element Methods, World Scientific Publishing Co. Pte. Ltd., 2004.

8. COMSOL Multiphysics Documentation: The Microfluidics Module.

9. Nam-Trung Nguyen and Steven T. Wereley, Fundamentals and Applications in Microfluidics, ARTECH HOUSE, INC., 2006.

10. Kleinstreuer C., Modern Fluid Dynamics: Basic Theory and Applications in Macro- and Micro-Fluidics, Springer, 2010.

11. COMSOL Multiphysics Documentation: Laminar Flow, The Particle Tracing Module, The Level Set Method, and Phase Field.

APPENDIX B
Numeric Laboratory Manufactoring Processes

In previous chapters, I explored the fabrication methods for microdevices used in biomedical applications. This section focuses on the manufacturing processes conducted in specialized laboratories, such as the clean room at the Institute of Applied Sciences and Intelligent Systems (ISASI) in Naples, which is equipped with advanced tools for micro- and nanofabrication. This state-of-the-art facility enables the production of devices with high precision and control, utilizing specialized equipment for deposition, etching, and lithography at the micro- and nanoscale.

Alongside these advanced technologies, this section also examines more accessible, low-cost fabrication techniques that can produce equally efficient devices with more economical materials and methods. These "low-cost" approaches allow for the development of biomedical devices without requiring complex infrastructure, making them suitable for rapid prototyping or large-scale applications in resource-limited settings.

Figure B. ISASI's group Clean room

B.1 μ-Fabrication

Microscale microfabrication is the realm of the "small big": it covers sizes between 0.1 and 500 micrometers, allowing the creation of incredibly precise tiny structures. To put it into perspective, these are dimensions up to a thousand times thinner than a human hair. Microfabrication techniques fall mainly into two categories: hard and soft technologies, each with distinct materials and methods.

Hard technologies use rigid materials like glass and silicon, known for their resilience, precision, and stability—ideal for applications where every micrometer matters. Key techniques include etching, lithography, and deposition, all of which operate on scales between 0.2 and 500 micrometers, creating complex microfluidic devices with remarkable accuracy. Picture micro-channels linked to tiny evaporated electrodes that are accessible from the outside for precise measurements or micrometric manipulations.

Silicon is the undisputed leader in this category, but it has limitations. For example, its optical opacity hinders applications that require transparency, and its high cost and low biocompatibility limit its use with biological samples like cells and proteins. While glass offers a viable alternative, it requires complex processing that slows down large-scale applications.

This is where soft technologies come in, relying on flexible, moldable materials like elastomers and plastics. A leading material in this field is PDMS, a soft, transparent, and biocompatible polymer that has revolutionized microfabrication. Imagine having a mold (like a cookie cutter) that defines the desired pattern: using this mold, PDMS can be quickly shaped to create precise, custom microstructures for microfluidic designs.

Soft techniques are ideal for applications that require flexible, biocompatible devices. In biological and chemical fields, for example, they allow for the creation of microchannels that mimic the human tissue environment, enabling in vitro analysis of cells or biomolecules on a micrometer scale.

To address silicon and glass limitations, elastomeric micromolding was developed at Bell Labs in the 1970s, introducing a new way to create microstructures by molding elastomeric materials onto lithographic molds. Japanese researchers advanced these techniques in the 1980s by developing soft lithography methods, opening new avenues for affordable microdevice production. Through embossing and molding, increasingly complex and accessible microfluidic applications were developed.

In the 1990s, George Whitesides' team took these innovations further by introducing PDMS in soft lithography. This breakthrough made microfabrication more accessible, affordable, and faster, allowing researchers and companies to easily create microfluidic devices for biomedical and chemical applications. With its transparency, PDMS is perfect for microscopy and optical analysis, and its flexibility makes it ideal for devices that gently interact with biological tissues.

B.2 Rapid Prototyping

The Soft Lithography Process

The soft lithography process begins with applying a layer of photoresist onto a substrate, like silicon or glass, using a spin-coater that distributes the photoresist evenly through high-speed rotation [1-10]. Next, the desired pattern is "printed" by exposing the photoresist to a light source through a mask containing the design. This light, typically from a mercury vapor lamp, passes through the mask and projects a pattern of light and dark areas onto the photoresist, transferring the image of the mask onto it.
This step is known as pattern transfer. Once the photoresist takes the desired shape, unwanted sections are removed, and the microstructure is molded.

The photoresist is applied as a thin layer on a solid substrate, such as silicon or glass, through spin-coating. The resulting film thickness is uniform and follows this empirical relationship:

$$h = kC(\frac{\mu}{\omega^2})^{\frac{1}{3}}$$

where:

- h represents the film thickness,
- C is the initial concentration of polymers in solution,
- k is a characteristic constant of the process,
- ω is the angular rotation speed.

The type of photoresist used determines the final pattern result:

1. Positive resist: illuminated areas become soluble in a specific solvent, while non-illuminated areas remain insoluble.
2. Negative resist: illuminated areas become insoluble, while non-illuminated areas can be removed with the same solvent.

One of the most important advancements in microfabrication was the introduction of SU-8 photoresist by IBM, an extremely useful photosensitive resin for creating microstructures. This photoresist revolutionized microfluidic device fabrication due to its high photosensitivity and ability to be deposited in very thick layers, even up to tens of micrometers. This feature makes it ideal for creating high aspect ratio structures, where the height of the structure is significantly greater than the width. In our work, SU-8 was chosen as the photoresist for fabricating microfluidic channels in microsystems, due to its ability to form deep, well-defined channels essential for applications that require controlled fluid flows on a micrometer scale.

To transfer the desired patterns onto the SU-8 photoresist, I use two main techniques: mask aligner and laser writer, each offering specific advantages for different fabrication needs.

1. Mask Aligner: This technique uses a mask containing the pattern to be transferred and a UV light source that passes through the mask to etch the

pattern onto SU-8. The mask aligner enables high-resolution patterning, even on relatively large surfaces, due to its precision in positioning and the uniformity of UV light. This method is ideal for mass production or large patterns that require high repeatability.

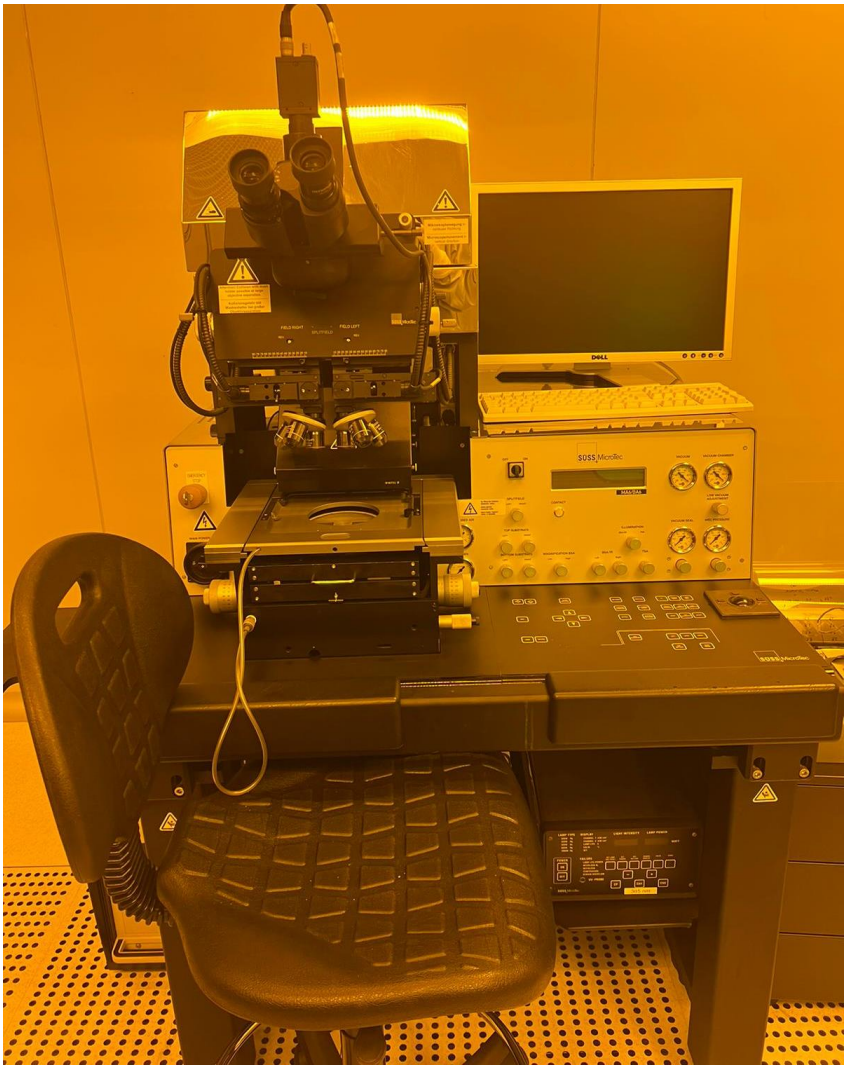

Figure B.1.Mask Aligner

2. Laser Writer: Unlike the mask aligner, this technique does not require a physical mask. The laser writer creates the pattern directly onto the SU-8 photoresist using a focused laser beam, which "writes" the design pixel by pixel. It is a direct writing technique particularly suited for rapid prototyping or for creating complex structures on small areas, as it allows great flexibility in pattern

design. Its versatility makes the laser writer perfect for iterative design and for creating customized structures.

Figure B.1. Laser writer

Replica Molding

After creating the SU-8 lithographic master, the process moves to creating microfluidic channels in PDMS, an elastomeric polymer widely used in microfluidics for its flexibility, transparency, and biocompatibility. PDMS is supplied as an uncrosslinked pre-polymer, and to initiate the cross-linking process, it must be mixed with a cross-linking agent in a typical 10:1 ratio. This ratio is essential: a correct mixture allows for uniform solidification and a stable elastomeric structure. During cross-linking, silicon hydride groups in the cross-linking agent react with vinyl groups present in the PDMS base, forming a crosslinked structure that gives the material its elastic properties.

Once the PDMS mixture is prepared, it is poured over the SU-8 master. The PDMS conforms perfectly to the micro-patterns on the master, and once solidified, an exact replica of the channels and structures is obtained. This replication process is called stamping and represents a cost-effective and efficient method to create multiple copies of the original design.
For practical use of microfluidic devices, it is necessary to include access holes and reagent reservoirs. These can be integrated in two main ways:

- Adding pins to the master: During the creation of the master, pins can be placed at points where access holes are desired, so that these holes are already present in the PDMS replica.
- Manual perforation: Once the PDMS has solidified, holes can be manually created using a small punch, a technique particularly useful for customized applications or prototypes.

Once completed, the PDMS replica already includes three of the four walls necessary to form a closed channel. The fourth wall is achieved by sealing the replica onto a flat surface, which can be another layer of PDMS or a glass slide. Sealing PDMS devices is a critical step that can be done in two ways:

1. Reversible sealing: Achieved by simply placing the PDMS surface against a smooth surface, such as a glass slide. This type of sealing is temporary and allows the device to be removed without damage, making it suitable for short-term experiments or preliminary tests.

2. Irreversible sealing: Achieved by treating the PDMS surface with an oxygen plasma. This treatment makes the PDMS surface more reactive, promoting covalent bonding with a complementary surface, such as another layer of PDMS or a glass slide, and ensuring a permanent seal.

In our laboratories, irreversible PDMS sealing is performed using the Reactive Ion Etching technique (RIE), which involves generating an oxygen plasma in a vacuum chamber. During this process, a high-frequency electric field

accelerates oxygen ions, creating a highly reactive plasma composed of oxygen radicals and ions. These species interact with the PDMS surface, removing organic contaminants and activating hydroxyl (-OH) groups, which promote covalent bonding between coupled surfaces. Once two PDMS surfaces treated with plasma are placed together, the -OH groups react with each other, forming stable siloxane (Si–O–Si) bonds, thus ensuring a permanent seal.

Plasma treatment requires specific parameters to be effective and achieve good adhesion. Typical parameters are:

- Gas: Oxygen (O2)
- Flow rate: 100 sccm (standard cubic centimeters per minute)
- Pressure: 0.13 mbar
- RF Power: 100 W
- Treatment time: 5 minutes

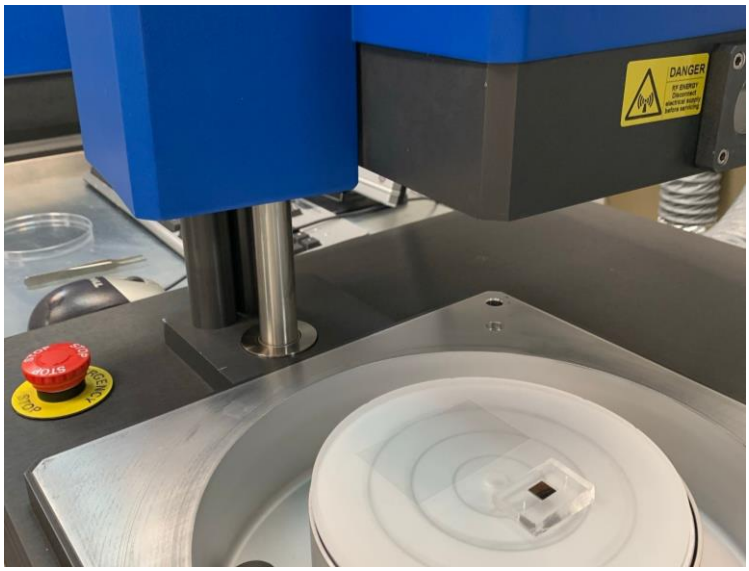

Figure B.3. Reactive Ion Etching technique (RIE) machine

This treatment temporarily makes the PDMS surface more hydrophilic, facilitating the filling of microfluidic channels with fluids. However, treated surfaces tend to revert to hydrophobic over time, so it is essential to couple the surfaces immediately after treatment.

Xurography is an innovative fabrication technique for microfluidic devices, enabling the rapid and straightforward creation of two-dimensional microstructures using a cutting plotter. This method is based on a computer-controlled cutting approach, employing specialized blades to shape materials such as pressure-sensitive adhesives, polymer films, and metal foils. Compared to conventional photolithography, which requires complex infrastructure and controlled environments, xurography offers a low-cost and fast alternative for microfluidic device prototyping, avoiding cleanrooms and simplifying the fabrication process [11-13].

Xurography uses a cutting plotter, which performs precise incisions on laminated materials with a computer-controlled blade following a pre-set path (Fig. B.4). The device can cut through multiple layers, which are then assembled to form multilayer microdevices. This approach is particularly advantageous for microfluidics because it allows for the overlay of different materials with varying wettability and surface tension characteristics.

In my research, I used xurography to create microfluidic channels by leveraging various materials with distinct wettability properties. Assembling layers with different wettability characteristics enabled us to modulate surface tensions within the channels themselves. This selective wettability control is essential for manipulating fluid flow and transporting chemical species; for example, in microfluidic channels made with xurography, liquids can flow along predetermined paths or specific sections can be isolated depending on analytical or reaction requirements. Using this technique, I was able to precisely manage the interaction between surface and fluid, optimizing reagent manipulation and species separation.

The advantages of this technique are numerous:

- Fabrication Speed: Xurography allows the production of a complete microfluidic device in less than half an hour. The speed is due to the simplicity

of the process, eliminating complex steps like photolithographic mask preparation.

- Reduced Costs: Unlike traditional techniques, xurography requires only a cutting plotter and low-cost materials, such as easily sourced adhesives and polymers.

- Material Flexibility:The materials used, including adhesives, PVC, polymers, and metal films, are available in various forms and thicknesses, allowing for device adaptation to project-specific requirements.

-Sustainability: By reducing the number of processing steps and minimizing chemical usage, xurography has a lower environmental impact compared to photolithography and other traditional techniques.

The use of materials with different wettability properties was essential to precisely control liquid behavior within the channels. By leveraging the surface tension differences between materials, I created devices capable of guiding flows along predefined paths without pumps or other external forces, relying solely on capillary forces. This made it possible to selectively transport and distribute chemical species, a crucial advantage in applications such as biomolecule separation or biochemical reactions within a microchannel.

Despite its effectiveness, xurography has some limitations, such as lower resolution compared to photolithography. However, recent improvements in materials and cutting techniques are opening new possibilities for miniaturization. In the future, the integration of xurography with other technologies, such as 3D printing and micromilling, could further enhance the versatility of this technique, making it suitable for fabricating increasingly complex microfluidic devices.

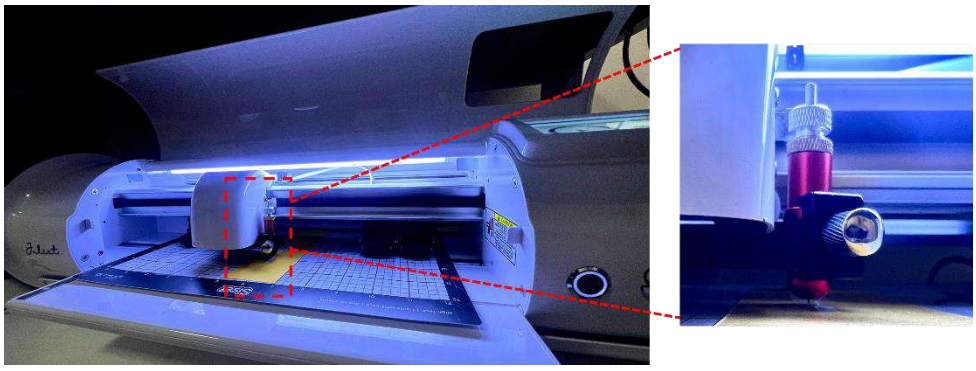

Figure B.4. Cutter plotter for xurography.

B.3 Flexible Plasmonic Device Fabrication Process

The fabrication of flexible plasmonic devices is a complex, highly specialized process that requires the careful integration of advanced microfabrication techniques to create precise structures on flexible materials. In our laboratory, the main goal is to develop flexible devices that incorporate plasmonic sensors for microfluidic applications. These devices are based on thin PDMS membranes, onto which amorphous silicon islands and gold nanoparticles are integrated through an electroless deposition process, promoting the formation of stable, optimally connected gold nanoparticle clusters on the PDMS substrate.

Step 1: Creation of PDMS Membranes

The first stage of the process involves creating thin PDMS membranes, which form the flexible base of the device. To achieve the desired consistency and thickness, PDMS pre-polymer is mixed with a cross-linking agent in a 10:1 ratio. This mixture is then deposited onto a silicon or glass wafer using a spin-coater. The spin-coating process ensures an even distribution of the material, with the final membrane thickness determined by the rotation speed and the volume of the mixture used. The spin-coating parameters are as follows (Table IV):

Volume (ml)	**Velocity (rpm)**	**Time (s)**	**Acceleration (rpm/s)**	**Thickness (µm)**
5	1000	10	300	100
5	500	10	300	300
10	500	10	300	350
10	300	10	200	500

Table IV

Depending on the application requirements, the appropriate PDMS thickness is selected to ensure the flexibility and robustness of the final device. After spin-coating, PDMS is cured in an oven to complete the cross-linking process.

Step 2: Lithographic Patterning

To create PDMS islands where gold nanoparticles will be deposited, lithographic patterning is performed using a positive resist (OIR9060). The resist is spread on the PDMS using a spin-coater at 4000 rpm for 60 seconds, achieving a thickness of about 1.3 micrometers. After application, the resist undergoes UV exposure using a lithographic mask with a pattern of 100-micrometer diameter holes. The parameters for this step are:

- Substrate: Glass
- Resist: OIR 906-12 (positive)
- Spin Coating: 4000 rpm for 60 seconds (estimated thickness: 1.3 micrometers)
- Soft Bake: 90 °C s for 60 seconds
- UV Exposure: 140 $mJ/\ cm^2$with a 16 mW/cm^2 source for 9 seconds
- Post Bake: 120 °C for 60 seconds
- Development: OPD 4262 for 60 seconds at 22 °C
- Rinse: Deionized Water

At the end of the lithographic process, a well-defined PDMS membrane pattern is obtained, with the exposed PDMS areas representing the islands on which amorphous silicon will be deposited.

Step 3: Deposition of Thin Amorphous Silicon Film Using PECVD

To improve gold nanoparticle adhesion to PDMS and to facilitate the catalytic reduction of gold ions, the PDMS surface is coated with a thin layer of

amorphous silicon (a-Si) using PECVD. PECVD is ideal for deposition on sensitive materials like PDMS, as it operates at lower temperatures compared to traditional chemical deposition methods.

The PECVD process uses gases like silane (SiH4), which, once ionized by an RF source at 13.56 MHz, forms a plasma that activates deposition reactions. The energy generated by the plasma allows the process to avoid high temperatures, thus preserving PDMS stability. The parameters used for PECVD are:

- Temperature: 100 °C
- Process Gas: Silane (SiH4) with a flow rate of 600 sccm
- Chamber Pressure: 1.2 mbar
- RF Power: 2 W
- Deposition Time: 5 minutes
- Final Film Thickness: 160 nm

The amorphous silicon layer serves as a catalytic surface for the subsequent gold nanoparticle deposition, improving adhesion and ensuring homogeneous nanoparticle growth for a high-quality final film.

Figure B.5. Plasma Enhanced Chemical Vapor Deposition (PECVD) machine

Step 4: Amorphous Silicon Removal via Lift-Off

After the amorphous silicon deposition, a lift-off process is performed to remove the film from undesired areas. The sample is immersed in acetone and placed in a sonic bath for 5 minutes, during which the acetone dissolves the photoresist and removes amorphous silicon from the covered areas. At the end of this step, only the amorphous silicon islands on the PDMS remain, which will act as the substrate for gold nanoparticle deposition.

Step 5: Electroless Gold Nanoparticle Deposition

To deposit gold nanoparticles on the amorphous silicon islands, the electroless deposition technique is used. This method allows direct deposition of gold ions on the amorphous silicon surface, promoting the growth of semi-spherical gold nanoparticles [14]. The electroless deposition solution includes hydrofluoric acid and gold chloride (AuCl3), with the following parameters:

- Deposition Solution: 0.15 M hydrofluoric acid (HF) and 5 mM gold chloride ($AuCl_3$)
- Immersion Time: 40 min
- Solution Temperature: 50 °C

During this process, the amorphous silicon acts as a catalyst for gold ion reduction, causing the ions to aggregate into well-adhered nanoparticles. This result is essential for ensuring the stability and functionality of the nanoparticles within the device.
The complete process results in a flexible plasmonic device equipped with gold nanoparticle islands integrated onto a PDMS membrane. The combination of lithographic, PECVD, and electroless deposition techniques allows precise control over the morphology and composition of the device. The PDMS membrane offers high optical transparency and biocompatibility, making the device ideal for applications requiring direct interaction with biological samples or fluids. The flexibility of PDMS also enables versatile use of the device in settings where adaptability to curved or complex surfaces is required.

B.4 Optical Characterization

Profilometer
The stylus profilometer is an essential tool in our laboratory, providing precise thickness measurements for both lithographically fabricated structures and thin films, such as amorphous silicon used in microfluidic and plasmonic devices. Often referred to as a mechanical contact profilometer, it operates by using a fine probe to physically trace the surface of a sample, capturing every variation in height with exceptional accuracy.

Its ability to collect highly detailed topographic data makes it particularly valuable in verifying that fabrication adheres to design specifications. For

example, during thin film deposition, ongoing checks on samples help maintain uniform thickness, preventing errors or imperfections that might impact the performance of the device.

The mechanism of profilometer relies on a diamond-tipped stylus mounted on a mobile arm, which gently makes contact with the sample surface. The ultra-sharp stylus follows a horizontal path across the surface, tracing even the smallest topographic variations. Surface changes, even at the nanometer scale, push the stylus up or down, generating vertical movements that are converted into electrical signals. These signals are then processed into a digital graph, creating a two-dimensional representation of the topography of sample.

This process produces a comprehensive view of height variations across the surface of sample, enabling the identification of any defects or inconsistencies in the deposition or patterning. One of the primary applications of profilometer is measuring thin film thickness, where the height difference between a coated area and an adjacent uncoated or etched region provides an extremely accurate measurement. With nanometer-level precision, the stylus profilometer is ideal for analyzing delicate films like amorphous silicon, ensuring consistency and quality in thin film fabrication.

Atomic Force Microscopy (AFM)

Measuring the thickness and topography of thin films, such as amorphous silicon, requires extremely precise instruments to detect sub-nanometric variations without damaging delicate samples. Atomic Force Microscopy (AFM) in non-contact mode is particularly suited for this purpose, as it allows for detailed three-dimensional images and quantitative measurements of thickness and roughness [15].

When using AFM in non-contact mode, the tip does not touch the sample surface but detects topographic variations through intermolecular forces, such as van der Waals and electrostatic forces, acting at close range. This method

minimizes the risk of damaging the sample and enables highly detailed surface and thickness information.
In AFM operation, the tip, mounted on a cantilever, is brought close to the surface to a distance of about 1-10 nanometers. At this range, the cantilever oscillates at a frequency near its resonance, and intermolecular forces between the tip and the sample alter the amplitude, frequency, and phase of the oscillation of the cantilever. A feedback system continuously detects these changes and adjusts the distance between the tip and the surface, maintaining constant oscillation and tracing the topography without direct contact.

The oscillation of cantilever variations are then converted into electrical signals, generating a three-dimensional surface map with sub-nanometric resolution, even reaching atomic-level details. To measure film thickness, AFM analyzes the height of both the coated area and an uncoated or etched region; the height difference between these two areas represents the film thickness. This approach is ideal for thin films or soft surfaces, as it avoids direct contact that could damage or alter the sample.

Scanning Electron Microscope (SEM)
The SEM enabled us to thoroughly examine the flexible plasmonic device due to its ability to observe the finest details of surface structure and sample composition [16]. By emitting a high-energy electron beam focused by electromagnetic lenses down to nanometric dimensions, the SEM allows for extremely high-resolution images. This precision, guaranteed by the adjustable beam energy and high-quality lenses, enables a clear exploration of every morphological and chemical characteristic of the device, revealing essential information for our analysis.

Once focused, the electron beam is guided with extreme precision across each point on the sample surface by a scanning coil system. This controlled movement creates a detailed map of the surface features, as each point reveals a specific interaction between the electrons and the material, providing a complete view of the topography and composition.

During this interaction, the beam generates several signals essential for analysis. Secondary electron (SE) signals are formed when electrons transfer energy to the surface electrons of the sample, which are sensitive to topography; these signals produce high-contrast images ideal for morphological study. In contrast, backscattered electron (BSE) signals emerge when electrons bounce back from atomic nuclei, and due to this property, they reflect atomic composition: heavier elements generate stronger signals, clearly distinguishing areas with different materials.

For advanced chemical characterization, the SEM can be integrated with an Energy Dispersive X-Ray Spectroscopy system (EDS or EDX), which utilizes X-rays emitted by excited atoms in the sample. Each element emits a unique energy signature, making it possible to create a chemical map that identifies and quantifies the elements on the surface.

The signals collected by the detectors are transformed into high-resolution images, revealing morphological and compositional details on a nanometric scale. This combination of data makes the SEM a versatile and powerful tool, ideal for analyzing micro- and nanostructured surfaces, such as microdevices, coatings, and nanoparticles. Thanks to its ability to accurately analyze complex materials, the SEM is critical for research and quality control in materials science and nanotechnology, especially in advanced manufacturing contexts.

References

1 G. M. Whitesides, The origins and the future of microfluidics, 2006, Nature 442, 368-373;

2 Henrik Bruus, Theoretical microfluidics, Oxford, 2008;

3 Xia, Y. and Whitesides, G.M. (1998) Soft Lithography. Ann. Rev. Mater. Sci. 28, 153–184;

4 N.-T. Nguyen, S. T. Wereley, Fundamentals and Applications of Microfluidics, 2006, Artech House;

5 A. del Campo and C. Greiner, SU-8: a photoresist for high-aspect-ratio and 3D submicron lithography, J. Micromech. Microeng. 17 (2007) R81–R95;

6 R. Daunton, A. J. Gallant and D. Wood, Manipulation of exposure dose parameters to improve production of high aspect ratio structures using SU-8, J. Micromech. Microeng. 22 (2012) 075016 (8pp);

7 J.C. McDonald, G.M. Whitesides, Poly(dimethylsiloxane) as a material for fabricating microfluidic devices, Acc. Chem. Res., 35 (2002), pp. 491–499;

8 J. Cooper McDonald, David C. Duffy, Janelle R. Anderson, Daniel T. Chiu, Hongkai Wu, Olivier J. A. Schueller and George M. Whitesides, Fabrication of microfluidic systems in poly(dimethylsiloxane), Electrophoresis 2000, 21, 27–40;

9 Mark A. Eddings, Michael A. Johnson and Bruce K. Gale, Determining the optimal PDMS–PDMS bonding technique for microfluidic devices, J. Micromech. Microeng. 18 (2008) 067001;

10 Chung, C. K., Tsai, M. Q., Tsai, P. H., & Lee, C. (2004). Fabrication and characterization of amorphous Si films by PECVD for MEMS. Journal of Micromechanics and Microengineering, 15(1), 136;

11 Bartholomeusz, D. A., Boutté, R. W., & Andrade, J. D. (2005). Xurography: rapid prototyping of microstructures using a cutting plotter. Journal of Microelectromechanical Systems, 14(6), 1364-1374;

12 Speller, N. C., Morbioli, G. G., Cato, M. E., Cantrell, T. P., Leydon, E. M., Schmidt, B. E., & Stockton, A. M. (2019). Cutting edge microfluidics:

Xurography and a microwave. Sensors and Actuators B: Chemical, 291, 250-256;

13 Shahriari, S., Patel, V., & Selvaganapathy, P. R. (2023). Xurography as a tool for fabrication of microfluidic devices. Journal of Micromechanics and Microengineering, 33(8), 083002;

14 E. Battista, M.-L. Coluccio, A. Alabastri, M. Barberio, F. Causa, P.-A. Netti, E. Di Fabrizio, F. Gentile, Metal enhanced fluorescence on super-hydrophobic clusters of gold nanoparticles, Microelectron. Eng. 175 (2017) 7–11;

15 Trache, A., & Meininger, G. A. (2008). Atomic force microscopy (AFM). Current Protocols in Microbiology, 8(1), 2C-2;

16 Mohammed, A., & Abdullah, A. (2018, November). Scanning electron microscopy (SEM): A review. In Proceedings of the 2018 International Conference on Hydraulics and Pneumatics—HERVEX, Băile Govora, Romania (Vol. 2018, pp. 7-9).

APPENDIX C
HOE-Based PDMS Waveguide for Advanced Biosensing

As described in Chapter 5, the next step involves integrating holographic optical elements (HOEs) into our flexible sensor to achieve total internal reflection (TIR) and create a PDMS waveguide. This approach will channel light directly toward the sensor and subsequently detect it through a photodetector, ensuring precise and compact optical signal transmission.

In this section, I describe the development mechanism of the HOEs and present an initial application, with a view toward their integration into the final device. Creating the HOE involves using an interferometric recording system which, through a prism and a suitably configured laser beam, enables the formation of specific diffraction gratings to confine light within the PDMS. This process allows precise control over the light path, essential for device miniaturization and efficiency.

The integration of HOEs into our sensor is an essential step to enhance the robustness and optical efficiency of the system, eliminating bulky optical components and simplifying the overall device structure. This work, along with experiments conducted to optimize the recording parameters and diffraction characteristics of the HOE, has been carried out in collaboration with TU Dublin, which provided technical and scientific support in refining the holographic setup.

C.1 Holographic Optical Element (HOE)

An HOE (Holographic Optical Element) is an optical component created through holographic techniques, used to deflect, modulate, or focus light in a highly controlled manner. HOEs are produced by recording laser beam interferences onto a photosensitive material to form a diffraction grating that interacts with incoming light, allowing for reflection, transmission, or diffraction at specific angles and wavelengths [1-4]. These elements are applied in various fields, including integrated optical systems and biosensing devices.

The holographic diffractive optical element (HOE) was recorded using a prism configuration within an interferometric setup. This method leverages the unique properties of light to create structures that precisely deflect the beam, which is essential for the system to function. The commercial material selected for recording offers high light sensitivity, making it ideal for forming the diffraction gratings needed to guide light within the PDMS. In Figure C.1, the recording mechanism of the HOE element is illustrated, where two light beams create an interference pattern on the photosensitive material. In the subsequent reconstruction process, once the recorded material is illuminated, it precisely redirects the light beam at the desired angle. Here, the HOE is designed to deflect the light at an angle that ensures total internal reflection (TIR) within the device, allowing for optimal guidance of light along the predetermined path.

Figure C.1 shows the setup used for the HOE recording process. For this process, a laser beam with a maximum power of 500 mW and a wavelength of 532 nm was used. The light was linearly polarized, with a coherence length exceeding 100 meters. The laser beam was split into two beams, with optical power adjusted to ensure equal intensity on the photosensitive material. This material required an exposure dose of 30 mJ/cm^2, with an exposure time of approximately 5 seconds.

During recording, the two beams created an interference pattern on the photosensitive material. In the subsequent reconstruction process, once the

recorded material is illuminated, it precisely redirects the light beam at the desired angle. Here, the HOE deflects the light at an angle that ensures total internal reflection (TIR) within the device, allowing for optimal guidance of light along the predetermined path.

After laser exposure, the photosensitive material was treated with uniform UV light for 5 minutes to complete the "bleaching" process, necessary to stabilize the holographic element. Several HOEs were recorded and characterized to identify optimal recording parameters. The diffraction efficiency of each HOE was evaluated in various areas, allowing us to select the highest-performing sections, which were subsequently cut and positioned on the PDMS waveguide as coupling elements for incoming and outgoing light.

In Figure C.1, a PDMS waveguide is shown with an HOE applied to its surface, which deflects a 532 nm light beam, enabling total internal reflection (TIR) within the material. This approach allows precise control of the light path, eliminating the need for bulky optical components, thereby optimizing device compactness and enhancing optical efficiency.

Integrating HOEs into the system offers several advantages. Firstly, it enables selective deflection of light at specific wavelengths and angles, ensuring the optical confinement needed for TIR within PDMS. Additionally, holographic recording allows HOEs to be tailored to meet the specific requirements of each application, enhancing precision and efficiency. Finally, the direct integration of HOEs onto the PDMS surface simplifies device design, reducing the need for complex optical alignments and improving overall robustness.

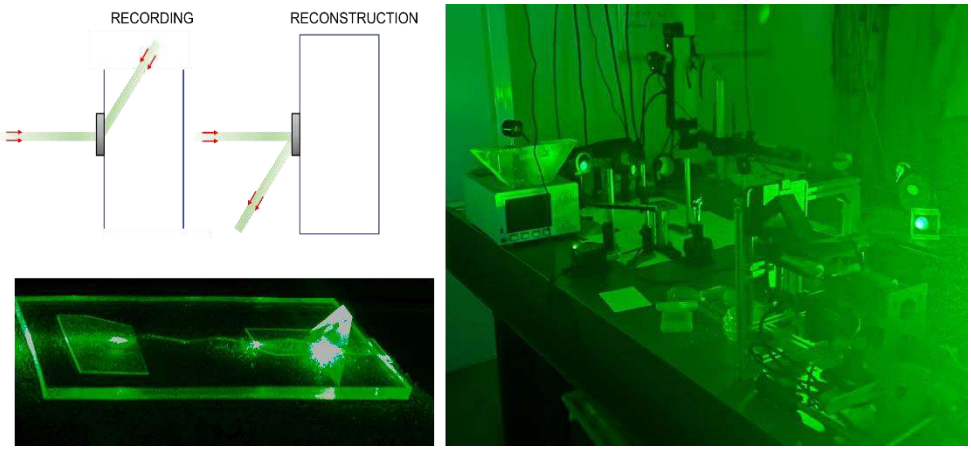

Figure C.1. a) Schematic of HOE recording and reconstruction process, illustrating the setup for interference recording and the subsequent reconstruction phase; b) Laboratory setup for HOE recording; c) PDMS waveguide with an HOE applied to its surface, deflecting a 532 nm light beam and enabling total internal reflection (TIR) within the material.

C.2 First Application

A key experiment demonstrating the effectiveness of this approach involved a PDMS microfluidic system filled with a methylene blue solution. In this setup, an HOE served as an optical coupling element for both input and output, enabling the excitation and detection of fluorescence from the dye solution. The configuration was divided into several key stages:

- Excitation Light Coupling: Light from a 633 nm wavelength laser was coupled into the system through an input HOE, positioned on the PDMS waveguide. This diffractive element directed the excitation light at the desired angle, enabling TIR within the waveguide and guiding the light toward the chamber containing the dye solution.

- Fluorescence Excitation and Detection: The methylene blue dye was excited by the 633 nm light, emitting fluorescence at 700 nm. A second HOE, designed to deflect the emitted 700 nm light, acted as the output coupling element. This HOE captured the fluorescent light and guided it to a photodiode for detection.

- Spectral Analysis: The optical signal was analyzed with a spectrometer, detecting both the incoming excitation light at 633 nm and the emitted fluorescent light at 700 nm. Spectroscopy confirmed the capability of the system to clearly distinguish between excitation and emitted light, demonstrating effective.

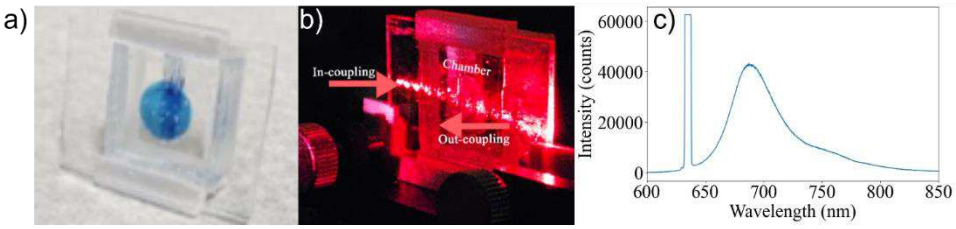

Figure C.2. a) PDMS microfluidic system with methylene blue dye solution attached to glass; b) Excitation of the dye chamber with a 633 nm in-coupler and 700 nm out-coupler; c) Spectrum of the in-coupled (excitation - 633nm) signal and the out-coupled (fluorescent dye solution – 700nm) signal from the system TU DUBLIN.

In conclusion, this experiment highlights the effectiveness of this approach in integrating optical coupling based on HOEs within a PDMS microfluidic system for precise excitation and detection of fluorescence. Using HOEs as input and output coupling elements successfully enabled total internal reflection (TIR) within the PDMS waveguide, allowing controlled guidance of the excitation light to the target chamber and efficient capture of the emitted fluorescent signal.

The ability to distinguish between the excitation light at 633 nm and the emitted fluorescence at 700 nm through spectral analysis demonstrates the robustness of the system in separating and detecting specific optical signals. This clear spectral separation confirms that the system can precisely manage both excitation and emission pathways, validating the role of HOEs in enhancing optical efficiency and compactness. These results open up opportunities for further development of advanced microfluidic biosensing devices that use integrated diffractive elements for high-sensitivity fluorescence detection in flexible, portable formats.

References

1 Close, D. H. (1975). Holographic optical elements. Optical Engineering, 14(5), 408-419.

2 Kim, N., Piao, Y. L., & Wu, H. Y. (2017). Holographic optical elements and application. Holographic Materials and Optical Systems, 5, 99-131.

3 Sweatt, W. C. (1977). Describing holographic optical elements as lenses. JOSA, 67(6), 803-808.

4 Lukin, A. V. (2007). Holographic optical elements. Journal of Optical Technology, 74(1), 65-70.

Acknowledgments

I would like to express my deepest gratitude to the Institute of Applied Sciences and Intelligent Systems (ISASI-CNR) in Naples for welcoming and supporting me throughout my PhD journey.

A special and heartfelt thank you goes to Eng. Giuseppe Coppola, not only my supervisor but also a precious mentor during this journey. His dedication, unwavering support, and ability to share knowledge with passion have been a constant source of guidance for me. With patience and generosity, he has taught me not only technical skills but also the value of scientific curiosity, rigor, and perseverance. Thanks to him, I was able to face every challenge with greater confidence, knowing that I could always rely on a mentor who was present, ready to offer valuable advice or encourage me to improve. His trust in me has been one of the most important driving forces throughout this journey.

I would also like to extend my sincere thanks to Eng. Mario Iodice, who, with his experience and availability, has been another fundamental reference point for me. His guidance has helped me grow professionally, and his encouragement has made this journey even more meaningful.

I would also like to thank Prof. Francesco Giuseppe Della Corte for his presence in my academic journey.

A sincere thank you goes to Prof. Francesco Gentile from the University of Catanzaro Magna Graecia, with whom I had the pleasure of collaborating throughout my PhD. His expertise and support have been essential contributions to our research work.

A profound thanks to Dr. Ruslan Efremov and Eng. Stefania Torino, who accompanied me during my experience in Belgium. Their support, professionalism, and enthusiasm have been a great source of inspiration for me. With them, I had the opportunity to grow, exchange ideas, and enrich my knowledge, making this adventure even more special.